Nonlinear Gain Dynamics of Quantum Dot Semiconductor Optical Amplifiers

vorgelegt von
Diplom-Physiker
Niels Majer
aus Göttingen

von der Fakultät II – Mathematik und Naturwissenschaften –

der Technischen Universität Berlin

zur Erlangung des akademischen Grades
Doktor der Naturwissenschaften
– Dr. rer. nat. –
genehmigte Dissertation

Promotionsausschuss:

Vorsitzender:	Prof. Dr. Michael Lehmann
Berichter:	Prof. Dr. Eckehard Schöll, PhD
Berichter:	Prof. Dr. Weng W. Chow

Tag der wissenschaftlichen Aussprache: 13. April 2012

Berlin 2012
D 83

Abstract

In this work the nonlinear gain dynamics of electrically injected quantum dot semiconductor optical amplifiers is investigated.

At first the semiclassical modeling ansatz on the basis of Maxwell-Bloch equations is presented. An important aspect are here the carrier scattering processes between the confined quantum dot states and the surrounding quasi-2D carrier reservoir states. Based on a detailed microscopic description of the Coulomb scattering processes density and temperature dependent scattering rates for the quantum dot-quantum well Auger scattering processes are calculated.

In the next part of this work the dynamic properties of quantum dot semiconductor optical amplifiers are investigated. The impact of the different scattering channels on the gain recovery of the device is investigated. As a main result it is shown that a cascading relaxation scattering channel drives the ultrafast gain recovery dynamics associated with quantum dot amplifiers. Furthermore, comparisons with gain recovery measurements suggest that carrier heating significantly enhances the gain recovery dynamics.

The stability properties of lasers are closely related to the linewidth enhancement factor, or α-factor. In the next part of this work the impact of the coherent interaction of the quantum dot states and the 2D reservoir states on the static α-factor is investigated. As a main result it is shown, that the α-factor of quantum dot based devices is largely determined by the coherent interaction of the reservoir.

Furthermore, it is shown that the coherent interaction of the reservoir states also has a huge impact on the phase dynamics and the chirp of ultrashort input pulses.

The last part of this work deals with nonlinear wavelength conversion using non-degenerate four-wave mixing. Based on the results on Coulomb scattering, it can be shown that the high bandwidth of nonlinear wavelength conversion in quantum dot semiconductor optical amplifiers is linked to the efficient scattering mechanisms between the reservoir and the quantum dot states.

Deutsche Zusammenfassung

In dieser Arbeit wird die nichtlineare raum-zeitliche Dynamik von quantenpunktbasierten Halbleiterverstärkern untersucht.

Im ersten Teil der Arbeit wird das zur Beschreibung und Vorhersage der Dynamik von Quantenpunktverstärkern entwickelte semiklassische Modell auf Basis von Maxwell-Bloch Gleichungen vorgestellt. Ein wichtiger Aspekt hierbei beinhaltet die Beschreibung des Ladungsträgeraustauschs zwischen den gebundenen Quantenpunktzuständen und dem umgebenden Ladungsträgerreservoir. Auf Grundlage einer detaillierten mikroskopischen Beschreibung der verschiedenen Coulomb-Streuprozesse werden dichte- und temperaturabhängige Coulomb-Streuraten für direkte Einfangprozesse vom Reservoir in den Quantenpunkt sowie für Relaxationsprozesse innerhalb der gebundenen Quantenpunktzustände berechnet.

Im zweiten Teil der Arbeit wird die Dynamik des Quantenpunktverstärkers untersucht. Hier wird zunächst der Einfluss der einzelnen Streukanäle auf die Gewinnerholungsdynamik des Bauteils analysiert. Als Hauptergebnis wird gezeigt, dass ein kaskadenartiger Relaxationsprozess maßgeblich die ultraschnelle Gewinndynamik von Quantenpunktverstärkern bestimmt. Durch Vergleiche mit experimentellen Daten zur Gewinnerholungsdynamik wird desweiteren gezeigt, dass eine Aufheizung des Bauteils die Gewinnerholungsdynamik wesentlich beschleunigt.

Die Stabilitätseigenschaften von Lasern sind eng mit dem linienverbreiternden α-Faktor verknüpft. Es wird der Einfluss der kohärenten Wechselwirkung der Quantenpunkte und des Ladungsträgerreservoirs auf den α-Faktor untersucht und als Hauptresultat wird gezeigt, dass der α-Faktor von quantenpunktbasierten Bauteilen maßgeblich durch die kohärente Wechselwirkung des Reservoirs bestimmt wird.

Weiterhin wird anhand der raum-zeitlichen Dynamik von ultrakurzen Eingangspulsen gezeigt, dass die kohärente Wechselwirkung im Reservoir auch hier einen erheblichen Einfluss auf das Phasenverhalten und insbesondere den Chirp der Signale hat.

Im letzten Teil der Arbeit zur nichtlineare Wellenlängenkonversion mittels Vierwellenmischung kann, basierend auf den Ergebnissen zur Ladungsträgerstreuung, bestätigt werden, dass die hohe Bandbreite der nichtlinearen Wellenlängenkonversion in Quantenpunktverstärkern auf die effiziente Coulomb-Streuung in Quantenpunktsystemen zurückzuführen ist.

List of publications

[MAJ10] N. Majer, K. Lüdge and E. Schöll. Cascading enables ultrafast gain recovery dynamics of quantum dot semiconductor optical amplifiers. Phys. Rev. B **82**, 235301 (2010).

[WEG10] M. Wegert, N. Majer, K. Lüdge, S. Dommers-Völkel, J. Gomis-Bresco, A. Knorr, U. Woggon and E. Schöll. Nonlinear Gain Dynamics of Quantum Dot Optical Amplifiers. Semicond. Sci. Technol. **26**, 014008 (2011).

[MAJ11] N. Majer, S. Dommers-Völkel, J. Gomis-Bresco, U. Woggon, K. Lüdge and E. Schöll. Impact of carrier-carrier scattering and carrier heating on pulse train dynamics of quantum dot semiconductor optical amplifiers. Appl. Phys. Lett. **99**, 131102 (2011).

[MAJ11a] N. Majer, K. Lüdge and E. Schöll. Maxwell-Bloch approach to Four-Wave Mixing in quantum dot semiconductor optical amplifiers. In Joachim Piprek, Hrsg., *11th Internat. Conf. on Numerical Simulation of Optoelectronic Devices (NUSOD), Rome 2011*, IEEE Proc., Seiten 153–154. IEEE, 2011.

Contents

List of Figures

List of Tables

Chapter 1

Introduction

The optical and electronic properties of semiconductor based optical devices have been a subject of intense theoretical and experimental research over the last decades. Besides the fundamental interest in the underlying physics there is a wide range of possible applications for example in optical communications.

The possibility to realize a semiconductor laser was first mentioned by John von Neumann in an unpublished manuscript sent to Edward Teller on September 19, 1953. In this manuscript entitled *Notes on the photon-disequilibrium-amplification scheme*, and later published in IEEE Journal of Quantum Electronics, he calculated the transitions between two Brillouin zones B_1 and B_2 and stated "... We will actually work with a setup, where there are few electrons in B_1 and there is an excess of holes over electrons, so that the region $E < \overline{E}$ in B_2 is very nearly filled with holes, and there are few holes with $E > \overline{E}$ in B_2. ..." Obviously, he had the idea of a *p-n* junction in mind. A summary of the von Neumann manuscript was included in Vol. 5 of the collected works of John von Neumann, which was published in 1963 [BAR63]. John Bardeen summarized von Neumann's ideas concerning a semiconductor laser in the following way: "... By various methods, for example by injection of minority carriers from a p-n junction, it is possible to upset the equilibrium concentrations of electrons in the conduction band and holes in the valence band. Recombination of excess carriers may occur primarily by radiation ... The rate of radiation may be enhanced by incident radiation of the same frequency in such a way as to make an amplifier. ..." This is exactly the concept of a laser[1]. A year later the first maser was demonstrated [GOR54] and it took until 1963 before the first realizations of injection laser diodes took place [HAL62, NAT62, HOL62].

Nowadays, semiconductor lasers are part of optical communication networks, compact disc players, optical computer mouses. The demand for higher data loads in optical networks and energy efficient data transmission to reduce the cost per transmitted bit is one aspect that has led to the development of more and more advanced devices.

The active medium, as the core of any photonic device, where the electrical energy

[1] Acronym: Light amplification by stimulated emission of radiation.

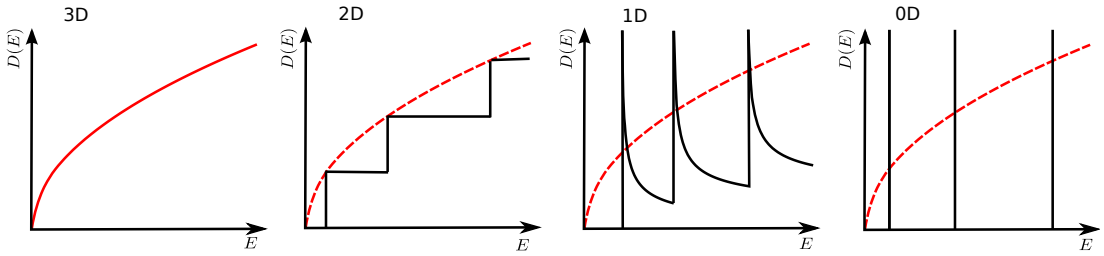

Figure 1.1: Schematic illustration of the density of states as a function of energy for bulk (3D), quantum well (2D), quantum wire (1D) and quantum dot (0D) structures.

is converted into light output, has experienced significant development due to advances in semiconductor thin film growth techniques. The evolution beginning with the early bulk devices has led to quantum well (QW) and finally to quantum dot (QD) based active materials. In bulk devices the electrons and holes can move freely in all directions within the semiconductor material. By reduction of the extent of the active region in one direction below the De-Broglie wavelength of electrons and holes, the charge carriers are confined in this direction and occupy quantized bound states. In practice, the reduction from bulk (3D) to QW (quasi-2D) is achieved by sandwiching a thin layer of semiconductor material with a lower band gap energy than the bulk between the surrounding bulk material. The step from QW (quasi-2D) to QD (quasi-0D) active regions can be achieved with a special thin film growth technique, the Stranski-Krastanow growth mode, which leads to the formation of QDs, i.e., small islands of semiconductor material which confine the electrons and holes in all three spatial directions.

As a direct consequence of the reduced dimensionality the density of states in the vicinity of the band extrema qualitatively changes as indicated in Fig. 1.1. For bulk material the density of states shows a square root dependence on energy in the vicinity of the band extrema. For the 2D case the density of state shows a stepwise behaviour and in the case of quantum dot structures the density of states is δ-distributed at the discrete energy levels of the QDs. The application of QD based devices to optical communications in the 1.3 to 1.5 μm wavelength window holds the promise of lower costs compared to the present InP based technology and also expected superior performance arising from the reduced dimensionality. Edge emitting InGaAs-based QD diode lasers have been experimentally demonstrated with low threshold currents and temperature stable operation. A low linewidth enhancement factor associated with QD lasers leads to increased stability under optical injection [PAU12, KEL11a] or modelocked operation [OTT10]. For QD based optical amplifiers broad gain bandwidths and an ultrafast response have been reported [BOR00, SUG04] making them ideal candidate in high-speed

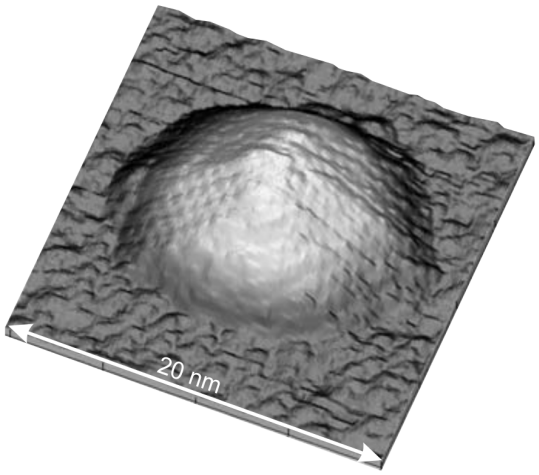

Figure 1.2: Top-view STM image of a single InAs quantum dot (from K. Jacobi et al. [XU05a]).

optical networks. Further applications of QDs include nanophotonic devices [BIM08a] and QD based single photon sources for the generation of entangled photons for secure communication purposes.

1.1 Self-assembled Quantum Dots

Quantum dots (QDs) can be regarded as mesoscopic or nanoscaled objects capable of confining electrons in all three spatial dimensions (quasi-0D). Nowadays, QDs can be fabricated in several ways, with the major distinction between epitaxial growth methods, chemical synthesis or state of the art lithography and etching techniques, and exhibit a wide range of sizes and material compositions [BIM99]. Epitaxially grown QDs are embedded in a crystalline environment and can therefore easily be integrated into semiconductor devices, and are therefore better suited for optoelectronics applications than chemically synthesized QDs. Among the epitaxially grown QDs, InGaAs/InAs QDs are probably the most widely investigated systems and this material sysem will be in the focus of the investigations throughout this thesis. Semiconductor structures with self-assembled QDs based on the Stranski-Krastanow growth mode [SEI96, JAC03] are considered. The principle workings of this thin-film growth technique is described in the following.

The Stranski-Krastanow growth is by now a well established growth mechanism for self-assembled QD structures. It has been successfully applied to III-V material systems [LAN87] like InGaAs/GaAs, InP/GaInP, InGaN/GaN, GaN/AlN and IV-IV material systems GeSi/Si. The growth techniques are typically heteroepitaxy methods

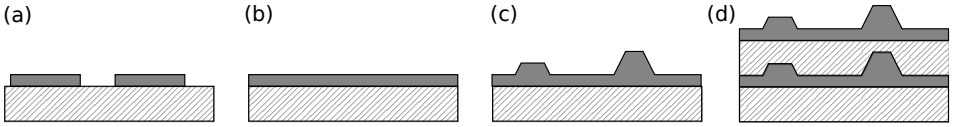

Figure 1.3: Schematic drawing of the Stranski-Krastanow thin fim growth mode. (a): Substrate and epitaxy layer less than one mono-layer. (b): Substrate and single mono-layer epitaxy material. (c): Formation of QDs for more than one mono-layer of epitaxy material. (d): Stacked QD-QW layers.

like molecular beam epitaxy (MBE) or metal-organic vapor phase epitaxy (MOVPE). Schematically, the Stranski-Krastanow growth mode is illustrated in Fig. 1.3 showing the formation of QDs. It relies on two fundamental mechanisms. First, a material which is referred to as the substrate is embedded in a surrounding barrier with a larger band gap thus leading to a confinement of electrons. The second effect is related to the morphology of the epitaxial layer. Starting with the substrate, successive mono-layers of epitaxy material are grown on top of it. The first overgrown layer is commonly referred to as the wetting layer (see Fig. 1.3(b)). In the Stranski-Krastanow growth mode the epitaxy material is lattice-mismatched to the substrate material, and the lattice constant of the epitaxy material is larger than that of the substrate. This leads to compressive strain in the epitaxy layers. By adding more material on top of the substrate a metastable state develops at a critical thickness and the epitaxy layer relaxes into a morphology with a thinner 2D wetting layer and a small 3D island on top. These islands are denoted as quantum dots (QDs) as illustrated in Fig. 1.3(c). Finally the QDs are overgrown with the material from the barrier or substrate. One refers to these types of dots as buried QDs or dot-in-a-well (DWELL) structures. In an actual photonic device such as a quantum dot laser or a quantum dot semiconductor optical amplifier one usually repeats this process yielding an active region comprised of stacked layers of QDs as indicated in Fig. 1.3(d). Each layer adds to the optical gain of the structure and therefore the total gain of the device is increased. It is important to understand that the transition from the metastable epitaxy layer into the WL-QD state is triggered by the system itself and not forced externally. Thus one refers to the process as self-organized or to the QDs being self-assembled. From intuitive grounds the formation of QDs takes place, because the build up of internal material strain in the epitaxial layer reaches a point, where it is energetically favourable to form QDs at the price of additional surface energy, because the reduction in strain energy is even larger so that the system is driven towards the QD-QW state.

In Fig. 1.2 a typical scanning tunneling microscopy image of an uncapped InAs QDs

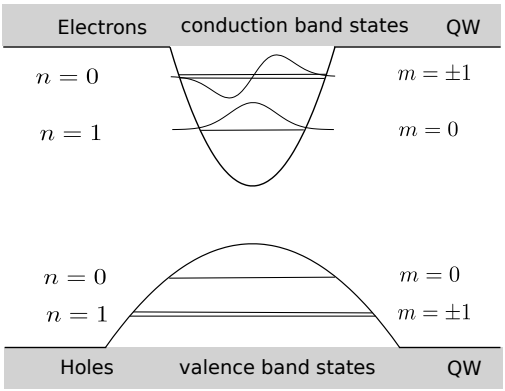

Figure 1.4: Schematic diagram of the QD energy levels of the ground state and first excited state within a harmonic oscillator potential. The QW quasi continuum has larger interband transition energies than the QD states. The labels n and m indicate the energy level index and the two-dimensional angular momentum quantum number. The degeneracy $m = \pm 1$ is indicated by two separate lines.

grown on a GaAs (001) surface is shown. The depicted QD may be characterized as being lens-shaped. Depending on the growth conditions the size and shape of the QDs can be manipulated to a certain degree. QDs formed as lenses, rings, capped or uncapped pyramids have been reported [GRU95, WOJ96, MIC03]. Throughout this work, lens-shaped QDs will be assumed, a feature that reflects itself in the form of the single-particle wave functions that enter in the calculations of Coulomb matrix elements in later chapters.

1.2 Single-particle states

The calculation of single particle states for a given confinement potential from first principles is a challenging task on its own. On the basis of tight binding and $\mathbf{k} \cdot \mathbf{p}$ models single and few particle states of QD-QW structures have been investigated in Ref.[SEG05]. The focus of the present work differs from these investigations in such a way that rather than calculating the detailed electronic structure and the single-particle wave functions, the goal of this work is to include carrier-scattering rates and single particle energy renormalizations calculated on the basis of given single-particle wave functions in a dynamic simulation of a QD based semiconductor optical amplifier (QD SOA). At this level the fundamental properties such as carrier density and temperature dependence of scattering, while the wave function model itself is used as a starting point in the calculation and not itself obtained from first principle calculations.

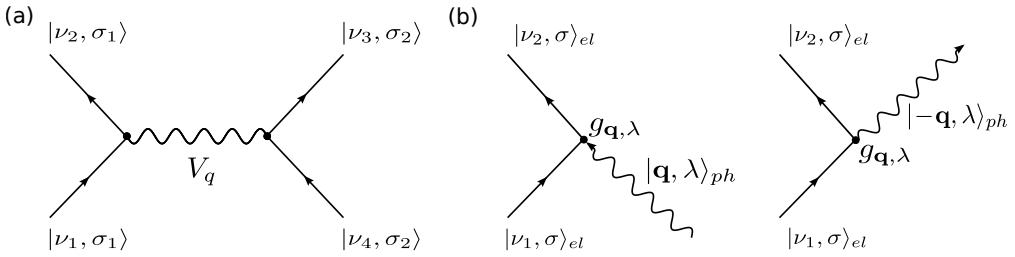

Figure 1.5: Graphical representations of carrier scattering processes. (a): Carrier-carrier scattering processes. The Coulomb matrix element V_q gives the probability amplitude for a scattering process with initial states $|\nu_1,\sigma_1\rangle$ and $|\nu_4,\sigma_2\rangle$ and final states $|\nu_2,\sigma_1\rangle$ and $|\nu_3,\sigma_2\rangle$. The initial spins σ_1 and σ_2 are preserved.(b): Carrier-phonon scattering processes involving the absorption (left) or emission of a phonon (right). The electron states are indicated by straight lines and the phonon states by curly lines and the coupling strength $g_{\mathbf{q},\lambda}$ by a dot.

For lens shaped QDs it hast been shown in Ref. [WOJ96] that the in-plane part of the single-particle wave functions are in good approximation given by two-dimensional harmonic oscillator eigenfunctions. These functions allow analytic treatment of e.g. overlap integrals and will therefore be used for the microscopic theory described later on in this work.

In Fig. 1.4 the energy diagram for lens-shaped QDs with a two-dimensional harmonic oscillator confinement potential is shown. For the given energy level spacing sketched in Fig. 1.4 each QD can confine three electrons and three holes, one in the QD ground state and two in the double degenerate first excited state. In the scope of this work only the QD ground state and first excited state will be considered. The in-plane wave function for the QD ground state has an s-orbital character with angular momentum $m = 0$, while the first excited state has a p-orbital character with angular momentum $m = \pm 1$. The QD states are located energetically below the band edge of the surrounding QW which forms a quasi-continuum indicated by the gray shaded area in Fig. 1.4.

1.3 Carrier scattering processes

The dynamical behaviour of the stimulated emission process that drives a QD laser or amplifier is to a large extent determined by the underlying charge carrier dynamics. In an electrically pumped setup the charge carriers are not injected directly into the QDs. The basic question is therefore how the charge carriers get into the QDs. To answer this question it is crucial to know the important mechanisms that drive the

QW-QD scattering processes. This problem has been theoretically addressed on various levels of sophistication ranging from quantum kinetic approaches [LOR06, LOR07] for quantum dots and quantum wires [PRE97, PRE99] to simpler perturbative approaches [INO97, WET04, WET04a]. The two basic interactions leading to a population of the QDs are carrier-carrier and carrier-phonon collisions sketched in Fig. 1.5.

At low carrier densities the charge carriers can efficiently couple to longitudinal optical (LO) phonons [INO92, INO97], while Auger type carrier-carrier collisions are relatively inefficient. Here, the use of perturbation methods leads to a so-called phonon bottleneck. The reason is, that Fermi's Golden rule for a carrier scattering process assisted by the absorption (or emission) of an LO-phonon contains an energy conserving delta-function, which allows only scattering processes where the LO-phonon energy matches the carrier transition energy. When the intraband transition energies of localized QD states does not match multiples of the LO-phonon energy, scattering is prohibited in this framework. On the contrary, recent results based on full quantum kinetic description predict an enhanced scattering efficiency for carrier-phonon processes [LOR06, LOR07].

At high carrier densities the accumulation of charge carriers can provide for efficient Auger type scattering channels between the QW and QD states. In experimental measurements of QD SOAs using heterodyne pump-probe measurements [PIW07] a power law behaviour of the gain recovery times versus injection current has been observed, which indicates that Auger capture processes dominate the carrier dynamics. In other studies of the ground and excited state recovery as a function of the injection current it was also suggested that the ultrafast relaxation processes are Auger dominated [SCH05d]. The high carrier densities that occur during operation of a QD SOA justifies to neglect the carrier-phonon processes between QD and QW states.

To ensure the predictive power of the modeling approach, Auger type scattering rates between QW states and the bound QD ground and first excited state in dependence of the QW electron and hole density are implemented into the dynamical simulation. While being complex to calculate a thorough microscopic treatment of carrier-carrier scattering processes can account for effects such as carrier heating [MAJ11]. Similar density dependent scattering rates between QW states and the QD ground state level have been successfully used to describe the turn-on behaviour of solitary QD lasers [LUE08, LUE09, LUE10, LUE10a] and to investigate the stability properties of QD lasers subjected to optical feedback [OTT10, OTT11] and to external optical injection [OTT12, PAU12, LIN12]. For quantum dot optical amplifiers the scattering formalism has been extended to include both the ground state and the first excited state of the QD. Besides direct carrier capture processes from the QW to the QD states this

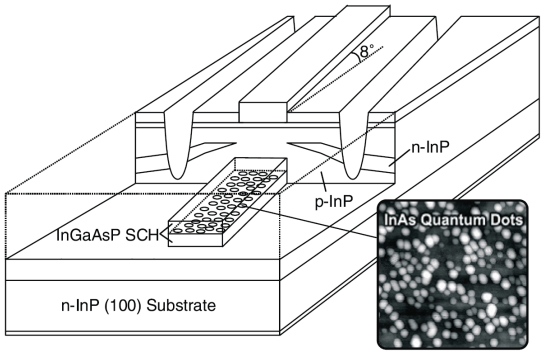

Figure 1.6: Geometric structure of a quantum dot semiconductor optical amplifier with tilted waveguide (from Sugawara et al.(2005) [SUG05].

extension also includes intradot relaxation processes from the first excited state to the ground state that have proven to be the essential processes enabling the ultrafast gain recovery observed in QD SOAs.

1.4 Quantum dot semiconductor optical amplifiers

The main focus of this thesis lies on the investigation of the dynamical properties of of quantum dot semiconductor optical amplifiers (QD SOAs). Structurally, QD SOAs are similar to quantum dot Fabry-Perot laser diodes. The major difference between QD lasers and QD SOAs is the degree of reflectivity of the end facets. For a SOA the reflectivity is engineered as small as possible, modern designs with tilted waveguides and antireflection coatings at the end facets allow refectivities as low as 10^{-5}, thus efficiently suppressing the longitudinal modes. A laser resonator on the other hand requires a high degree of reflectivity (> 0.99) to operate efficiently. The high optical losses at the end facets of the SOA prevent it from reaching a lasing state and consequently it is not possible to define a threshold current. Instead one refers to the transparency current at which a signal propagates lossless through the device. The geometric structure of a QD SOA is sketched in Fig. 1.6.

For optical networks, optical amplifiers are of largest importance serving as boosters, in-line or preamplifiers. From the laser design a reduction of the facet reflectivity has led to a development of laser amplifiers [SCH88j] to modern day optical amplifiers. The high degree of optical nonlinearities present in QD SOAs makes them attractive for all-optical signal processing such as all-optical switching, pulse shaping and pulse control, chirp compensation and nonlinear wavelength conversion. The advantages of QD SOAs over conventional QW or bulk SOAs are a broad gain bandwidth originating from the distribution in size, composition and strain of the QDs [4] , high saturation output power levels [BER04, USK05], and ultra-fast gain dynamics within the QDs [PIW07, ODR07a,

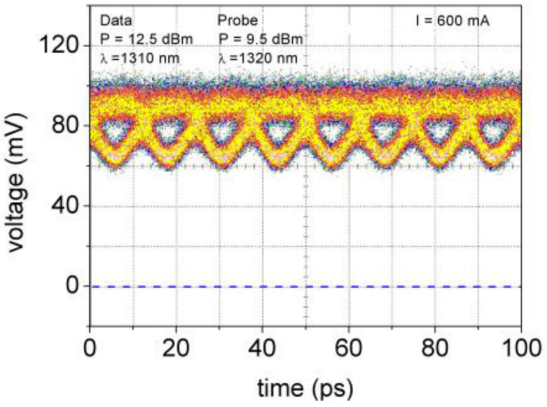

Figure 1.7: Eye diagram of a 80 Gb/s wavelength converted return to zero on-off keying signal. The input and output signals are at wavelength 1310 nm and 1320 nm (from Meuer et al.(2005) [MEU11].

GOM08], enabling amplification as well as signal processing at high data rates [SUG05, CON10]. Figure 1.7 shows an eye diagram of a 80 Gb/s wavelength converted signal from Meuer et al. [MEU11]. The open eyes indicate successful wavelength conversion with a distinct separation between the on and off state of the data stream.

From a scientific point of view SOAs can deliver valuable information on internal processes occurring in the active gain medium. Time integrated four-wave mixing experiments for example allow access to the polarization dephasing times [BOR02, BOR07b] and pump-probe spectroscopy methods give valuable information on the carrier lifetimes of the system [BOR00, GOM08].

1.5 Outline of the thesis

The thesis is structured as follows. In chapter 2 a short review of the theoretical concepts of semiclassical laser theory is given. The first part deals with the electric field dynamics on the basis of Maxwell's Equations. Approximation schemes for the spatial (device geometry) and temporal evolution of the electric field are discussed. The second part treats the material model on a quantum-mechanical level. In this section quantum dot semiconductor Bloch equations suitable for the description of QD SOAs are derived.

Chapter 3 describes the microscopic carrier-carrier scattering contributions appearing in the quantum dot semiconductor Bloch equations. A thorough analysis of the possible Auger scattering channels present in the combined QD-QW system is given and density dependent scattering rates for the different processes as input for the dynamic simulation are calculated.

In chapter 4 the spectral properties of the gain medium is investigated. The linewidth enhancement factor, or α-factor, which quantifies the amplitude phase coupling of the

electric field within the QD-QW gain medium. Furthermore, the local ultrafast nonlinear gain response of QD SOAs is analyzed. With the microscopic input at hand it is possible to quantify the relevance of different scattering contributions and it could be deduced that the relaxation channels make the dominant contributions to the ultrafast gain recovery dynamics of QD-SOAs. The contributions of QW and QD states to the α-factor and the impact of the QW in the gain and phase response of QD SOAs are discussed in detail in Chap. 5.

Wavelength conversion properties of QD SOAs using nonlinear four wave mixing (FWM) is the focus of chapter 6. As in the previous sections the focus lies on the impact of the QW and QD states on the FWM wavelength conversion efficiency.

A summary of the results of the thesis and an outlook to possible future investigations on the topic of QD SOAs is given in chapter 7.

Chapter 2

Theoretical background

In the active medium of a semiconductor laser or amplifier the light interacts with the medium and is amplified. In it the fundamental processes of absorption, stimulated and spontaneous emission occur simultaneously and interact with each other. Nonlinear laser dynamics [LUE11b] based on quantum dots is a field of active research nowadays. There exists a hierarchy of models ranging from full microscopic models to simple rate equations. The level of detail of the modeling strongly depends on the physical problem that is being addressed. Throughout this work a semiclassical ansatz is chosen to describe the dynamics of QD SOAs. In the spirit of semiclassical laser theory [HAK83a, CHO99, HAU04] only the classical character of light is accounted for while for the gain medium the quantum mechanical properties are considered.

For the QD SOA, the combined system of Maxwell's equations on the one hand and the quantum dot and quantum well semiconductor Bloch equations on the other hand, the *Maxwell-Bloch* equations, constitute the basis for the theoretical description. In the following a review of semiclassical laser theory is given and the dynamical Maxwell-Bloch equations for QD SOAs are derived.

The strong optical confinement in transverse direction in an edge emitting QD SOA and respective approximations of the field variables in terms of spatial averages of the transverse modes allows one to neglect the transverse field dynamics altogether.

The slowly varying envelope approximation (*SVEA*) to the (1D) Maxwell Equations in propagation direction enables a further reduction of the complexity leaving a single first order partial differential equation for the electric field. The validity of this temporal approximation in the context of QD SOAs is discussed.

The many-body intraband interactions in the QW are conveniently approximated in *relaxation time approximation* in terms of relaxation processes with characteristic relaxation times (Auger and carrier-phonon processes).

2.1 Electric field dynamics

Within a semiclassical modeling approach the dynamics of the electric field amplitude within the active region of the QD SOA is described by Maxwell‘s equations

$$\nabla \cdot \mathbf{D} = \rho_f, \tag{2.1}$$

$$\nabla \cdot \mathbf{B} = 0, \tag{2.2}$$

$$\nabla \times \mathbf{E} = -\frac{\partial \mathbf{B}}{\partial t}, \tag{2.3}$$

$$\nabla \times \mathbf{H} = \mathbf{J}_f + \frac{\partial \mathbf{D}}{\partial t}, \tag{2.4}$$

together with the material equations

$$\mathbf{D} = \epsilon_0 \mathbf{E} + \mathbf{P} \tag{2.5}$$

$$\mathbf{B} = \mu_0 \mathbf{H}, \tag{2.6}$$

where $\mathbf{D}$ and $\mathbf{E}$ denote the electric displacement field and the electric field, respectively, and $\mathbf{B}$ and $\mathbf{H}$ are the magnetic and magnetizing fields, respectively. The above equations are given for nonmagnetic material s (relative permeability $\mu = 1$). Furthermore, $\mathbf{J}_f$ is the free current density and ρ_f the free charge density.The macroscopi c spatial average of the microscopic dipole density of the gain medium is denoted by $\mathbf{P}$ and ϵ_0 and μ_0 are the free sp ace permittivity and permeability, respectively. Disregarding free charges ($\rho_f = 0$) and taking $\nabla\times$ of Eq. (2.3) and using Eq. (2.4) one obtains the fundamental wave equation

$$\nabla^2 \mathbf{E} - \nabla(\nabla \cdot \mathbf{E}) = \frac{1}{c^2}\frac{\partial^2 \mathbf{E}}{\partial t^2} + \mu_0 \frac{\partial^2 \mathbf{P}}{\partial t^2} + \mu_0 \frac{\partial \mathbf{J}_f}{\partial t}. \tag{2.7}$$

Solving Maxwell‘s equations is a numerically challenging task and therefore it is useful to apply spatial and temporal approximations that are well suited to the geometry of the problem and the spatio-temporal features of the involved fields, which is outlined in the following.

2.1.1 Geometric approximations

The geometry of the QD SOA is a planar ridge waveguide structure (see Fig. 1.6) and the width of the waveguide is typically in the μm regime (here $4\,\mu m$). One can therefore assume that there exists strong transversal confinement of the electric field and that it is possible to neglect the transversal field dynamics by using a *mean field* in transverse

direction. The orientation of the dipole density is directly related to the orientation of the microscopic dipoles in the QD-QW system, which depends on the growth and fabrication process of the device. In the following the electric field and dipole density are assumed to be parallel. Then, the vectorial character of the fields can be neglected.

For the propagation direction of the incident electric field the z-direction is chosen and the polarization is taken to be along the x-direction, $\mathbf{E}(\mathbf{r},t) = \tilde{E}_x(z,t)\,\mathbf{e}_x$. The spatial orientation of the macroscopic, and thus all microscopic dipoles is parallel to the electric field, i.e., $\mathbf{P} = \tilde{P}_x\,\mathbf{e}_x$. For the magnetic field then follows $\mathbf{H}(\mathbf{r},t) = \tilde{H}_y(z,t)\,\mathbf{e}_y$.

With the above assumptions Maxwell's Eqs. can be reduced to the following scalar set of equations

$$\frac{\partial \tilde{H}}{\partial t} = -\frac{1}{\mu_0}\frac{\partial \tilde{E}}{\partial z} \tag{2.8}$$

$$\frac{\partial \tilde{E}}{\partial t} = \frac{1}{\epsilon_0}\left(\frac{\partial \tilde{H}}{\partial z} - \Gamma\frac{\partial \tilde{P}}{\partial t}\right), \tag{2.9}$$

where the indices of the vector components (x,y) have been omitted. The total polarization density $\tilde{P}$ can be split into a background and a resonant contribution $\tilde{P} = \tilde{P}_{bg} + \tilde{P}_r$. Assuming a linear response of the background contribution, e.g., $\tilde{P}_{bg} = \epsilon_0\chi_{bg}\tilde{E}$ one can introduce a background dielectric constant $\epsilon_r = 1 + \chi_{bg}$ and replace ϵ_0 with $\epsilon_0\epsilon_r$ and $\tilde{P}$ with $\tilde{P}_r$ in Eqs. (2.9) and (2.9). The prefactor Γ to the polarization term in Eq. (2.9) is the transverse optical confinement factor from Eq. (B.22) accounting for the fact that the transverse mode has a finite overlap with the cross section (perpendicular to the propagation direction) of the device. The above equations describe the full wave solution of Maxwell's equation in one spatial dimension (1D). The dynamic polarization $\tilde{P}_r$ of the medium in response to the input light field at each spatial position is given by the solution of the semiconductor Bloch equations for the combined QD-QW system derived later on in Sec. 2.2. The resulting coupled Maxwell-Bloch system is the basis for the investigation of ultrafast, high power pulse excitations in the semiconductor gain medium. With this approach arbitrary signals in time and frequency domain can be investigated without restrictions to the electric field signals as the rotating wave and slowly varying envelope approximations. It includes nonlinearity, dispersion, saturation and resonance effects. The numerical approach is based on a finite difference time domain (FDTD) numerical integration scheme described in App. C.

2.1.2 Slowly varying envelope approximation

Direct integration of Maxwell's Equations with finite difference time domain methods has a major drawback due to the high computational demands that are required. In order to solve the full-field dynamics in a finite difference time domain approach both a high spatial and temporal resolution is needed in the numerical integration in order to resolve the fast oscillations of the carrier wave. However, for the case of near resonant and slowly varying spatio-temporal electric fields, the slowly varying envelope approximation (*SVEA*) and rotating wave approximation (*RWA*) can be applied. These are common approximations made in the dynamical description of semiconductor lasers. The changes to the Bloch equations in RWA and SVEA approximations will be discussed in 2.2.1.

The electric field dynamics under *RWA* and *SVEA* approximation can be reduced to the following first order wave equation (see App. B.1):

$$\left(\frac{\partial}{\partial z}+\frac{1}{\nu_g}\frac{\partial}{\partial t}\right)E(z,t)=\frac{1}{2}\Gamma i\mu_0\frac{\omega_0 c}{n_b}P(z,t), \tag{2.10}$$

where ν_g is the group velocity of the light with central frequency ω_0 in the medium and n_b is the background refractive index. Also, E and P are now the slowly varying envelopes of the full fields $\tilde{E}$ and $\tilde{P}$ defined as

$$\tilde{P}(z,t)=\frac{1}{2}P(z,t)\left(e^{i\omega t}+e^{-i\omega t}\right), \tag{2.11}$$

$$\tilde{E}(z,t)=\frac{1}{2}E(z,t)\left(e^{i\omega t}+e^{-i\omega t}\right). \tag{2.12}$$

The acquired reduced set of equations neglects group velocity dispersion (GVD) effects completely. For a QD SOA one can make the assumption that the dispersion length, e.g. the length scale on which GVD becomes important to be much larger than the nonlinear length, e.g. the length scale on which the nonlinear gain effects come to play a role. To account for dispersive effects in a slowly varying envelope framework one would need to solve a nonlinear Schrödinger equation, which includes a dispersive term proportional to the second time derivative of the electric field $\partial^2 E/\partial t^2$.

The optical transition energies present in the system cover a range beginning with the lowest optical transition energies of the QD GS around $\hbar\omega_{GS}\approx 1eV$ and ending with the highest transition energies of the QW optical transitions $\hbar\omega\geq 1.1eV$). Especially for ultrashort pulse excitations, where the frequency spectrum of the input pulses can become very large the QW transitions can be expected to interact significantly with the signal even when the central frequency of the input signal is located near the QD

transition frequencies. The full field approach is therefore a good tool to test for the validity of the reduced dynamical system in slowly varying envelope and rotating wave approximation.

Differential gain

An expression for the modal differential gain $g(z,\omega)$ (in units per length) can be obtained by Fourier transforming Eq. (2.10) and using the relation $P(z,\omega) = \epsilon_0 \chi(z,\omega) E(z,\omega)$

$$\frac{\partial}{\partial z} E(z,\omega) = i \left(\frac{\omega}{\nu_g} + \frac{1}{2} \Gamma \frac{\omega_0}{c n_b} \chi(z,\omega) \right) E(z,\omega). \tag{2.13}$$

The differential gain is given by the real part of the prefactor in front of E on the right hand side of Eq. (2.13)

$$g(z,\omega) = \frac{1}{2} \Gamma \frac{\omega_0}{c n_b} \operatorname{Im}[\chi(z,\omega)]. \tag{2.14}$$

2.2 The active medium

In this section a review of the quantum mechanical description of semiconductor gain media is given. The following derivation of the QD semiconductor Bloch equations relies on the concept of density matrix theory[1] [SCH98, WAC02]. The starting point is the system's Hamiltonian. The most simple ansatz for the quantum dot active medium includes the free carrier Hamiltonian H_0, describing the energy of the bound electron and hole states in the QDs, and the carrier-field interaction Hamiltonian H_{cf}, describing the light-matter interaction between the light field and the electron-hole pairs of the QDs. Within the framework of second quantization the free carrier Hamiltonian and the carrier-field Hamiltonian in dipole approximation are given by

$$\begin{aligned}\hat{H} = H_0 + H_{C-F} = &\sum_{\alpha} \epsilon_\alpha a_\alpha^\dagger a_\alpha + \sum_{\beta} \epsilon_\beta a_\beta^\dagger a_\beta \\ &- \sum_{\alpha,\beta} \left(\mu_{\alpha\beta} a_\alpha^\dagger d_\beta^\dagger + \mu_{\alpha\beta}^* d_\beta a_\alpha \right) \mathrm{Re}\left[E e^{-i\omega t} \right]. \end{aligned} \tag{2.15}$$

Here, α and β denote the single particle electron and hole states. The electric field in the dipole interaction Hamiltonian is given by

$$\tilde{E}(t) = \mathrm{Re}\left[E(t) e^{-i\omega t} \right] = \frac{1}{2} \left(E(t) e^{-i\omega t} + E^*(t) e^{i\omega t} \right). \tag{2.16}$$

The operators $a_\alpha^\dagger$ and a_α ($d_\beta^\dagger$ and d_β) are the electron (hole) creation and annihilation operators of the corresponding single particle state α (β). The dipole matrix element $\mu_{\alpha\beta}$ quantifies the dipole coupling strength of the optical transition between level α and β. The operators defined by $a_\alpha^\dagger a_\alpha$ and $d_\beta^\dagger d_\beta$ are particle number operators of the electron and hole states α and β, respectively and the terms $a_\alpha^\dagger d_\beta^\dagger$ and $d_\beta^* a_\alpha^*$ are the creation and annihilation operators of electron-hole pairs in the states α, β. The occupation probabilities of electron and hole states, $f_{e,\alpha}$ and $f_{h,\beta}$, and the microscopic polarization amplitude $p_{\alpha\beta}$ are defined in the following way

$$f_{e,\alpha} := \langle a_\alpha^\dagger a_\alpha \rangle, \tag{2.17}$$

$$f_{h,\beta} := \langle d_\beta^\dagger d_\beta \rangle, \tag{2.18}$$

$$\tilde{p}_{\alpha\beta} := \langle a_\alpha^\dagger d_\beta^\dagger \rangle^* = \langle d_\beta a_\alpha \rangle. \tag{2.19}$$

Assuming non-vanishing polarizations only between common single particle electron and

[1] An alternative approach would be the use of nonequilibrium Green's function theory [LOR06]

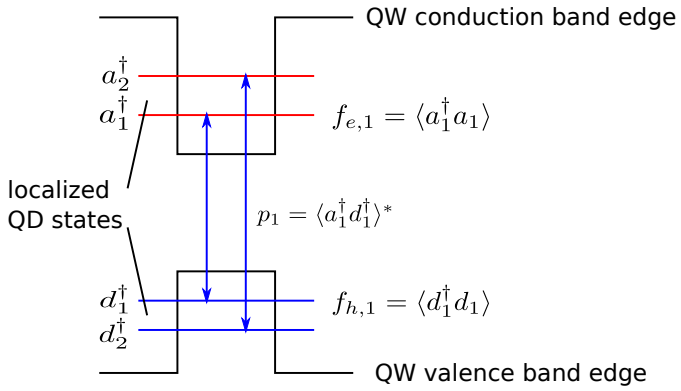

Figure 2.1: Schematic diagram of the QD energy structure with two discrete electron and hole levels.

hole states only, e.g., $\tilde{p}_{\alpha\beta} = 0$ for $\alpha \neq \beta$ the associated single particle density matrix takes the simple form

$$\rho_\alpha = \begin{pmatrix} f_{e,\alpha} & \tilde{p}_\alpha \\ \tilde{p}_\alpha^* & f_{h,\alpha} \end{pmatrix}, \tag{2.20}$$

where the second index in the polarization term has been dropped for notational simplicity, e.g., $\tilde{p}_{\alpha\alpha} := \tilde{p}_\alpha$. In the following, such a density matrix will be called diagonal in the index α. The time evolution of the density matrix elements is governed by Heisenbergs equations of motion for expectation values of operators $\hat{o}$ [MEY91, HAU04, CHO99]

$$\frac{\partial}{\partial t}\langle \hat{o} \rangle = \frac{i}{\hbar}\left[\hat{H}(t), \hat{o}(t)\right]. \tag{2.21}$$

The equations of motion for the density matrix elements from Eq. (2.20) and the Hamiltonian from Eq. (2.15) are the well-known semiconductor Bloch equations

$$\frac{\partial \tilde{p}_\alpha}{\partial t} = -i\omega_\alpha \tilde{p}_\alpha - i\frac{\mu_\alpha}{\hbar}\,\mathrm{Re}\left[E e^{-i\omega t}\right](f_{e,\alpha} + f_{h,\alpha} - 1) \tag{2.22}$$

$$\frac{\partial f_{e/h,\alpha}}{\partial t} = -\frac{i}{\hbar}(\mu_\alpha^* \tilde{p}_\alpha - \mu_\alpha \tilde{p}_\alpha^*)\,\mathrm{Re}\left[E e^{-i\omega t}\right]. \tag{2.23}$$

Note that for any diagonal density matrix Eqs. (2.22) and (2.23) are exact. When treating Coulomb interactions in chapter 3, the appearance of particle-particle correlations will introduce non-diagonal elements to the density matrix and the evaluation of the equations of motion does not immediately lead to a closed set of equations.

2.2.1 Rotating wave approximation

A common approximation of Eq. (2.22) and (2.23) is the rotating wave approximation (RWA). It relies on near resonant excitation, meaning that the frequency of the electric field interacting with the two-level medium is close to the optical transition frequency of the dipole transition. In such a situation it is favorable to transform into a frame of reference of the electric and dipole fields rotating with the central field frequency ω. Writing the polarization in the same fashion as Eq. (2.16)

$$\tilde{p}_\alpha(t) = \frac{1}{2}\left(p_\alpha(t)e^{-i\omega t} + p_\alpha^*(t)e^{i\omega t}\right) \tag{2.24}$$

and inserting Eqs. (2.16) and (2.22) into Eqs. (2.22) and (2.23) one obtains

$$\frac{\partial p_\alpha}{\partial t}e^{-i\omega t} = -i(\omega_\alpha - \omega)p_\alpha e^{-i\omega t} - i\frac{\mu_\alpha}{2\hbar}\left[E + E^* e^{2i\omega t}\right](f_{e,\alpha} + f_{h,\alpha} - 1) \tag{2.25}$$

$$\frac{\partial f_{e/h,\alpha}}{\partial t} = -\frac{i}{\hbar}(\mu_\alpha^* p_\alpha e^{-i\omega t} - \mu_\alpha p_\alpha^* e^{i\omega t})\,\mathrm{Re}\left[Ee^{-i\omega t}\right]. \tag{2.26}$$

Assuming that the slowly varying envelope of the electric field and the polarization vary little on timescales of $\frac{1}{2\omega}$ the contributions from the terms oscillating with 2ω will average to zero and can thus be neglected. Equations. (2.22) and (2.23) then simplify to

$$\frac{\partial p_\alpha}{\partial t} = -i(\omega_\alpha - \omega)p_\alpha - i\frac{\Omega_\alpha}{2}(f_{e,\alpha} + f_{h,\alpha} - 1) \tag{2.27}$$

$$\frac{\partial f_{e/h,\alpha}}{\partial t} = -\,\mathrm{Im}[\Omega_\alpha p_\alpha^*]. \tag{2.28}$$

Here, the *Rabi frequency* $\Omega = \frac{\mu_\alpha}{\hbar}E$ has been introduced. The dipole moment μ_α appearing in the Rabi frequency quantifies the strength of the dipole interaction.

2.2.2 Many-body Coulomb effects

In order to extend the derivation to also account for Coulomb interaction between charge carriers in the system the Coulomb interaction Hamiltionian in second quantization is included

$$H_C = \frac{1}{2}\sum_{\substack{a,b,c,d\\ s,s'}} V_{abcd}\left[a_{c,s}^\dagger a_{d,s'}^\dagger a_{a,s'}a_{b,s} + d_{c,s}^\dagger d_{d,s'}^\dagger d_{a,s'}d_{b,s} - 2a_{c,s}^\dagger d_{d,s'}^\dagger a_{a,s'}d_{b,s}\right], \tag{2.29}$$

where a, b, c, d denote electron and hole states of the QD-QW system and $s, s' \in \{\uparrow, \downarrow\}$ their respective spin. The Coulomb matrix element V_{abcd} is given by

$$V_{abcd} = \int d^3r d^3r' \Psi_d^*(\mathbf{r}) \Psi_c^*(\mathbf{r}') \frac{e_0^2}{4\pi\epsilon_0 |\mathbf{r} - \mathbf{r}'|} \Psi_a(\mathbf{r}) \Psi_b(\mathbf{r}'). \tag{2.30}$$

Here, Ψ denote the single particle wave functions and $V = \frac{e_0^2}{4\pi\epsilon_0|\mathbf{r}-\mathbf{r}'|}$ is the bare Coulomb potential. The additional contributions to the dynamics are readily obtained by applying Heisenbergs equations of motion:

$$\left.\frac{\partial p_\alpha}{\partial t}\right|_C = \frac{i}{\hbar} \langle [H_C, d_\alpha a_\alpha] \rangle , \tag{2.31}$$

$$\left.\frac{\partial f_{e,\alpha}}{\partial t}\right|_C = \frac{i}{\hbar} \left\langle \left[H_C, a_\alpha^\dagger a_\alpha\right] \right\rangle , \tag{2.32}$$

$$\left.\frac{\partial f_{h,\alpha}}{\partial t}\right|_C = \frac{i}{\hbar} \left\langle \left[H_C, d_\alpha^\dagger d_\alpha\right] \right\rangle . \tag{2.33}$$

As stated earlier, the Coulomb Hamiltonian introduces correlations to the system (manifesting themselves in a non-diagonal density matrix). The evaluation of the equations of motion given in Eqs. (2.31)-(2.33) couples operators consisting of two single-particle operators to expectation values of operators consisting of four single-particle operators. The time evolution of the four-operator term can be evaluated via Heisenbergs equations of motion again. The four-operator terms then couple to six-operator terms which couple to even higher orders. Eventually one obtains a hierarchy of coupled differential equations. A truncation of this hierarchy-problem can be achieved via the Hartree-Fock factorization.

Hartree-Fock approximation

The Hartree-Fock approximation [CHO99, HAU04] is based on the following factorization of four operator terms into products of two operator terms in the following way

$$\langle \hat{a}\hat{b}\hat{c}\hat{d} \rangle = \langle \hat{a}\hat{b} \rangle \langle \hat{c}\hat{d} \rangle - \langle \hat{a}\hat{c} \rangle \langle \hat{b}\hat{d} \rangle + \langle \hat{a}\hat{d} \rangle \langle \hat{b}\hat{c} \rangle. \tag{2.34}$$

Within this approximation the time evolution of the system with Coulomb effects can be reduced to a form similar to Eqs. (2.27) and (2.28)

$$\frac{\partial p_\alpha}{\partial t} = -i(\tilde{\omega}_\alpha - \omega)p_\alpha - i\frac{\tilde{\Omega}_\alpha}{2}(f_{e,\alpha} + f_{h,\alpha} - 1) \tag{2.35}$$

$$\frac{\partial f_{e/h,\alpha}}{\partial t} = -\operatorname{Im}[\tilde{\Omega}_\alpha p_\alpha^*], \tag{2.36}$$

where the renormalized transition energy

$$\hbar\tilde{\omega}_\alpha = \hbar\omega_\alpha + \sum_{\nu,b,b',s'} V^{b,b'}_{\alpha\nu\nu\alpha} - \delta_{b,b'}\delta_{s,s'}V^{b,b'}_{\nu\alpha\nu\alpha}, \tag{2.37}$$

with $b \in \{e, h\}$ and the Coulomb enhanced Rabi frequency

$$\tilde{\Omega}_\alpha = \Omega_\alpha + \frac{1}{\hbar}\sum_{\nu,\mu} V^{e,h}_{\nu\mu\alpha\alpha}\, p_{\nu\mu}, \tag{2.38}$$

have been introduced. The summation over ν and μ includes all QD as well as QW states of the combined QD-QW system. In terms of renormalized single-particle electron and hole states Eq. (2.37) can be expressed as

$$\hbar\tilde{\omega}_\alpha = \hbar\omega_\alpha + \Delta\varepsilon_{\alpha,e} + \Delta\varepsilon_{\alpha,h}, \tag{2.39}$$

with

$$\Delta\varepsilon_{\alpha,e} = \sum_{\nu,b',s'} V^{e,b'}_{\alpha\nu\nu\alpha} - \delta_{e,b'}\delta_{s,s'}V^{e,b'}_{\nu\alpha\nu\alpha}; \quad \Delta\varepsilon_{\alpha,h} = \sum_{\nu,b',s'} V^{h,b'}_{\alpha\nu\nu\alpha} - \delta_{h,b'}\delta_{s,s'}V^{h,b'}_{\nu\alpha\nu\alpha} \tag{2.40}$$

Often the Hartree-Fock approximation overestimates the Coulomb effects, so additional corrections such as the screened exchange and Coulomb hole contributions are used. Chapter 3 provides a detailed description of these first order Coulomb contributions.

2.2.3 Scattering contributions

Within the Hartree-Fock factorization scheme described above intraband and intrasubband scattering are not accounted for. Here, two mechanisms play an important role, namely, carrier-carrier and carrier-phonon collisions. Not only do these scattering processes lead to dephasing of the optical polarization and to equilibration of charge carriers in the considered QD-QW system, also scattering between QW and QD states leads to population of the QD states. Taking into account scattering one obtains additional

scattering contributions $(\partial/\partial t)f^j_{e/h,\alpha}|_{col}$ and $(\partial/\partial t)p^j_\alpha|_{col}$ to the carrier and polarization equations, respectively. A detailed analysis of these additional scattering contributions will be the topic of chapter 3 as later on these contributions will be of crucial importance for the dynamics of QD SOAs. One then obtains the Bloch equations in the general form

$$\frac{\partial p_\alpha}{\partial t} = -i(\tilde{\omega}_\alpha - \omega)p_\alpha - i\frac{\tilde{\Omega}_\alpha}{2}(f_{e,\alpha} + f_{h,\alpha} - 1) + \frac{\partial p_\alpha}{\partial t}|_{col}, \tag{2.41}$$

$$\frac{\partial f_{e/h,\alpha}}{\partial t} = -\,\mathrm{Im}[\tilde{\Omega}_\alpha p^*_\alpha] + \frac{\partial f^j_{e/h,\alpha}}{\partial t}|_{col}. \tag{2.42}$$

As stated in the introduction, the calculation of the dephasing processes accounting for the scattering contribution to the polarization dynamics, $(\partial p_\alpha/\partial t)|_{col}$, is a cumbersome task that requires a quantum kinetic approach to make accurate predictions [SCH04e, LOR06] and is beyond the scope of this work. Therefore, throughout this work, a dephasing time T_2 is introduced, which sets the time-scale on which the polarization decays and the collision term in the polarization equation, Eq. (2.41) is expressed as

$$\frac{\partial p_\alpha}{\partial t}|_{col} = -\frac{1}{T_2}p_\alpha. \tag{2.43}$$

The theoretically predicted [LOR06b] and experimentally determined [BOR00a] QD ground state dephasing times in QD systems lie in the range of $30 - 100\,\mathrm{fs}$, depending on the excitation (current injection) strength.

2.2.4 Adiabatic elimination of the polarization

The separate degrees of freedom for the polarization dynamics given by Eq. (2.48) can be neglected in the case of *"fast"* polarization decay, e.g. when the time scale of the polarization dynamics is much smaller than the time scale on which the electric field envelope evolves. Under these conditions all trajectories will approach the hypersurface given by setting $\dot{p}_\alpha = 0$ in Eq. (2.48). In the case of pulse shaped electric input fields this holds true if the temporal pulse width Δ_{FWHM} is much larger than the dephasing time T_2 of the polarizazion, e.g. $\Delta_{FWHM} \gg T_2$. Setting $\dot{p}_\alpha = 0$ in Eq. (2.41) and using Eq. (2.43) one obtains

$$0 = -i(\tilde{\omega}_\alpha - \omega)p^0_\alpha - i\frac{\tilde{\Omega}_\alpha}{2}(f_{e,\alpha} + f_{h,\alpha} - 1) - \frac{1}{T_2}p^0_\alpha. \tag{2.44}$$

The quasi-stationary value p_α^0 is then given by

$$p_\alpha^0 = \frac{\tilde{\Omega}_\alpha(f_{e,\alpha} + f_{h,\alpha} - 1)}{(\omega - \tilde{\omega}_\alpha) + i\frac{1}{T_2}}. \tag{2.45}$$

Summing over all states α one obtains the macroscopic quasi-stationary polarization density

$$P^0 = \frac{1}{V_{act}} \sum_\alpha \mu_\alpha p_\alpha^0, \tag{2.46}$$

where V_{act} is the active volume. To reduce the complexity further one can neglect the polarization dynamics completely and instead introduce a modal gain function and a linewidth enhancement factor to account for the phase dynamics. This is a common approach in laser modeling. The final step in a model reduction would consist of also neglecting the phase of the electric field and to consider only the field intensity (photon density).

2.3 Quantum dot semiconductor Bloch equations

Up to now the description has been kept general, leaving the single particle states unspecified. In a QD system, α and β are compound quantum numbers including the quantum numbers of the electronic states of the QD levels, the spin index s, as well as a spatial index $\rho_i, i = 1, \dots N$ indicating the in-plane position of each QD of a total of N QDs. As stated in the introduction and as will be explained in more detail in chapter 3, for lens-shaped QDs it is valid to make a separation ansatz for the QD wave functions into an in-plane and a z-component. With the assumption of strong z-confinement the potential in z-direction is approximated by an infinite height barrier potential and only the energetically lowest state is taken into account. The in-plane potential is approximated by a 2D harmonic oscillator potential and the in-plane wave functions are thus harmonic oscillator eigenfunctions with energy level quantum number n and magnetic quantum number m, respectively. This allows to write the QD single-particle states as

$$\alpha = \{n, m, \rho_i\}. \tag{2.47}$$

In the process of self-assembled QD growth, fluctuations in the QD geometry, especially the size, and the material composition has a direct influence on the band structure of the QD-QW system. As a result the optical transitions of th QD ensemble appear to be broadened. This effect, referred to as inhomogeneous broadening, is accounted for by

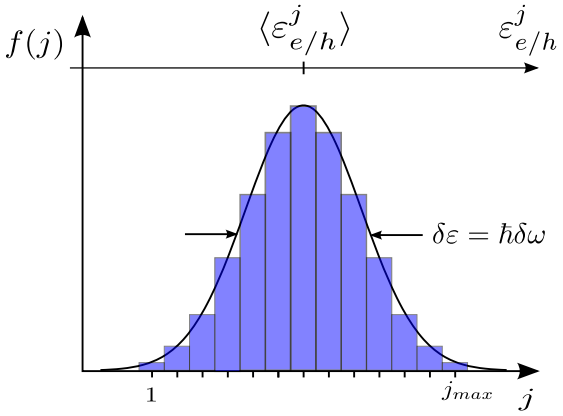

Figure 2.2: Schematic illustration of the inhomogeneous broadening of the QD transition. Each QD is assigned to a subgroup with index j with probability $f(j)$ with the central QD ground or excited state transition indicated by $\langle \varepsilon^j \rangle$. The full width at half maximum of $f(\varepsilon)$ is indicated by $\delta\varepsilon = \hbar\delta\omega$.

probability mass function $f(\varepsilon)$ for the transition energies $\varepsilon = \hbar\omega$ of the QDs. The QD ensemble is then divided into subgroups $N^j = f(\varepsilon = \varepsilon_j)N^{QD}$ such that $\sum_j f(\omega_j) = 1$. The probability mass function is taken as a Gaussian with full width at half maximum (FWHM) $\delta\varepsilon = \hbar\delta\omega$ around a central transition energy $\langle \varepsilon^j_{e/h} \rangle$. In Fig. 2.2 the probability mass function and the discrete subensembles are schematically illustrated. For now, the spin index s and the spatial index ρ_i are dropped, and instead index j discriminating QDs with different transition frequencies is introduced. Furthermore, restricting oneselves to the two lowest QD energy levels, the ground state and the first excited state, the energy level quantum number n can be suppressed as well. The dynamical equations for the QD material system can then be formulated in terms of the angular momentum quantum number m and the subgroup index j. The dynamics of each QD level (index m) within each QD subgroup of the inhomogeneously broadened QD ensemble (index j) with distinct transition frequency ω^j_m is governed by the following quantum dot semiconductor Bloch equations

$$\frac{\partial p^j_m}{\partial t} = -i(\tilde{\omega}^j_m - \omega) - i\frac{\tilde{\Omega}^j_m}{2}\left(f^j_{e,m} + f^j_{h,m} - 1\right) - \left.\frac{\partial p^j_m}{\partial t}\right|_{col}, \tag{2.48}$$

$$\frac{\partial f^j_{e,m}}{\partial t} = -\,\mathrm{Im}\left[\tilde{\Omega}^j_m\, p^{j\,*}_m\right] - R^j_{sp,m} + \left.\frac{\partial f^j_{e,m}}{\partial t}\right|_{col}, \tag{2.49}$$

$$\frac{\partial f^j_{h,m}}{\partial t} = -\,\mathrm{Im}\left[\tilde{\Omega}^j_m\, p^{j\,*}_m\right] - R^j_{sp,m} + \left.\frac{\partial f^j_{h,m}}{\partial t}\right|_{col}. \tag{2.50}$$

For a homogeneous ensemble of QDs with the same size and two localized states these are six dynamical equations. However, if a separation into x subgroups is necessary $6x$ equations need to be solved. The total 2D QD carrier density $n_{b,m}$ is obtained by summing over all subgroups,

$$n_{b,m} = 2\nu_m \sum_j f_{b,m}^j N^j; \quad b = \{e, h\}, \tag{2.51}$$

where N^j is the 2D QD density of a specific QD subgroup and ν_m is the degeneracy of the respective quantum dot state m (1 for GS and 2 for ES). The additional factor of 2 arises due to spin degeneracy of the QD levels. Furthermore, the total 3D macroscopic polarization density P^{QD} of the QDs is a linear superposition of the microscopic dipole densities of all QD states and subensembles given by

$$P^{QD} = \sum_{j,m} \frac{N^j}{h^{QW}} \mu_m^j \, p_m^j = N^{QD} \sum_{j,m} \frac{g(\omega_j)}{h^{QW}} \mu_m^j \, p_m^j \tag{2.52}$$

where h^{QW} is the height of one QW layer and N^j is the 2D density of the j-th subgroup with transition frequency ω_j of the inhomogeneously broadened QD ensemble.

2.3.1 Spontaneous emission

Spontaneous emission contributes to the loss of charge carriers in the QD states. The rate of spontaneous emission for electrons and holes is given by [SCH84a]

$$R_{sp,m}^j \left(f_{e,m}^j, f_{h,m}^j \right) = W_m^j f_{e,m}^j f_{h,m}^j, \tag{2.53}$$

with the Einstein coefficient [CHO94, LUE08]

$$W_m^j = \frac{(\mu_m^j)^2 \sqrt{\epsilon_{bg}}}{3\pi\epsilon_0\hbar} \frac{(\omega_m^j)^3}{c^3} \tag{2.54}$$

accounting for the interaction with all resonator modes. Here, μ_m^j is the dipole moment of the QD transition, ϵ_{bg} the background dielectric constant, e_0 the elementary charge , and c the vacuum velocity of light.

2.3.2 Quantum well Bloch equations

The dipole interaction of the QW optical interband transitions can be modeled using a similar ansatz as for the QDs via Bloch equations for the occupation probabilities of the

QW states and the interband polarizations.

For the case when the QW is far off-resonant and the electric field is of moderate intensity the dipole interaction of the QW states can be lumped into the background adding to the background refractive index of the material. For high field intensities though, the contributions of the QW to the gain and phase dynamics can not be neglected even for the case when the QW states are significantly detuned from the QD transitions. In situations where the phase information is relevant, e.g. when evaluating the linewidth enhancement factor, a parameter describing the amplitude phase coupling in semiconductor lasers and amplifiers [HEN82], the QW has a significant impact. Therefore, the coherent QW interaction is taken into account. In order to describe the state dependence of the QW one needs information about the band structure of the 2D quasi-continuum. For simplicity, the description is restricted to the lowest conduction and valence bands (two band approximation) and the conduction and valence bands are modeled as parabolic bands with effective masses m_e and m_h and the renormalized transition energy is given in analogy to Eq. (2.37) by

$$\hbar\tilde{\omega}_k = \hbar\omega_0 + \frac{\hbar^2 k^2}{2}\left({m_e}^{-1} + {m_h}^{-1}\right) + \Delta\varepsilon_{k,e} + \Delta\varepsilon_{k,h}. \tag{2.55}$$

Here, $\hbar\omega_0$ is the band gap energy of the QW, where m_b, $b = \{e, h\}$ are the effective masses of electrons (e) and holes (h) and $\varepsilon_{k,b}$ are the energy renormalizations of the QW states due to Coulomb effects, which are treated in detail in Sec. 3.3. The states are labeled by the 2D in-plane momentum k. The corresponding QW Bloch equations for the occupation probabilities of the QW charge carrier states f_b^k and the corresponding interband polarizations p_k then read

$$\frac{\partial p_k}{\partial t} = -i(\tilde{\omega}_k - \omega)p_k - i\frac{\tilde{\Omega}_k}{2}\left(f_e^k + f_h^k - 1\right) - \left.\frac{\partial p_k}{\partial t}\right|_{col}, \tag{2.56}$$

$$\frac{\partial f_e^k}{\partial t} = \Delta_k^b - \mathrm{Im}\left[\tilde{\Omega}_k {p_k}^*\right] - \left.\frac{\partial f_e^k}{\partial t}\right|_{col}, \tag{2.57}$$

$$\frac{\partial f_h^k}{\partial t} = \Delta_k^b - \mathrm{Im}\left[\tilde{\Omega}_k {p_k}^*\right] - \left.\frac{\partial f_h^k}{\partial t}\right|_{col}. \tag{2.58}$$

The terms $\tilde{\hbar}\omega_k$ and $\tilde{\Omega}_k$ are in analogy to Eqs. (2.48)-(2.50) the renormalized transition energies and Rabi frequencies, respectively. The term Δ_k^b contains all contributions to the population change of the QW states, which do not contain an explicit dependence on the QW states f_b^k, but rather depend on the total charge carrier densities in the QW.

Instead of evaluating the intraband carrier scattering contributions to the QW dy-

namics on a microscopic basis, a simpler relaxation time approximation for the intraband QW scattering contributions is used, where the relaxation towards quasi-equilibrium is given in terms of a relaxation rate $\gamma = \frac{1}{T_2^{QW}}$ [CHO05, WAL06]. The carrier collision contributions then read

$$\left.\frac{\partial f_b^k}{\partial t}\right|_{col} = \gamma_b \left(f_b^k - f_b^{k,eq}\right), \tag{2.59}$$

where $f_b^{k,eq}$ denotes the quasi-equilibrium occupation probability for the QW charge carriers and $\gamma_b = 1/T_1^{QW}$ is the relaxation rate. The quasi-equilibrium occupation probabilities of the QW states are given in terms of the 2D quasi-Fermi level as

$$f_b^{eq} = \left(1 + e^{\frac{\varepsilon_{k,b} - F_b^{QW}}{k_B T}}\right)^{-1} \quad , b \in \{e, h\}. \tag{2.60}$$

Here, $\varepsilon_{k,b} = \hbar^2 k^2/(2\, m_b)$ is the unrenormalized energy of the k-th QW state and F_b^{QW} is the corresponding quasi-Fermi level in the conduction and valence bands. For the 2D case the quasi-Fermi level can be expressed as a function of the total QW charge carrier density

$$w_b = \frac{1}{A} \sum_k 2 f_b^k \tag{2.61}$$

and temperature T as

$$F_b^{QW}(w_b, T) = k_B T \log\left(\exp\left[(\pi \hbar^2 w_b)/(k_B T m_b)\right) - 1\right]\right). \tag{2.62}$$

The QW state dependence of current injection, spontaneous emission and carrier-carrier scattering contributions is neglected and only the total change of the total QW charge carrier density w_b due to these processes is taken into account. The contributions to the QW occupation dynamics arising from these processes is included in the term Δ_k^b. The state dependence is kept only for the coherent QW interaction with the light field. These coherent interactions can drive the QW distributions away from quasi-equilibrium. Since the scattering rates are calculated for quasi-equilibrium distributions between QW and QD states the this approach is consistent if the deviations from quasi-equilibrium distributions in the QW are small. For the case of fast carrier equilibration processes in the QW, e.g., efficient carrier-carrier and carrier-phonon scattering processes and sufficiently weak coherent light-matter interaction with the QW states this assumption can be made. The calculation of state-dependent scattering rates would be significantly more involved and numerically challenging as would be the accurate modeling of charge transport between 3D bulk and 2D QW states (the current injection). Due to the discrete nature

of the scattering processes the population changes due to global charge carrier density changes Δ_k^b are best expressed in a discrete time formulation of Eqs. (2.57)- (2.58). Replacing the time derivative with a difference quotient with time step Δt one obtains

$$\Delta f_e^k = \Delta_t \left[\Delta_k^e - \mathrm{Im}\left[\tilde{\Omega}_k {p_k}^*\right] - \left.\frac{\partial f_e^k}{\partial t}\right|_{col} \right], \tag{2.63}$$

$$\Delta f_h^k = \Delta_t \left[\Delta_k^h - \mathrm{Im}\left[\tilde{\Omega}_k {p_k}^*\right] - \left.\frac{\partial f_h^k}{\partial t}\right|_{col} \right]. \tag{2.64}$$

The product $\Delta_t \Delta_k^b$ can now be expressed in the following way

$$\Delta_t \Delta_k^b = f_b^{k,eq}\left(\mu_b(w_b + \Delta t W_b^{inc}, T)\right) - f_b^{k,eq}\left(\mu_b(w_b, T)\right), \tag{2.65}$$

where the term W_b^{inc} contains all incoherent contributions which change the 2D QW particle density, e.g., the current injection density $j(t)$, the spontaneous emission rate in the QW $\tilde{R}_{sp}$, and the QD-QW scattering contributions $(\partial f_{b,m}^j/\partial t)|_{col}$

$$W_b^{inc} = \frac{j(t)}{e_0} - \tilde{R}_{sp} - 2\sum_{m,j} N^j \left.\frac{\partial f_{b,m}^j}{\partial t}\right|_{col}. \tag{2.66}$$

The spontaneous emission loss rate $\tilde{R}_{sp}$ is given by a bimolecular recombination rate

$$\tilde{R}_{sp} = B_s w_e w_h \tag{2.67}$$

with spontaneous emission loss coefficient B_s [SCH87]. The QW polarization decay is described in terms of a polarization lifetime as

$$\left.\frac{\partial p_k}{\partial t}\right|_{col} = -\frac{1}{T_2^{QW}} p_k = -\gamma p_k. \tag{2.68}$$

In Fig 2.3 the coherent and state independent processes in the QW are illustrated schematically. In Fig. 2.3(a) the coherent interaction is illustrated. It leads to spectral hole burning in the QW and thus creates non-equilibrium charge carrier distributions in the QW. The non-equilibrium distributions then relax towards quasi-equilibrium via carrier-carrier and carrier-phonon scattering processes (relaxation rate γ). The state independent processes are sketched in Fig. 2.3(b). They denote processes that leave the quantum well distributions in quasi-equilibrium and only change the particle number in the QW.

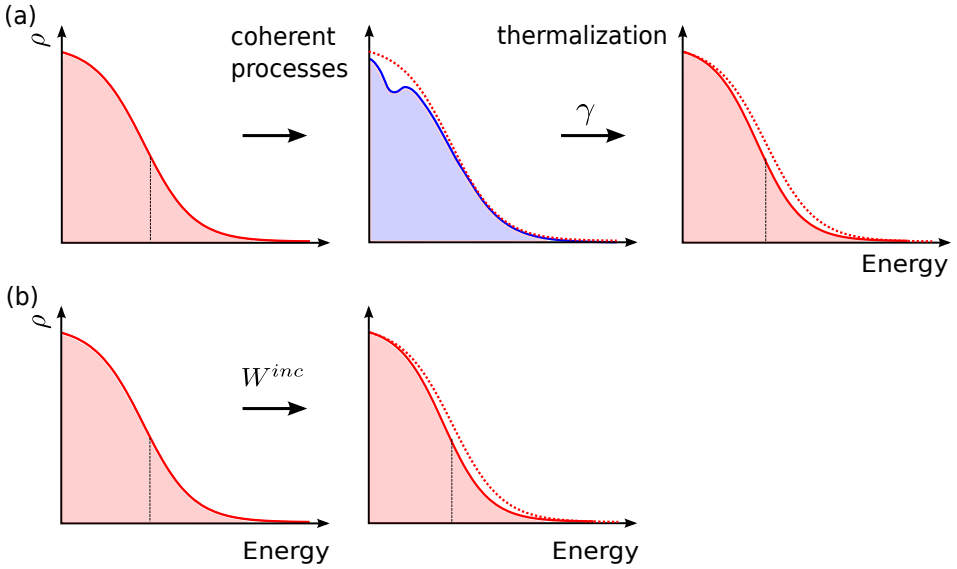

Figure 2.3: Schematic illustration of the coherent and incoherent interactions. (a) Coherent processes lead to a non-equilibrium distribution of QW charge carriers. Scattering mechanisms thermalize the non-equilibrium distribution with relaxation rate $\gamma = \frac{1}{T_2^{QW}}$. (b) Incoherent processes change the particle number and thus the chemical potential while maintaining a thermal distribution.

As in the case of the QDs, the macroscopic polarization p^{QW} stemming from the interaction of the light-field with the QW states is given by a summation over all k-states.

$$P^{QW} = \frac{1}{h^{QW}A} 2 \sum_k p_k = \frac{2}{h^{QW}A} \frac{A}{(2\pi)^2} \int d^2k \, p_k = \frac{2}{4\pi^2 h^{QW}} \int d^2k \, p_k, \tag{2.69}$$

where A denotes the in-plane area of the active region.

2.3.3 Incoherent description

For the case of weak dipole interactions of the QW states with the light field the polarization dynamics of the QW can be neglected. In the limiting case of zero dipole interaction, $\mu^k = 0$, Eqs. (2.56)- (2.58) reduce to the following rate equations

$$\frac{\partial w_b}{\partial t} = \frac{\partial}{\partial t} \left(\frac{2}{A} \sum_k f_k^b \right) = \frac{2}{A} \sum_k \Delta_k^b = \frac{j(t)}{e_0} - \tilde{R}_{sp} - 2 \sum_{m,j} N^j \frac{\partial f_{b,m}^j}{\partial t} \bigg|_{col}. \tag{2.70}$$

The separate incoherent contributions are the electrical injection term is $j(t)/e_0$, the spontaneous emission rate in the QW $\tilde{R}_{sp}$ and the QD-QW Auger scattering contributions $2\sum_{m,j} N^j (\partial/\partial t) f^j_{b,m}|_{col}$.

Chapter 3

Coulomb correlation contributions

A microscopic description of the Coulomb interaction has been proven successfull in the modeling of bulk and QW semiconductor based laser [CHO99] and amplifier devices [KNO92, KNO93]. Many-body effects in QD-QW systems have been found to play a crucial role in understanding the turn-on dynamics and modulation response [LUE08, KIM10a, LIN10, LUE11] as well as the large signal response [LUE10a] and the linewidth enhancement factor [SCH02j] of QD lasers.

While the optical transitions in QD lasers and amplifiers involve the localized QD states, the pump process in electrically injected devices generates carriers in the QW. Hence the carrier dynamics in QD based devices crucially depends on the capture of carriers from the QW to the discrete QD states as well as on the relaxation of carriers between the discrete QD states. An important question addressed in Chapter 4 is to what extent these processes limit the gain recovery speed of a QD based amplifier.

The aim of this chapter is to study the Coulomb effects present in a QD based optical amplifier. Thus an ensemble of QDs is considered, which is embedded in a surrounding QW and the in-plane dimensions are assumed to be that of a typical optical device. In order to cover a broad range of operating conditions of a QD SOA the results are presented in dependence of the 2D QW density and temperature.

3.1 Matrix elements and wave function model

The matrix elements of the bare Coulomb potential

$$V_{\nu_1\nu_3\nu_2\nu} = \int d^3r d^3r' \Psi^*_{\nu}(\mathbf{r})\Psi^*_{\nu_2}(\mathbf{r}')\frac{e_0^2}{4\pi\epsilon_0\epsilon_{bg}|\mathbf{r}-\mathbf{r}'|}\Psi_{\nu_1}(\mathbf{r})\Psi_{\nu_3}(\mathbf{r}') \tag{3.1}$$

involve the single-particle wave functions $\Psi_v(\mathbf{r})$ of electrons and holes in the confinement potential of the QD-QW system.

For lens-shaped QDs the wave functions can be separated into an in-plane component and a perpendicular y-component [WOJ96] $\Psi_\nu(\mathbf{r}) = \phi^b_l(\rho)\xi^b_\sigma(y)u_b(\mathbf{r})$, where $u_b(\mathbf{r})$ are the

lattice Bloch functions and l and σ the quantum numbers of the in-plane and y-component wave functions, respectively, Eq. (3.1) can be expressed as [NIE04]

$$V_{\nu_1\nu_3\nu_2\nu} = \frac{1}{A}\sum_q V^{b,b_2}_{\sigma_1\sigma_3\sigma_2\sigma}\delta_{b,b_1}\delta_{b_2,b_3} \times \langle\phi^b_l|e^{-i\mathbf{q}\cdot\rho}|\phi^{b_1}_{l_1}\rangle\langle\phi^{b_2}_{l_2}|e^{i\mathbf{q}\cdot\rho}|\phi^{b_3}_{l_3}\rangle, \tag{3.2}$$

where $\mathbf{q}$ is the two-dimensional in-plane carrier momentum and

$$V^{b,b_2}_{\sigma_1\sigma_3\sigma_2\sigma} = \frac{e_0^2}{2\epsilon_0\epsilon_{bg}q}\int dydy' \times \xi^b_\sigma(y)^*\xi^{b'}_{\sigma_2}(y')^* e^{-q|y-y'|}\xi^{b'}_{\sigma_3}(y)\xi^b_{\sigma_1}(y') \tag{3.3}$$

is the in-plane Coulomb matrix element.

3.1.1 QD wave functions

In a simple approach to the QD confinement we approximate the y-confinement potential by an infinite-height potential barrier of width $L = 2\,h^{QW}$, where h^{QW} is the thickness of one QW layer [LIU94, WAL04a]. With this ansatz, analytic wavefunctions in y-direction can be used and also the overlap integral from Eq. (3.3) can be solved analytically. For a more rigorous treatment one would need to solve a 1D Schrödinger equation for a finite height potential barrier.

For the in-plane confinement potential of the QDs the model of a two-dimensional harmonic oscillator is adopted, which allows for an analytic solution of the wave function overlap integrals in Eq. (3.2). The calculation of realistic single-particle wave functions is a task of its own and requires detailed knowledge of the QD geometry and the material composition and is beyond the scope of this work.

The two-dimensional electronic in-plane wave functions of the QD GS and ES labeled by $\phi_{n,m}$ with the energy level quantum n and angular momentum quantum number m are given in polar coordinates (ρ, φ) as

$$\phi_{0,0}(\boldsymbol{\rho}) = \frac{\beta}{\sqrt{\pi}}\,\exp\left\{-\frac{\beta^2\rho^2}{2}\right\}, \tag{3.4}$$

$$\phi_{1,\pm1}(\boldsymbol{\rho}) = \frac{\beta^2}{\sqrt{\pi}}\rho\,\exp\left\{-\frac{\beta^2\rho^2}{2}\right\}\exp(i\varphi). \tag{3.5}$$

The corresponding energy levels and the energy level spacing are given by

$$E_n = \hbar\omega_{_{H0}}(n+1), \tag{3.6}$$

$$\hbar\omega_{_{HO}} = \hbar^2\beta^2 m^*, \tag{3.7}$$

with effective mass m^* and oscillator strength ω_{HO}.

3.1.2 Orthogonalized plane waves

In a (homogeneous) quantum well devoid of QDs the in-plane component of the QW wave functions are in good approximation given by plane waves

$$\phi^0_{\mathbf{k}}(\boldsymbol{\rho}) = (1/\sqrt{A})e^{i\mathbf{k}\cdot\boldsymbol{\rho}}. \tag{3.8}$$

In the presence of QDs however, the QW wave-functions are altered in the vicinity of the QDs due to local changes in the QD-QW potential and the set of plane waves and QD wave functions does not represent an orthonormal basis of the combined QD-QW system.

To describe the combined system one can construct QW wave functions by projecting plane waves onto the subspace orthogonal to the QD wave functions [SCH01d, NIE04, MAJ10], so-called orthogonalizedplane waves (OPW). A detailed description of the orthogonalzation procedure can be found in Refs. [NIE04, MAJ10]. A short outline of the orthogonalization procedure is presented in the following. For the case of 2D harmonic oscillator eigenfunctions used as QD wavefunctions all the resulting overlap integrals appearing in Eq. (3.2) can be solved analytically.

$$|\phi_{\mathbf{k}}\rangle = \frac{1}{N_{\mathbf{k}}}(|\phi^0_{\mathbf{k}}\rangle - \sum_{\alpha}|\phi_\alpha\rangle\langle\phi_\alpha|\phi^0_{\mathbf{k}}\rangle). \tag{3.9}$$

Here $N_{\mathbf{k}}$ is the normalization constant ensuring $\langle\phi_{\mathbf{k}}|\phi_{\mathbf{k}}\rangle = 1$. The summation runs over all localized QD states. Assuming an ensemble of identical QDs located at positions $\{\boldsymbol{\rho}_i\}$ with non-overlapping wave functions $\phi^i_m(\boldsymbol{\rho})$ the summation runs over $\alpha = (m, i)$. By construction, the OPW states are orthogonal to all QD states $\langle\phi_\alpha|\phi_{\mathbf{k}}\rangle$. For different OPW states we evaluate

$$\langle\phi_{\mathbf{k}}|\phi_{\mathbf{k}'}\rangle = \frac{1}{N_{\mathbf{k}}N_{\mathbf{k}'}}\left(\delta_{\mathbf{k},\mathbf{k}'} - \sum_{\alpha}\langle\phi^0_{\mathbf{k}}|\phi_\alpha\rangle\langle\phi_\alpha|\phi^0_{\mathbf{k}'}\rangle\right) \tag{3.10}$$

The inner product between a plane wave and and a QD wave function at position ρ_i gives

$$\begin{aligned}\langle\phi_{\alpha=(m,\rho_i)}|\phi_{\mathbf{k}}\rangle &= \int d^2\rho\,\phi_m(\rho-\rho_i)e^{i\mathbf{k}\rho} \\ &= \int d^2\rho\,\phi_m(\rho)e^{i\mathbf{k}(\rho+\rho_i)} = \langle\phi_{\alpha=(m,0)}|\phi_{\mathbf{k}}\rangle e^{i\mathbf{k}\rho_i}\end{aligned} \tag{3.11}$$

With this Eq. (3.10) can be rewritten as

$$\langle\phi_{\mathbf{k}}|\phi_{\mathbf{k}'}\rangle = \frac{1}{N_{\mathbf{k}}N_{\mathbf{k}'}}\left(\delta_{\mathbf{k},\mathbf{k}'} - \sum_{m,i}\langle\phi^0_{\mathbf{k}}|\phi_{(m,0)}\rangle\langle\phi_{(m,0)}|\phi^0_{\mathbf{k}'}\rangle e^{i(\mathbf{k}'-\mathbf{k})\rho_i}\right) \tag{3.12}$$

In the large area limit, meaning that both the in-plane area $A \to \infty$ and the number of QDs $N \to \infty$ such that the QD density remains constant ($N/A = const$) the phase factors in Eq. (3.12) cancel out on average except for $\mathbf{k} = \mathbf{k}'$. In that case the orthogonality of different OPW states of an ensemble of randomly distributed QDs is restored and orthonormality is achieved with the normalization constant

$$N_{\mathbf{k}} = \sqrt{1 - N^{QD}\sum_{m}|\langle\phi^0_{\mathbf{k}}|\phi_{(m,0)}\rangle|^2}. \tag{3.13}$$

3.2 Plasma screening

Am important many body effect present in systems with a high carrier density, such as QD SOAs or QD lasers, is the screening of the Coulomb interaction due to the surrounding carrier plasma. The bare Coulomb potential is often found to overestimate the Coulomb interaction, since the carrier plasma effectively screens the interaction.

Within the context of the present work plasma screening is included via the Lindhard Formula for the longitudinal dielectric function given by [HAU04]

$$\epsilon(q,\omega) = 1 - V_q\sum_{k,b}\frac{f(\varepsilon_{b,\mathbf{k}-\mathbf{q}},\mu_b,T_b) - f(\varepsilon_{b,\mathbf{k}},\mu_b,T_b)}{\hbar(\omega+i\delta) + \varepsilon_{b,\mathbf{k}-\mathbf{q}} - \varepsilon_{b,\mathbf{k}}}, \tag{3.14}$$

where $b = \{e,h\}$ takes into account screening effects due to the electron (e) and hole (h) plasma seperately. The charge carrier distributions are taken as Fermi distributions assuming equilibrium within the QW. For the implementation of screening the frequency dependence of the screening is neglected by applying the limit $\omega + i\delta \to 0$. The Lindhard formula becomes

$$\epsilon(q,\omega\to 0) = 1 - V_q\sum_{k,b}\frac{f(\varepsilon_{b,\mathbf{k}-\mathbf{q}},\mu_b,T_b) - f(\varepsilon_{b,\mathbf{k}},\mu_b,T_b)}{\varepsilon_{b,\mathbf{k}-\mathbf{q}} - \varepsilon_{b,\mathbf{k}}}, \tag{3.15}$$

Furthermore, only the long-wavelength limit ($q \to 0$) is considered. With this approximation Eq. (3.14) can be further simplified by expanding $f(\varepsilon_{b,\mathbf{k}-\mathbf{q}},\mu_b,T_b)$ and $\varepsilon_{\mathbf{k}-\mathbf{q}}$ around $\mathbf{q} = 0$ and keeping only the lowest order terms of the expansion. For the denominator

one obtains

$$\varepsilon_{b,\mathbf{k}-\mathbf{q}} - \varepsilon_{b,\mathbf{k}} = \frac{\hbar^2}{2m_b}(k^2 - 2\mathbf{k}\cdot\mathbf{q} + q^2) - \frac{\hbar^2 k^2}{2m_b} \simeq -\frac{\hbar^2 \mathbf{k}\cdot\mathbf{q}}{m_b} \tag{3.16}$$

and for the numerator

$$f_{\mathbf{k}-\mathbf{q}} - f_{\mathbf{k}} = f_{\mathbf{k}} - \mathbf{q}\cdot\nabla_{\mathbf{k}} f_{\mathbf{k}} + O(q^2) \simeq -\mathbf{q}\cdot\nabla_{\mathbf{k}} f_{\mathbf{k}} \tag{3.17}$$

Inserting Eqs (3.16) and (3.17) into Eq (3.15) one obtains

$$\epsilon(\mathbf{q},0) = 1 - V_{\mathbf{q}} \sum_{b,\mathbf{k},i} \frac{-q_i \frac{\partial f}{\partial k_i}}{-\frac{\hbar^2 \mathbf{k}\cdot\mathbf{q}}{m_b}} = 1 - V_{\mathbf{q}} \sum_{b,\mathbf{k},i} \frac{q_i \frac{\partial f}{\partial k_i}}{\frac{\hbar^2 \mathbf{k}\cdot\mathbf{q}}{m_b}} \tag{3.18}$$

Assuming a thermal distribution of the QW states one gets

$$\sum_i q_i \frac{\partial f_b^k}{\partial k_i} = -\sum_{b,i} q_i \frac{\partial f_b^k}{\partial F_b}\frac{\partial \varepsilon_{b,k}}{\partial k_i} = -\sum_{b,i} q_i k_i \frac{\hbar^2}{m_b}\frac{\partial f_b^k}{\partial F_b}. \tag{3.19}$$

Here, $\varepsilon_{b,k} = \frac{\hbar^2 k^2}{2m_b}$ and $\frac{\partial \varepsilon_k}{\partial k_i} = \frac{\hbar^2 k_i}{m_b}$

$$\epsilon(q,0) = 1 + V_q \sum_{b,k,i} \frac{q_i k_i \frac{\hbar^2}{m}\frac{\partial f_b^k}{\partial F_b}}{\frac{\hbar^2 \mathbf{k}\cdot\mathbf{q}}{m}} = 1 + V_q \sum_{b,k} \frac{\partial f_b^k}{\partial F_b} = 1 + \frac{e_0^2}{2\epsilon_0 \epsilon_{bg} A q} \sum_b \frac{\partial}{\partial F_b} \sum_k f_b^k \tag{3.20}$$

$$= 1 + \frac{e_0^2}{2\epsilon_0 \epsilon_{bg} q} \sum_b \frac{\partial w_b}{\partial F_b} \equiv 1 + \frac{\kappa}{q}. \tag{3.21}$$

Here, w_b is the 2D QW carrier density and $\kappa = \sum_b \frac{e_0^2}{2\epsilon_0\epsilon_{bg}}\frac{\partial w_b}{\partial F_b}$ is the 2D inverse screening length. With this the 2D statically screened Coulomb potential is given by

$$W_s(q,\omega=0) \equiv \frac{V_q}{\epsilon(q,\omega=0)} = \frac{e_0^2}{2\epsilon_0\epsilon_{bg} A q}\frac{q}{q+\kappa} = \frac{e_0^2}{2\epsilon_0\epsilon_{bg} A}\frac{1}{q+\kappa} \tag{3.22}$$

The 2D quasi-Fermi level in the QW can be expressed anaytically as

$$F_b^{QW}(w_b, T) = k_B T \ln\left[\exp(\hbar^2 \beta \pi w_b / m_b) - 1\right]. \tag{3.23}$$

This allows to explicitly express the screening wave number as follows

$$\kappa = \frac{e_0^2}{2\epsilon_0\epsilon_{bg}} \sum_b \frac{\partial w_b}{\partial F_b} = \frac{e_0^2}{2\epsilon_0\epsilon_{bg}} \sum_b \frac{m_b}{\hbar^2 \pi}(1 - e^{-\hbar^2\beta\pi w_b/m_b}) = \sum_b \frac{m_b e_0^2}{2\pi\epsilon_0\epsilon_{bg}\hbar^2} f_b^{k=0}. \tag{3.24}$$

3.3 First order Coulomb contributions

In this section the first order Coulomb effects will be discussed. As introduced in section 2.2.2 the Hartree-Fock approximation is a common method to resolve the so-called hierarchy problem arising when evaluating Heisenbergs equations of motion including Coulomb interaction contributions. Specifically, the Coulomb interaction leads to an energy renormalization of the single-particle states of the electronic system.

3.3.1 Hartree-Fock approximation

In Hartree-Fock approximation the energy renormalization $\Delta\varepsilon_\nu^{HF}$ for an arbitrary QD or QW state ν with spin s is given by

$$\tilde{\varepsilon}_\nu = \varepsilon_\nu + \Delta\varepsilon_\nu^{HF}, \tag{3.25}$$

where ε_ν is the free carrier single particle energy and $\Delta\varepsilon_\nu^{HF}$ the Hartree Fock term. The spin index s is in the following tacitly included in ν. The Hartree-Fock term consists of a direct (Hartree) term and an exchange (Fock) term

$$\begin{aligned}\Delta\varepsilon_\nu^{HF} &= \Delta\varepsilon_\nu^{H} + \delta_{s,s'}\Delta\varepsilon_\nu^{F} \\ &= \sum_{\nu'} \left[V_{\nu'\nu\nu\nu'} - V_{\nu'\nu\nu'\nu}\right] f_{\nu'}.\end{aligned} \tag{3.26}$$

The summation over ν' involves all possible states, e.g., QD as well as QW states with $V_{\nu'\nu\nu\nu'}$ being the Coulomb matrix element defined in Eq. (2.30). The first term in Eq. (3.26) is the direct (Hartree) part resulting from direct Coulomb interaction and the second term is the exchange (Fock) part that results by assuming antisymmetric wavefunctions and thus by taking the Pauli principle into account.

3.3.2 Screened Coulomb interaction

To account for plasma screening effects the bare Coulomb potential V is replaced with the screened Coulomb potential W derived in section 3.2 in the direct and exchange terms

$$\begin{aligned}\Delta\varepsilon_\nu^{HF} \to \Delta\varepsilon_\nu^{SHF} &= \Delta\varepsilon_\nu^{SH} + \Delta\varepsilon_\nu^{SF} \\ &= \sum_{\nu'} \left[W_{\nu'\nu\nu\nu'} - \delta_{s,s'} W_{\nu'\nu\nu'\nu}\right] f_{\nu'}.\end{aligned} \tag{3.27}$$

3.3.3 Coulomb hole

The HF approximation is only a first correction to the Coulomb correlation contributions and further corrections can lead to significant improvements of the HF estimate. A frequently used modification to the bare HF contributions for high-density plasma excitations are the above shown screened interaction and Coulomb hole contributions.

The term Coulomb hole refers to the fact that two electrons cannot occupy the same spatial position due to the repulsive Coulomb force. A wavefunction built up as a Hartree product does not restore this property and the probability of finding two electrons at the same spatial position is not zero. The screening of the Coulomb interaction , however, weakens the repulsive Coulomb force and thus dimishes the effect of the Coulomb hole, yielding a reduction of the total energy equal to the difference of the screened and the unscreened Coulomb potential at zero distance [HAU94]:

$$\Delta\varepsilon_{\nu}^{CH} = \lim_{|r|\to 0} \frac{1}{2} \left[W(|r|) - V(|r|) \right] \tag{3.28}$$

A similar effect due to the fact that two electrons with equal spins cannot overlap spatially is accounted for by the exchange (Fock) term of the Hartree-Fock approximation. This is referred to as the Fermi or exchange hole.

Throughout this work Coulomb renormalizations of the single particle energies are neglected. Instead, the focus of this work lies on the second order Coulomb scattering processes between the QD and QW states, which will be presented in the next section. The calculation of Coulomb renormalizations for QD-QW systems is given in App E. Typically, the Coulomb renormalizations lead to a band gap shrinkage [NIE04, LIN11b].

3.4 Microscopic theory of carrier-carrier scattering

The screened Hartree-Fock terms and Coulomb hole contributions are first order contributions in terms of the Coulomb potential. The second order Coulomb contributions are the carrier-carrier scattering contributions presented in this section. A schematic energy diagram of the given QD-QW structure is shown in Fig. 3.1. It indicates the energy in growth direction (y) of the QD-QW structure. The quasi-continuum of QW states is marked by the gray shaded areas, respectively, whereas the confined QD ground state (GS) and first excited state (ES) are indicated by the solid and dashed gray lines, respectively. The energy offsets of the electron and hole QD ground states to the QW band edge are labeled by ΔE_e and ΔE_h and the energy separation between the ground and excited state electron and hole levels is denoted by Δ_e and Δ_h. The black arrows

in Fig. 3.1 indicate the possible scattering induced carrier capture processes from the QW to the bound QD states as well as intradot relaxation processes (Auger electrons are omitted).

3.4.1 Born-Markov approximation - Boltzmann equation

The collision terms in Eqs. (2.49) - (2.50) in the Markov limit up to second order in the screened Coulomb potential W are given by [NIE04, MAJ10]:

$$\left.\frac{\partial f^j_{b,m}}{\partial t}\right|_{col} = \frac{2\pi}{\hbar}\sum_{\nu_1\nu_2\nu_3} W_{\nu_1\nu_3\nu_2 m}\left[W^*_{\nu_1\nu_3\nu_2 m} - \delta_{b,b'}W^*_{\nu_3\nu_1\nu_2 m}\right] \times \delta\left(\varepsilon_m - \varepsilon_{\nu_1} + \varepsilon_{\nu_2} - \varepsilon_{\nu_3}\right) \times \left[f_{\nu_1}(1-f_{\nu_2})f_{\nu_3}(1-f^j_{b,m}) - (1-f_{\nu_1})f_{\nu_2}(1-f_{\nu_3})f^j_{b,m}\right]. \tag{3.29}$$

with $b, b' \in \{e, h\}$. The above equation is a Boltzmann equation of the form

$$\left.\frac{\partial f^j_{b,m}}{\partial t}\right|_{col} = S^{in}_{b,m}(1-f^j_{b,m}) - S^{out}_{b,m}f^j_{b,m}, \tag{3.30}$$

where the sums over products of matrix elements, occupation factors, and the energy conserving δ-function is given by the general scattering expression S. In these Auger-type scattering events two carriers scatter from initial states ν_1 (with energy ε_{ν_1}) and ν_3 to final states m and ν_2, respectively, and vice versa. The calculation involves screened Coulomb matrix elements for the direct and exchange interaction $|W_{\nu_1\nu_3\nu_2 m}|^2$ and $W_{\nu_1\nu_3\nu_2 m}W^*_{\nu_3\nu_1\nu_2 m}$, respectively. The index m represents the quantum number of the 2D angular momentum of the confined QD states, $m = 0$ and $m = \pm 1$ for the GS and ES, respectively. The states of interest are always QD states denoted by the angular momentum quantum number m. The summation runs over all other states, QD states as well as QW states. The δ-function in Eq. (3.29) ensures energy conservation. The occupation probability of state ν_i is denoted by f_{ν_i}.

In the following Eq. (3.29) is systematically split into different contributions originating from different scattering processes, i.e., direct capture processes and relaxation type processes

$$\left.\frac{\partial f^j_{b,m}}{\partial t}\right|_{col} = R^{cap} + R^{rel} \tag{3.31}$$

and the different contributions are determined separately. Figure 3.2 gives a systematic overview of the possible QW-QD Auger processes for a QD with two bound energy states. The Auger scattering processes are grouped into two main categories, direct capture (and

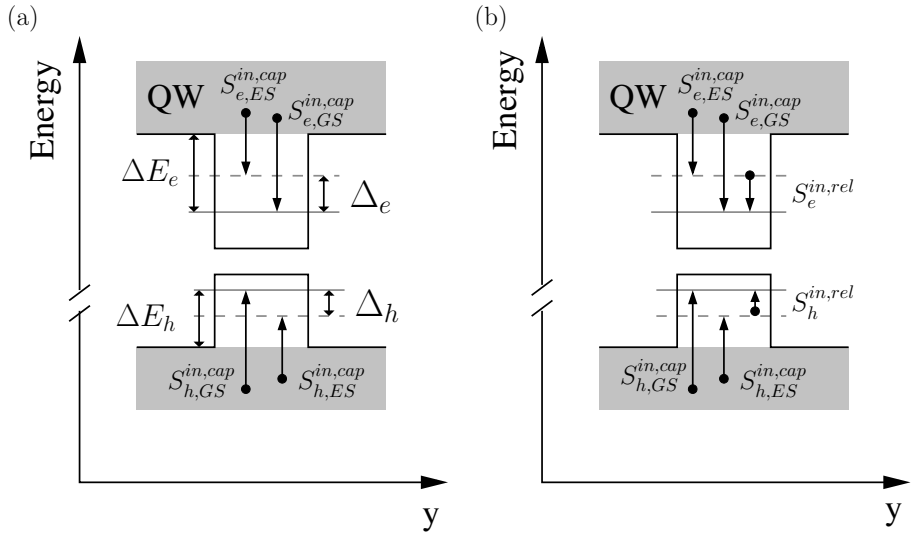

Figure 3.1: Schematic energy diagram of the QW-QD system. (a): Direct scattering processes between QW and QD electron and hole states indicated by the black arrows. The offset energies of the QD electron and hole GS with respect to the QW band edge are labeled by ΔE_e and ΔE_h, respectively. The enery separation of the electron and hole GS and ES are given by Δ_e and Δ_h, respectively. (b): Direct and relaxation type capture processes indicated by the black arrows.

escape) processes and relaxation processes shown in Fig. 3.2(a) and (b), respectively. The arrows in Fig. 3.2 indicate electron transitions in the QD-QW system. An Auger process can be of pure ($e-e$ of $h-h$) and a mixed ($e-h$ or $h-e$). The pure electron processes are indicated in panels I, III of Figs. 3.2 and the mixed processes are shown in panels II, IV. In Fig.3.2 the respective hole processes are omitted, but the same scheme applies for holes. In total this makes a number of sixteen different scattering processes. The scattering rates are evaluated for quasi-equilibrium between the QW and QD subsystems. The consideration of pure and mixed processes results in a dependency of the scattering rates on both the electron and hole QW charge carrier density w_e and w_h respectively. In the following the separate contributions of each type of process will be discussed.

3.4.2 Direct capture

A direct capture process describes the Coulomb assisted transition of charge carrier from a QW state to a QD state accompanied by an intraband QW transition. The contribution to Eq. (3.29) from direct capture processes can be expressed as the following Boltzmann

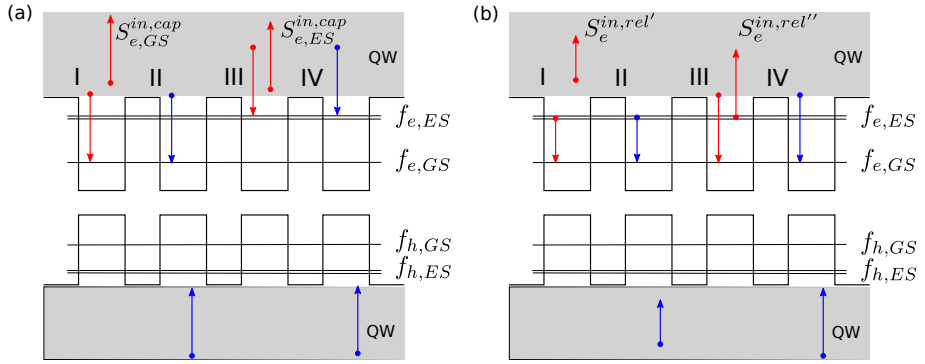

Figure 3.2: (a) Direct electron capture processes from the QW to the QD ground state (I,II) and first excited state (III,IV). Panels I, III and panels II, IV show pure e-e and mixed e-h scattering processes, respectively. (c) Electron relaxation processes to the QD ground state. (blue arrows denote electron transitions also in the valence band).

equation

$$R_b^{cap} = S_{b,m}^{in,cap}(1 - f_{b,m}^j) - S_{b,m}^{out,cap} f_{b,m}^j, \tag{3.32}$$

with the in-scattering rate given by the following expression

$$\begin{aligned} S_{b,m}^{in,cap} = \frac{2\pi}{\hbar} \sum_{\mathbf{k}_1\mathbf{k}_2\mathbf{k}_3 b'} W_{\mathbf{k}_1\mathbf{k}_3\mathbf{k}_2 m} \left[2W^*_{\mathbf{k}_1\mathbf{k}_3\mathbf{k}_2 m} - \delta_{b,b'} W^*_{\mathbf{k}_3\mathbf{k}_1\mathbf{k}_2 m} \right] \\ \times \delta\left(\varepsilon_m^b - \varepsilon_{\mathbf{k}_1}^b + \varepsilon_{\mathbf{k}_2}^{b'} - \varepsilon_{\mathbf{k}_3}^{b'} \right) f_{\mathbf{k}_1}(1 - f_{\mathbf{k}_2}) f_{\mathbf{k}_3} \,. \end{aligned} \tag{3.33}$$

3.4.3 Relaxation processes

A relaxation process is given by the redistribution of carriers within the intra-QD levels. This class of scattering processes can be further subdivided into two types of processes involving either one QW-QD transition accompanied by an intra-QW transition ($m_1 \to m$, $\mathbf{k}_3 \to \mathbf{k}_2$) or one QW-QD transition to an energetically low QD level (QD ground state $m = 0$) together with a QD-QW transition from an energetically higher QD level (QD excited state $m = \pm 1$) to the QW ($\mathbf{k}_1 \to m$, $\mathbf{k}_2 \to m_1$). Labeling the scattering contributions of the first type of relaxation process $R_b^{rel'}$ and of the latter process $R_b^{rel''}$ one obtains for the total rate $R_b^{rel} = R_b^{rel'} + R_b^{rel''}$ The first relaxation type scattering process ($R^{rel'}$) obeys the following Boltzmann equation

$$R_b^{rel'} = S_{b,m}^{in,rel'} f_{b,m_1}^j (1 - f_{b,m}^j) - S_{b,m}^{out,rel'} (1 - f_{b,m_1}^j) f_{b,m}^j \tag{3.34}$$

with the in-scattering rate

$$S_{b,m}^{in,rel'} = \frac{2\pi}{\hbar} \sum_{\mathbf{k}_2\mathbf{k}_3 b'} W_{m_1\mathbf{k}_3\mathbf{k}_2 m} \left[2W^*_{m_1\mathbf{k}_3\mathbf{k}_2 m} - \delta_{b,b'} W^*_{\mathbf{k}_3 m_1 \mathbf{k}_2 m}\right] \times \delta\left(\varepsilon^b_m - \varepsilon^b_{m_1} + \varepsilon^{b'}_{\mathbf{k}_2} - \varepsilon^{b'}_{\mathbf{k}_3}\right)(1 - f_{\mathbf{k}_2}) f_{\mathbf{k}_3}. \tag{3.35}$$

The scattering rates for the second type of process ($R_b^{rel''}$) can be obtained in a similar fashion as Eq. (3.35)

$$S_{bb',m}^{in,rel''} = \frac{2\pi}{\hbar} \sum_{\mathbf{k}_1\mathbf{k}_2} W^{bb'}_{\mathbf{k}_1 m_1 \mathbf{k}_2 m} \left[2W^{*\,bb'}_{\mathbf{k}_1 m_1 \mathbf{k}_2 m} - W^{*\,bb'}_{m_1 \mathbf{k}_1 \mathbf{k}_2 m}\right] \times \delta\left(\varepsilon^b_m - \varepsilon^{b'}_{m_1} + \varepsilon^{b'}_{\mathbf{k}_2} - \varepsilon^b_{\mathbf{k}_1}\right)(1 - f^{b'}_{\mathbf{k}_2}) f^b_{\mathbf{k}_1} \tag{3.36}$$

$$R_b^{rel''} = \sum_{b'} S^{in,rel''}_{bb',m} f^j_{b',m_1}(1 - f^j_{b,m}) - S^{out,rel''}_{bb',m}(1 - f^j_{b',m_1}) f^j_{b,m}. \tag{3.37}$$

The out-scattering rates are determined by replacing $f \to (1 - f)$.

3.4.4 Detailed balance

Assuming quasi-equilibrium within the QW states but non-equilibrium between QW and QD electron and hole states the quasi-Fermi distributions within the QW are given by Fermi-Dirac distributions

$$f^b_{\mathbf{k}} = \left[1 + \exp\left(\frac{E^b_{\mathbf{k}} - F^{QW}_b}{k_B T}\right)\right]^{-1}. \tag{3.38}$$

Here, F_b^{QW} is the quasi-Fermi level in the QW carrier reservoir given by Eq. (3.23), k_B is Boltzmann's constant ant T is the temperature. For direct scattering processes the detailed balance condition between in- and out-scattering is [LUE09]:

$$S^{in,cap}_{b,m} = S^{out}_{b,m} \exp\left(\frac{\pm F^{QW}_b \mp \varepsilon^b_m}{k_B T}\right), \tag{3.39}$$

where the upper and lower signs in the exponent are for the case of electrons ($b = e$) and holes ($b = h$), respectively. For relaxation type processes of type rel' the detailed

balance condition reads

$$S_{b,m}^{in,rel'} = S_{b,m}^{out,rel'} \exp\left(-\frac{(\varepsilon_m^b - \varepsilon_{m_1}^b)}{k_B T}\right), \tag{3.40}$$

whereas for relaxation processes of type rel'' it is given by

$$S_{bb',m}^{in,rel''} = S_{bb',m}^{out,rel''} \exp\left(-\frac{(\varepsilon_m^b - \varepsilon_{m_1}^{b'})}{k_B T}\right). \tag{3.41}$$

Note, that the detailed balance condition for the mixed process of Eq. 3.41 involves the single particle energies of QD electron as well as QD hole states, whereas for all other processes only one charge carrier type appears in the detailed balance condition. Using detailed balance one only needs to calculate either in- or out-scattering rates, which is a significant simplification and saves valuable computation time.

3.4.5 Relaxation time approximation

In many theoretical models for optoelectronic devices [CHO05, LIN10, GIO06, GIO08] the scattering contributions are treated in relaxation time approximation. In thermal equilibrium the occupation probabilities become stationary, e.g.,

$$\frac{\partial f_{b,m}^{j,eq}}{\partial t} = 0. \tag{3.42}$$

For perturbations $\delta f_{b,m}^j$ close enough to thermal equilibrium the time evolution from Eq. (3.30) is given by

$$\frac{\partial}{\partial t}\left(f_{b,m}^{j,eq} + \delta f_{b,m}^j\right) = \frac{\partial \delta f_{b,m}^j}{\partial t} = -(S_{b,m}^{in} + S_{b,m}^{out})\delta f_{b,m}^j. \tag{3.43}$$

With a charge carrier lifetime defined by

$$T_{1,m}^b = (S_{b,m}^{in} + S_{b,m}^{out})^{-1} \tag{3.44}$$

a relaxation time approximation is obtained, leading to an exponential decay of the perturbation from thermal equilibrium. The scattering rate expressions $S_{b,m}^{in}$ and $S_{b,m}^{out}$ appearing in Eq. (3.44) contain contributions from direct capture processes and relaxation

processes. The QD ground state scattering expressions are given by

$$S^{in}_{b,GS} = S^{in,cap}_{b,GS} + 2S^{in,rel'}_{b} f^{j}_{b,ES} + 2S^{in,rel''}_{bb} f^{j}_{b,ES} + 2S^{in,rel''}_{bb'} f^{j}_{b',ES}, \tag{3.45}$$
$$S^{out}_{b,GS} = S^{out,cap}_{b,GS} + 2S^{out,rel'}_{b}(1 - f^{j}_{b,ES}) + 2S^{out,rel''}_{bb}(1 - f^{j}_{b,ES}) + 2S^{out,rel''}_{bb'}(1 - f^{j}_{b',ES}).$$

For the QD ES the scattering expressions are given by

$$S^{in}_{b,ES} = S^{in,cap}_{b,ES} + 2S^{out,rel'}_{b} f^{j}_{b,GS} + 2S^{out,rel''}_{bb} f^{j}_{b,GS} + 2S^{out,rel''}_{bb'} f^{j}_{b',GS}, \tag{3.46}$$
$$S^{out}_{b,ES} = S^{out,cap}_{b,ES} + 2S^{in,rel'}_{b}(1 - f^{j}_{b,GS}) + 2S^{in,rel''}_{bb}(1 - f^{j}_{b,GS}) + 2S^{in,rel''}_{bb'}(1 - f^{j}_{b',GS}).$$

The factor of 2 in the contributions of relaxation type appears due to the degeneracy of the QD ES. Due to the relaxation rates the expressions for the charge carrier lifetimes also contain occupation factors of the QD levels.

3.5 Results for an InGaAs-GaAs quantum dot quantum well system

In this section the numerical results for the scattering rates of the considered QD-QW system are presented. The conduction and valence bands of the QW are approximated as parabolic bands with effective masses m_e and m_h. The exact calculation of the band

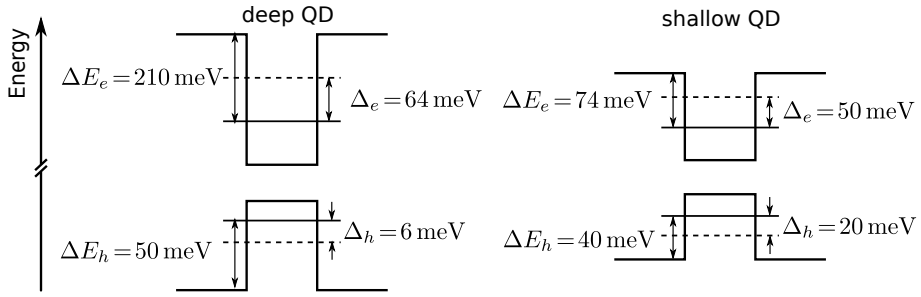

Figure 3.3: Schematic diagram of the considered deep QD and shallow QD structures.

structure of the QD-QW material system is a complex task on its own and is beyond the scope of this work. To gain insight into the qualitative changes resulting for different band structure parameters without performing complex ab initio calculations (for example via $\mathbf{k} \cdot \mathbf{p}$ calculations [POH05, SEG05]) the QD band offset energies with respect to the QW and the QD oscillator strength within the 2D harmonic oscillator ansatz are considered for two extremal cases of very deep QDs on the one hand and shallow QDs on the other

hand. The energetic configuration of the different QD types is shown in Fig. 3.3 and the respective parameters are given in Table 3.1. Here, ΔE_e (ΔE_h) denotes the energy separation of the QD GS electron (hole) energy level to the QW conduction (valence) band edge and Δ_e (Δ_h) is the energy level spacing of the electron (hole) QD GS and ES energy levels.

Table 3.1: Numerical parameters used for the calculation of scattering rates.

shallow dot		deep dot	
$\Delta E_{e,m=0}$	74 meV	$\Delta E_{e,m=0}$	210 meV
$\Delta E_{e,m=\pm1}$	24 meV	$\Delta E_{e,m=\pm1}$	146 meV
$\Delta E_{h,m=0}$	40 meV	$\Delta E_{h,m=0}$	50 meV
$\Delta E_{h,m=\pm1}$	20 meV	$\Delta E_{h,m=\pm1}$	44 meV
Δ_e	50 meV	Δ_e	64 meV
Δ_h	20 meV	Δ_h	6 meV
h^{QW}	4 nm	N^{QD}	10^{11}cm^{-2}
m_e	$0.043\,m_0$	m_h	$0.45\,m_0$

In the following the QDs with energies $\Delta E_e = 74\,\text{meV}$, $\Delta E_h = 40\,\text{meV}$, $\Delta_e = 50\,\text{meV}$, $\Delta_h = 20\,\text{meV}$ are referred to as shallow QDs, whereas the QDs with energies $\Delta E_e = 210\,\text{meV}$, $\Delta E_h = 50\,\text{meV}$, $\Delta_e = 64\,\text{meV}$, $\Delta_h = 6\,\text{meV}$ are referred to as deep QDs (see Fig. Fig. 3.3). The numerical parameters used for the evaluation of the different scattering contributions are listed in Table A.2. Here, h^{QW} is the height of a single QW layer, N^{QD} is the 2D QD density and m_e and m_h are the effective masses of electrons and holes, respectively.

In later parts of this work concentrating on the dynamical aspects of QD SOA devices the different dot configurations will play a role in the analysis of gain recovery and pulse propagation dynamics.

3.5.1 Shallow quantum dot scattering rates

In this section the shallow QD scattering rates are presented. Figure 3.4 shows a plot of the shallow QD direct scattering rates between the 2D QW states and the bound QD states in dependence of the 2D QW electron density for a plasma temperature of $T = 300\,\text{K}$ and a constant ratio of $w_h/w_e = 1$. The direct electron and hole in-scattering

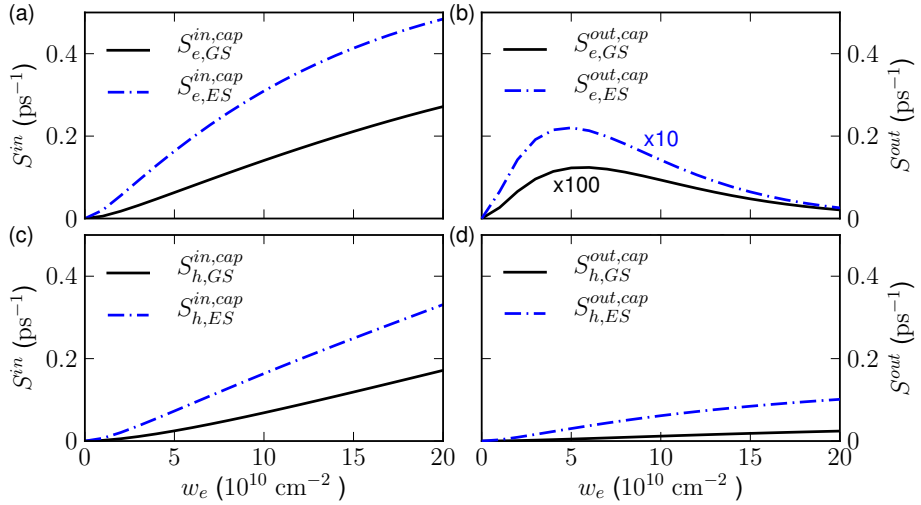

Figure 3.4: Direct Auger scattering rates of the QD-QW system vs. QW carrier density w_e for electrons and holes, respectively, for a 2D plasma temperature of $T = 300\,\mathrm{K}$ and a fixed ratio $w_h/w_e = 1.0$ (a): In-scattering rates to the QD ground state (black solid line) and first excited state (blue dash-dotted line). (b): Electon out-scattering rates given by detailed balance from Eq. (3.39) (c) and (d): Same as (a) and (b) for holes. Other parameters as in Table 3.1.

rates from the QW states to the bound QD states assisted by Auger electrons in the QW are shown in Fig. 3.4(a) and (c), respectively, while the direct out-scattering rates for electrons and holes obtained from the detailed balance condition from Eq. (3.39) are shown in Fig. 3.4(b) and (d). At zero QW density no states in the QW are occupied and therefore the scattering rate is zero due to the lack of possible scattering partners. With increasing QW charge carrier density the electron and hole in-scattering rates at first increase due to the increased availability of scattering partners. For higher QW densities, however, Pauli blocking of the final scattering states in the QW leads to a decrease of the scattering rate. Quantitatively, the direct capture rates to the QD ES are larger than those to the QD GS. This is due to the fact, that the QD ES is energetically closer to the QW band edge than the QD GS. Furthermore, the direct hole capture rates are smaller than the direct electron capture rates for capture processes to the ground state as well as to the first excited state.

The out-scattering rates for direct capture processes (escape rates) shown in Fig. 3.4(b) and (d) for electrons and holes, respectively, are much smaller than their capture counterparts. In the electron out-scattering rate one can observe a rollover which can be attributed to Pauli blocking.

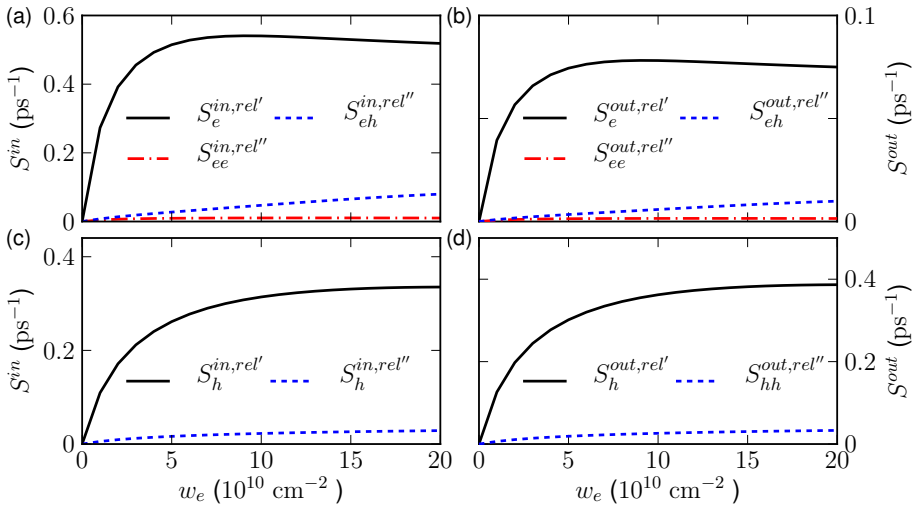

Figure 3.5: Auger scattering rates for relaxation type processes of the QD-QW system vs. QW carrier density w_e for electrons and holes, respectively. The plasma temperature is $T = 300\,\mathrm{K}$ ($w_h/w_e = 1.0$). (a): In-scattering rates. (b): Out-scattering rates given by detailed balance from Eqs. (3.40) and (3.41). Other parameters as in Table 3.1.

The shallow QD scattering rates for processes of relaxation type are depicted in Fig. 3.5. For relaxation processes in-scattering refers to the scattering of a charge carrier into the QD ground state and out-scattering to the opposite process. The dominant relaxation processes for shallow QDs is the rel' process depicted in panel I and II of Fig. 3.2(b), where the intradot relaxation is assisted by a charge carrier transition inside the QW. The scattering rates of this process is much larger compared to the rel'' process, which involves two transitions of charge carriers between QW and QD states.

The electron and hole in- and out-scattering rates of the dominant rel' relaxation process are characterized by a fast increase (from zero at zero QW density) with increasing QW density. At a value of approximately $5 \times 10^{10}\,\mathrm{cm}^{-2}$ the in-and out-scattering rate of electrons has a maximum followed by a slight decrease with increasing QW density. For holes the slope of the initial increase of the in-scattering rate is smaller.

Temperature dependence of scattering

The temperature of the carrier plasma in an optical device may change for example with varying injection strength due to Joule heating or due to free carrier absorption (FCA) within the conduction and valence bands. Therefore it is crucial to study the temperature dependence of carrier-carrier scattering.

To include temperature effects the scattering rates are evaluated for different tem-

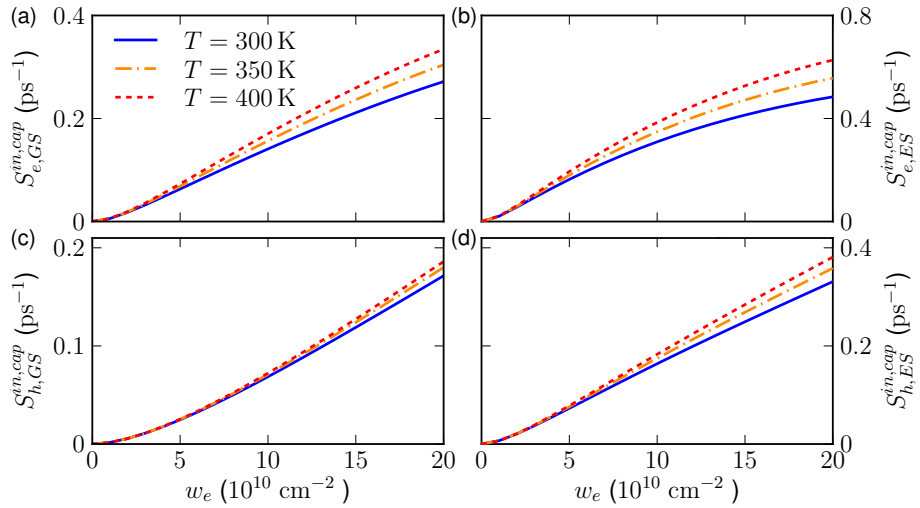

Figure 3.6: Direct in-scattering rates in dependence of the QW electron density and the plasma temperature. (a): Electron scattering rate to the QD ground state. (b) Electron scattering rate to the QD first excited state. (c) and (d): Same as (a) and (b) for holes. The ratio of electron and hole density in the QW is $w_h/w_e = 1.0$, Other parameters as in Table 3.1.

peratures of the quasi-Fermi distributions of the QW states. The temperature dependence of the in-scattering rates is shown in Fig. 3.6 for direct capture processes and in Fig. 3.7 for relaxation type scattering processes. In the considered temperature range from $300 - 400\,\mathrm{K}$ carrier heating leads to an enhanced in-scattering efficiency for all carrier-carrier scattering processes. Comparing Figs. 3.6 and 3.7 one observes that a change in the temperature of the carrier plasma has a larger impact on the relaxation rates, which experience a significant enhancement for elevated temperatures, while the change in the direct capture rates is less prominent.

3.5.2 Deep quantum dot scattering rates

From intuitive grounds one would expect the direct capture (escape) rates to (from) the QD levels to decrease due to the increased band offset of the bound QD states to the QW band edge. For the direct capture rates this behaviour can indeed be observed in Fig. 3.8 (a). The light shaded curves indicate the direct capture rates for shallow QDs for comparison. In contrast to shallow QDs the direct capture rate to the QD ES only merely exceeds the direct capture rate to the QD GS. Also, the respective electron escape rates plotted in Fig. 3.8(b) are approximately three orders of magnitude smaller than for shallow QDs. This can be attributed to the larger band offset of the deep QD

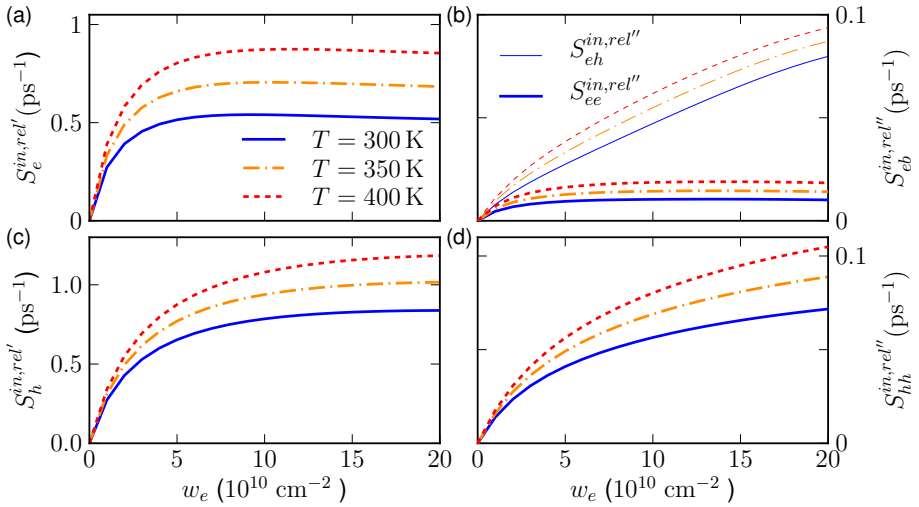

Figure 3.7: Temperature dependence of the scattering rates of relaxation type in dependence of the QW electron density for $T = 300, 350, 400\,\mathrm{K}$. (a): Electron scattering rate of type rel'. (b) Relaxation rates of type rel''. Pure $(e-e)$ electron scattering rate of type rel'' are given by the thick lines and mixed $(e-h)$ electron scattering rates of type rel'' are given by the thin lines. (c): Same as (a) for holes. (d): Hole processes of pure type $(h-h)$ for the process rel''. The ratio of electron and hole density in the QW is $w_h/w_e = 1.0$. Other parameters as in Table 3.1.

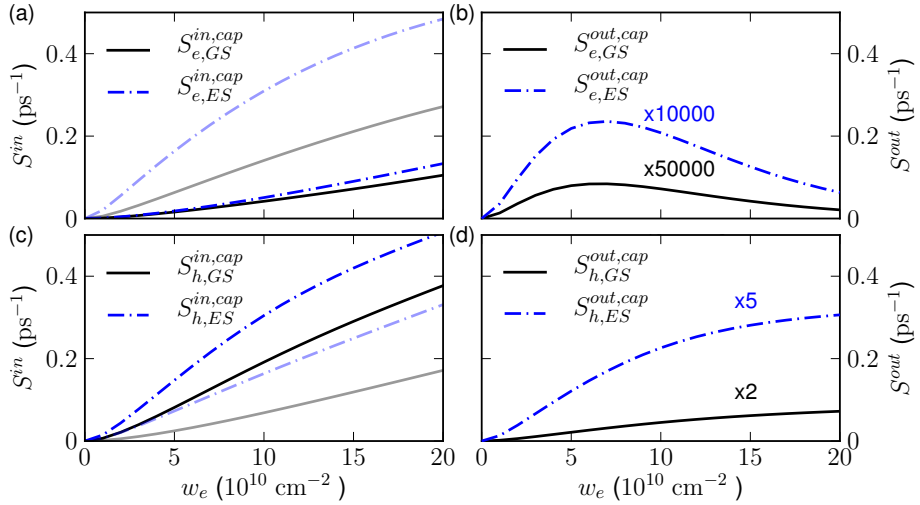

Figure 3.8: Direct capture rates as in Fig. 3.4 for deep QDs. The light shaded curves in panel (a) and (b) indicate the shallow dot scattering rates from Fig. 3.4(a) and (b), respectively.

states to the QW band edge compared to the QW-QD band offset of the shallow QD states. The direct hole capture rates to the QD GS and ES are shown in Fig. 3.8(c) for deep QDs. They exhibit an enhanced in-scattering rate compared to the shallow QD direct capture rates of holes shown in Fig. 3.4(c). The out-scattering rates of direct processes for holes is shown in Fig. 3.8(d). They are comparable to those of shallow QDs (compare Fig. 3.4(d)). An increase of the band-offset energy alone would always lead to a reduction of the scattering efficiency. However, the increased oscillator strength of the in-plane hole wave functions of the deep QDs compared to the shallow QD wave functions influences the Coulomb matrix elements and efficiently compensates the effect attributed to the increased band offset in this case. The scattering rates of relaxation type processes for deep QDs are shown in Fig. 3.9. As a main difference to the relaxation rates of shallow QDs, the dominant relaxation process for deep QDs is the mixed process of type rel'' and no longer the rel' process as in the case of shallow QDs. Overall, the electron relaxation rates for of deep QDs are significantly smaller than those of shallow QDs, while the hole relaxation rates are comparable in magnitude to those of shallow QDs. Due to the larger band offset of the QD states with respect to the QW band edge the electron out-scattering rate shown in Fig. 3.9(b) is greatly reduced compared to the respective rate for shallow QDs.

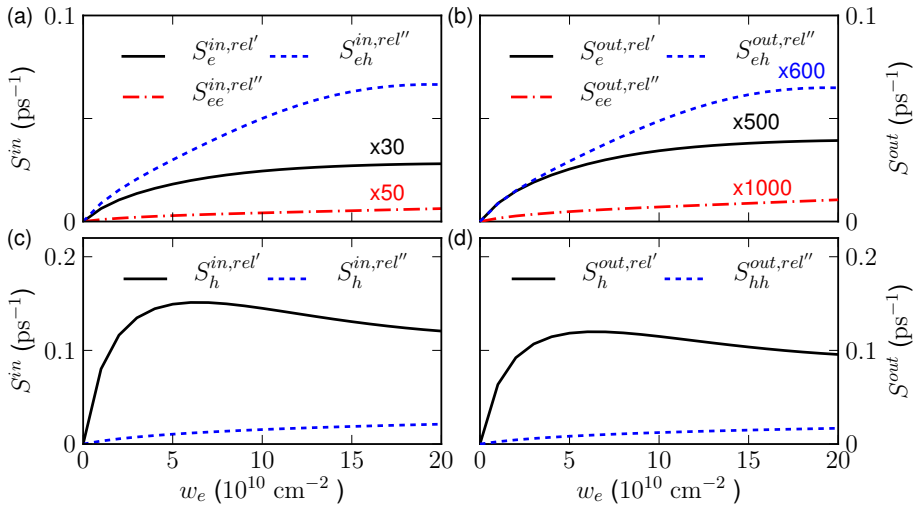

Figure 3.9: Relaxation rates as in Fig. 3.5 for deep QDs.

3.5.3 Quantum dot scattering lifetimes

From the microscopic scattering rates it is possible to extract equilibrium charge carrier lifetimes of the quantum dot ground and first excited state energy levels using Eqs. (3.44)-(3.46). The total QD carrier lifetime $T^b_{1,m}$ of a bound QD state m given by Eq. (3.44) can be split into terms containing direct capture processes and relaxation processes as

$$\frac{1}{T^b_{1,m}} = \frac{1}{T^{b,cap}_{1,m}} + \frac{1}{T^{b,rel}_{1,m}}, \tag{3.47}$$

which enables to quantify the contributions of capture and relaxation processes to the total carrier lifetime.

The resulting scattering lifetimes in dependence of the QW electron density for the shallow and deep dot energy level spacings given in Table 3.1 are shown in Figs. 3.10 and 3.10, respectively. The dependence of the scattering rates on the carrier density in the 2D reservoir leads to density dependent carrier lifetimes. Panels (a) and (b) in Figs 3.10 and 3.11 show the electron lifetimes of the QD ground state and first excited state, whereas panels (c) and (d) show the respective carrier lifetimes for holes and the total lifetime given by Eq. (3.47) is given by the black curves.

Shallow quantum dot scattering lifetimes

Focusing on Fig. 3.10 which shows the charge carrier lifetimes of shallow QDs one observes that the lifetimes of electrons and holes of both the QD ground state and the QD excited

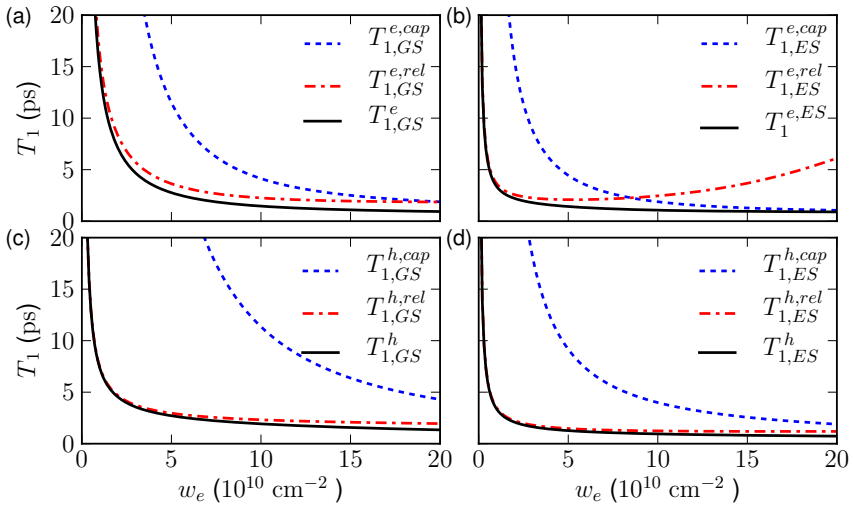

Figure 3.10: Shallow QD charge carrier lifetimes of the QD ground and first excited state levels in dependence of the QW electron density w_e for energy level spacings given in Table 3.1. The total lifetime is given by the black solid curve. The blue dashed curve and the red dash-dotted curve mark the lifetimes originating from only the capture and relaxation processes, respectively. (a): Electron lifetimes of the QD ground state. (b): Electron lifetimes of the QD first excited state. (c) and (d): Same as (a) and (b) for holes. The plasma temperature is $T = 300\,\mathrm{K}$ ($w_h/w_e = 1.0$). Other parameters as in Table 3.1.

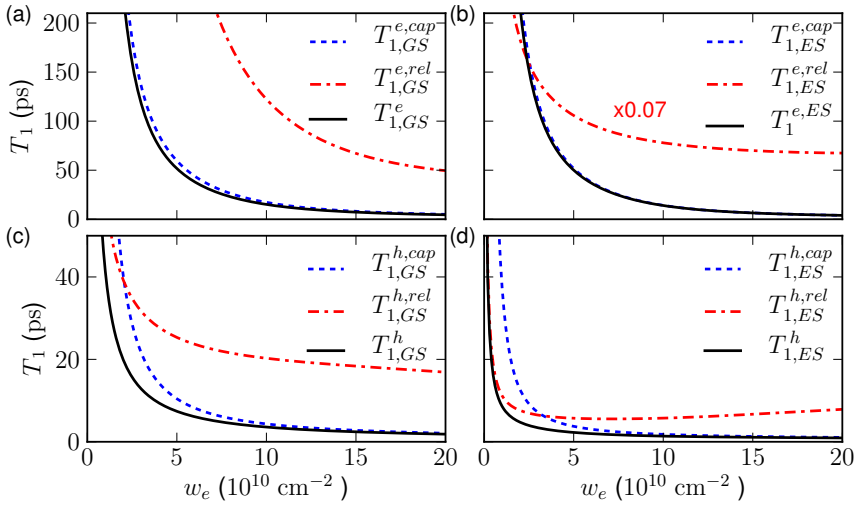

Figure 3.11: Deep QD charge carrier lifetimes of the QD ground and first excited state levels in dependence of the QW electron density w_e. Energy level spacings are according to Table 3.1.

state decrease monotonically with increasing QW electron density. At zero QW density the lifetimes diverge due to the vanishing scattering rates. The separate contributions for direct capture processes (blue dashed curves) and processes of relaxation type (red dash-dotted curves) from Eq. (3.47) shown in Fig. 3.10 indicate that the equilibrium carrier lifetimes of the QD levels of shallow QDs are to a large extent determined by the contribution from relaxation processes, especially in the low QW carrier density regime. The scattering lifetime attributed to direct capture processes is significantly larger than the contribution originating from relaxation type processes, especially for low QW electron densities. With increasing QW electron density the contribution from direct capture processes gains significance. In Fig. 3.10(b) the QD excited state electron lifetime is shown. Here, one can observe a crossover between the direct and relaxation type contribution to the overall scattering lifetime at $w_e \approx 8 \times 10^{11}\,\mathrm{cm}^{-2}$, from whereon the carrier capture process make the dominant contribution to the scattering lifetime of the QD excited state. The increase of the carrier lifetime associated with relaxation processes (red dash-dotted line) at high densities as visible in Fig. 3.10(b) can again be attributed to the effect of Pauli blocking, which reduces the scattering efficiency at high densities and thus increases the associated lifetime.

Deep quantum dot scattering lifetimes

The scattering lifetimes of the deep QD GS and ES levels are shown in Fig. 3.11. As a first observation the scattering lifetimes for deep QDs are significantly larger than those of shallow QDs (compare Fig. 3.10). For deep QDs, the carrier lifetimes originating from direct capture processes make the dominant contribution to the overall scattering lifetime for QW electron densities above $w_e \approx 5 \times 10^{11}\,\mathrm{cm}^{-2}$. This qualitative change in the behaviour can be attributed to the fact that a large energetic offset of the QD bound states to the QW band edge effectively reduces the out-scattering rate thus leading to an increased occupation probability of both the QD ground and excited states. This leads to effective Pauli blocking in the relaxation scattering channels and thus to a reduced scattering efficiency of the respective relaxation processes. This effect is most apparent in the case of electrons, since here the band offset to the QW band edge is very large (210 meV for the QD ground state).

3.5.4 Conclusion

The microscopic theory of Coulomb interactions in the considered QD-QW system allows one to calculate the density dependent energy renormalizations of the QW and QD single

particle states and the carrier-carrier scattering rates between the QW and QD energy levels. In the present approach the scattering contributions have been evaluated for the case of quasi-equilibrium between QW and QD. This approach is a good compromise between a full non-equilibrium approach and the simple ansatz of constant carrier lifetimes, since it is more exact than any approach using constant lifetimes while it is numerically by far not as demanding than a non-equilibrium approach. The use of non-constant carrier lifetimes in device simulations enhances the predictive power of the theoretical models and can account for effects such as carrier heating.

Chapter 4

Dynamic gain nonlinearities

The optical properties of semiconductor QDs have been the subject of ongoing research over the past decades. Especially the InGaAs/GaAs QD based devices have been widely investigated due to their application in optical communication systems in the $1.3-1.5\,\mu m$ wavelength window. InGaAs based QD amplifiers with high saturation power, broad gain bandwidth and ultrafast response have been reported. An understanding of the ultrafast gain dynamics driven by the underlying carrier and dipole dynamics is crucial in order to tailor high-speed optical devices. In the first part of this chapter the gain response to ultrashort input pulses [WEG10, MAJ10] is investigated with focus on the coupled carrier and dipole dynamics and the underlying carrier-carrier scattering mechanisms between the QD levels and the surrounding QW that have been derived in Chapter 3. The second part of this chapter deals with the static gain properties and the linewidth enhancement factor of QD SOAs.

The material equations used in this chapter are the combined Bloch equations for the QD and QW, Eqs. (2.48)- (2.50) and Eqs. (2.56) and (2.58), reformulated without first order Coulomb effects, which are neglected:

$$\frac{\partial p_m^j}{\partial t} = -i(\omega_m^j - \omega) - i\frac{\mu_m^j}{2\hbar}E\left(f_{e,m}^j + f_{h,m}^j - 1\right) - \frac{1}{T_2}p_m^j, \tag{4.1}$$

$$\frac{\partial f_{b,m}^j}{\partial t} = -\frac{\mu_m^j}{\hbar}\,\mathrm{Im}\left[E\,p_m^{j\,*}\right] - R_{sp,m}^j + \left.\frac{\partial f_{b,m}^j}{\partial t}\right|_{col}, \tag{4.2}$$

$$\frac{\partial p_k}{\partial t} = -i(\omega_k - \omega)p_k - i\frac{\mu^k}{2\hbar}E\left(f_e^k + f_h^k - 1\right) - \frac{1}{T_2^{QW}}p_k, \tag{4.3}$$

$$\frac{\partial f_b^k}{\partial t} = \Delta_b^k - \frac{\mu^k}{\hbar}\,\mathrm{Im}\left[E\,p_k{}^*\right] - \frac{1}{T_1^{QW}}\left(f_b^k - f_b^{k,eq}\right). \tag{4.4}$$

The term Δ_b^k explained in detail in Sec. 2.3.2 contains the current injection, spontaneous emission and scattering contributions to the dynamics of the occupation probability f_b^k of the QW states. These contributions are considered to be dependent on the global charge carrier density $w_b = (2/A)\sum_k f_b^k$ rather than on f_b^k. The carrier-carrier scatter-

Table 4.1: Numerical parameters and transparency current density used for the QD SOA simulation unless stated otherwise.

symbol	quantity	value
T_2	QD dephasing time	30 fs
T_2^{QW}	QW dephasing time	60 fs
T_1^{QW}	QW carrier lifetime	120 fs
μ_m^j	QD dipole moment	$0.6\,\mathrm{e_0\,nm}$
μ^k	QW dipole moment	$0.5\,\mathrm{e_0\,nm}$
Θ	pulse area	1.18π
$\hbar\delta\omega$	inhom. broadening	20 meV
N^{QD}	2D QD density	$10^{11} cm^{-2}$
j_0	transparency current density	$3.72 \times 10^{-9}\,\mathrm{e_0\,nm^{-2}fs^{-1}}$

ing contributions are included in the general expression $(\partial/\partial t) f_{b,m}^j|_{col}$ which have been derived in Chap 3. The macroscopic dipole density response of the medium is then given by Eqs. (2.52) and (2.69) as

$$P = P^{QD} + P^{QW} = \frac{2N^{QD}}{h^{QW}} \sum_{j,m} \mu_m^j f(\omega_j)\, p_m^j + \frac{2}{h^{QW} A} \sum_k p_k. \tag{4.5}$$

The parameters used throughout this chapter are listed in Table 4.1 unless stated otherwise. For an electric input pulse with amplitude $E(t)$ the pulse area θ is defined as the time integral over the Rabi frequency $\Omega(t)$

$$\theta = \int \Omega(t)\ \mathrm{dt} = \frac{\mu}{\hbar} \int E(t)\,\mathrm{dt}\,. \tag{4.6}$$

This gives a dimensionless quantity θ related to the optical input power in the case of a positive-valued pulse shape such as a Gaussian pulse. Without losses a pulse with $\theta = 2\pi$ in resonance to a two-level system leads to a complete *Rabi cycle* of the associated microscopic polarization $p(t)$.

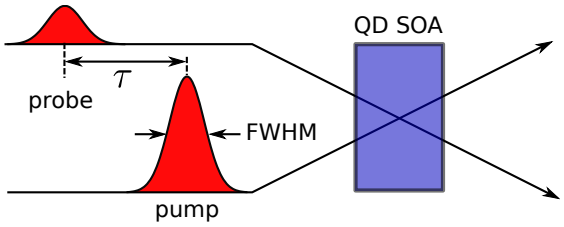

Figure 4.1: Schematic diagram of a pump-probe setup.

4.1 Pump-probe experiments

When an optical signal passes through the amplifier device, which is pumped above transparency, charge carriers recombine by means of stimulated emission. This reduces the gain for subsequent optical signals entering the amplifier. Carrier scattering processes between the QW and QD states then refill the charge carrier states in the QDs and thus increase the gain to its initial value. The gain recovery time, i.e., the time it takes to fully recover the gain after a signal has passed through the amplifier essentially determines the device performance. This section is dedicated to the analysis of the gain recovery dynamics of QD semiconductor optical amplifiers. The gain recovery dynamics can be determined experimentally in a pump-probe setup schematically shown in Fig. 4.1. In such a setup a strong pump pulse is used to excite the system and a delayed weaker probe pulse is then used to probe the gain state of the device at the delayed time τ.

The gain recovery dynamics is directly linked to the dipole and carrier dynamics and one can retrieve information on the polarization and carrier lifetime of the system. The different timescales of the involved processes allows to split the recovery dynamics into different characteristic stages: an ultrafast, a fast, and a slow recovery stage. The timescales of the coherent processes, which are on the order of tens to hundreds of fs determine the ultrafast recovery stage. For pump-probe delays large compared to the polarization lifetime T_2 the dynamic polarization is sufficiently decayed and the gain recovery dynamics is purely determined by the charge carrier dynamics of the QD-QW system. The fast recovery stage is characterized by the fast carrier-carrier scattering (ps timescale) mechanisms between QW and QD states, whereas the slow recovery phase is determined by the refilling of the QW states by current injection (ns timescales).

The following analysis focuses on single-color pump-probe setups, where the pump and probe signals are both centered around the same central frequency ω resonant to the central QD ground state transition frequency. The input signals are ultrashort Gaussian input pulses with a full width at half maximum (FWHM) of $FWHM = 150\,\mathrm{fs}$ in ac-

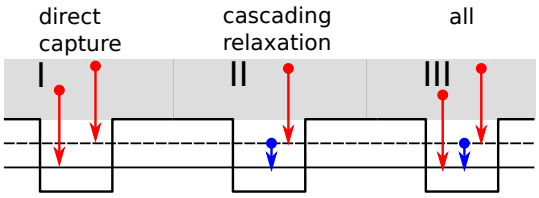

Figure 4.2: Illustration of the implemented scattering scenarios for electrons I: direct capture, II: cascading relaxation III: all scattering channels (direct capture and cascading relaxation). Auger electrons are omitted.

cordance with experimental setups [GOM08, GOM09]. In experiments the probe signal gain can be extracted using *heterodyne* detection setups. For a probe signal that is much weaker in intensity than the pump signal the probe signal will in good approximation induce a linear polarization response in the medium in addition to the nonlinear response induced by the strong pump signal. With this assumption the optical susceptibility is only dependent on the pump electric field and one can approximate the probe polarization as $P_{\text{probe}}(\omega) \approx P_{\text{pump+probe}}(\omega) - P_{\text{pump}}(\omega)$, where $P_{\text{pump+probe}}(\omega)$ is the Fourier amplitude of the macroscopic polarization induced by the superimposed pump and probe electric fields, and $P_{\text{pump}}(\omega)$ is the Fourier amplitude of the macroscopic polarization induced by the pump pulse alone. The probe susceptibility is therefore in good approximation given by

$$\chi_{\text{probe}}(\omega,\tau) = \frac{P_{\text{probe}}(\omega,\tau)}{\epsilon_0 E_{\text{probe}}(\omega,\tau)} \approx \frac{P_{\text{pump+probe}}(\omega,\tau) - P_{\text{pump}}(\omega)}{\epsilon_0 E_{\text{probe}}(\omega)}. \tag{4.7}$$

The differential gain $g(\omega,\tau)$ of the probe signal from Eq. (4.10) of the probe signal is then given by

$$g(\omega,\tau) = -\frac{1}{2}\Gamma\frac{\omega}{c\,n_{bg}}\,\text{Im}\left[\chi_{\text{probe}}\right] \approx -\frac{1}{2}\Gamma\frac{\omega}{c\,n_{bg}}\,\text{Im}\left[\frac{P_{\text{pump+probe}}(\omega,\tau) - P_{\text{pump}}(\omega)}{\epsilon_0 E_{\text{probe}}(\omega)}\right]. \tag{4.8}$$

Here, $E_{\text{probe}}(\omega)$ is the Fourier amplitude of the full complex electric field $E_{\text{probe}}(t)$ of the input probe pulse, Γ is the optical confinement factor, c is the vacuum velocity of light and n_{bg} is the background refractive index of the medium.

4.1.1 Impact of different scattering channels

In order to analyze the impact of each scattering channel on the gain recovery dynamics simulations with different scattering scenarios shown in Fig. 4.2 are preformed. The

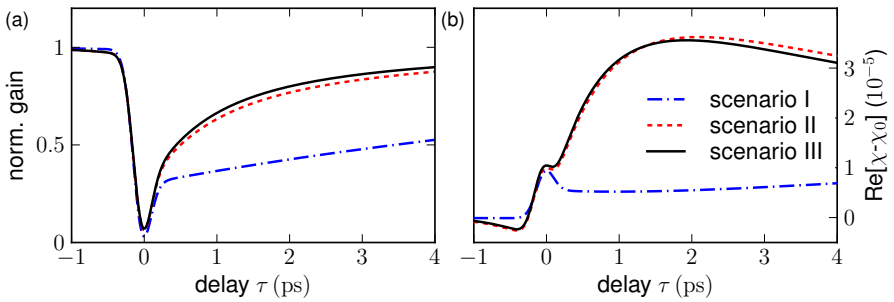

Figure 4.3: Simulated gain and phase recovery dynamics for the shallow QD configuration from Table 3.1 for a single injected pump pulse with pulse area $\theta = \pi$ for an injection current of $j = 10\, j_0$. Black solid curves shows the case with all Auger scattering processes, red (dashed) curves show the dynamics with direct capture processes only and blue (dash-dotted) curves with the cascading relaxation channel only. (a): Gain recovery dynamics and (b): Phase recovery dynamics in dependence of the pump-probe delay time τ. Parameters as in Table 4.1.

first scenario (I) consists of direct carrier capture processes from the QW to the QD ground and first excited state, the second scenario (II) is a cascading relaxation type scenario involving carrier capture from the QW to the first excited state of the QD and a subsequent relaxation from the ES to the GS and the third scenario (III) includes all possible scattering channels present in the system.

Shallow quantum dots

The gain and phase recovery dynamics a gain medium with shallow QDs embedded in a surrounding QW is shown in Fig. 4.3 in dependence of the pump-probe delay time τ for a current injection of $j = 10\, j_0$, with the transparency current j_0 from Table 4.1. The optical parameters are listed in Table 4.1. To quantify the impact of the different scattering channels Fig. 4.3 shows simulated gain and phase recovery dynamics for the direct scattering channel (scenario I from Fig. 4.2) given by the blue dash-dotted curve, the cascading scattering channel (scenario II from Fig. 4.2) shown as a red dashed curve and with all scattering channels (scenario III from Fig. 4.2) (black solid curve) as given by the microscopic calculations from Sec. 3.4. The normalized gain recovery dynamics in dependence of the pump-probe delay time τ is shown in Fig. 4.3(a). In the ultrafast recovery stage the deviations for different scattering scenarios are small, whereas in the fast recovery stage ($\tau > T_2$) the different scattering scenarios lead to significantly different dynamical behaviour. It becomes apparent that the cascading relaxation channel given by the red dashed line in Fig. 4.3(a) drives the (ultra-) fast recovery dynamics. The

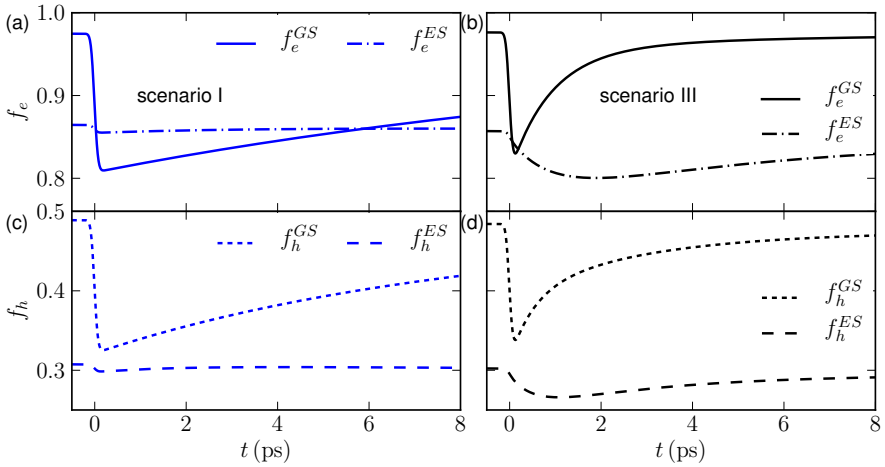

Figure 4.4: QD electron and hole dynamics for a single injected pump pulse with pulse area $\theta = \pi$ for an injection current of $j = 10\, j_0$ and pump-probe delay $\tau = 0$ for the shallow QDs according to Table 3.1. (a) Electron dynamics of the QD GS (blue solid curve) and ES (blue dash dotted curves) for scenario I from Fig. 4.2. (b) Same as (a) shown in black for scenario III of Fig, 4.2. (c) Hole dynamics of the QD GS (blue short dashed) and ES (blue long dashed) for scenario I from Fig. 4.2. (d) Same as (c) shown in black for scenario III of Fig, 4.2. Shallow QDs according to table 3.1. Other parameters as in Table 4.1.

additional enhancement due to direct capture process (difference between black solid and red dashed curve in Fig. 4.3(a)) is small. On the other hand the gain recovery dynamics only with direct capture processes given by the blue dash-dotted line in Fig. 4.3(a) results in a slow gain recovery dynamics.

In Figure 4.3(b) the associated phase recovery dynamics in dependence of the pump-probe delay time τ is shown. The phase change is given in terms of the real part of the probe susceptibility $\chi_{probe}(\omega, \tau)$ from Eq. (4.7) as $\mathrm{Re}[\chi_{\omega,\tau} - \chi_0]$, where χ_0 is the probe susceptibility of the unperturbed system (its value before the arrival of the pump pulse). The phase recovery dynamics is also characterized by an ultrafast dynamical regime in the vicinity of zero delay time τ followed by a fast and slow recovery stage for increasing delay times. The phase response of the full system with all scattering scenarios given by the black solid curve is again to a large extent determined by the cascading relaxation channel. Figure 4.4 shows the underlying carrier population dynamics of the QD electrons and holes resulting from the pump-pulse excitation used in Fig. 4.3. The population for scenario I of Fig. 4.2 with pump-probe delay $\tau = 0$ is shown in Figs. 4.4(a),(c), respectively, while Figs 4.4(b),(d) depict the electron and hole dynamics for scenario III.

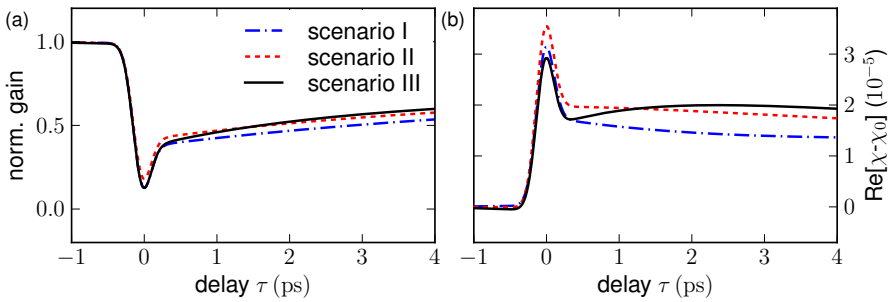

Figure 4.5: Same as Fig. 4.3 for deep QDs according to Table 3.1.

In Figs. 4.4(a),(c), the coherent interaction of the QD ground state with the incoming light field causes a strong carrier depletion both of electrons and holes, whereas the off-resonant ES experiences only little light-matter interaction (and the relaxation path to the GS is blocked). In Figs. 4.4(b),(d) relaxation processes between the ES and GS are allowed, which results in a strong decrease of the ES carrier populations and a faster refilling of the GS compared to scenario I.

Deep quantum dots

For deep QDs the gain and phase recovery dynamics is shown in Fig. 4.5(a) and (b). The gain recovery dynamics with deep QDs shown in Fig. 4.5(a) is qualitatively different from the that of shallow QDs shown in Fig 4.3(a). Here, the transition from the ultrafast to the fast recovery stage shows a distinct kink after which the gain recovery rate is significantly lower than in the case of shallow QDs. This behaviour can be directly linked to the lower scattering efficiency between the QW and QD states of the deep QDs (compare Figs. 3.8 and 3.4 and Figs. 3.9 and 3.5). Furthermore, the impact of the relaxation channel is not as significant as in the case of shallow QDs, where the relaxation channel drives the (ultra)-fast gain recovery. The deep QDs instead show quantitatively very similar dynamics for direct capture processes only (scenario I from Fig. 4.2) and cascading relaxation (scenario II from Fig. 4.2). The impact of the direct capture channels and the relaxation channels to the gain recovery dynamics is therefore comparable in magnitude for deep QDs.

The phase recovery dynamics for deep QDs is shown in Fig. 4.5(b). It also shows qualitative difference in comparison to the shallow dot case shown in Fig. 4.3(b). Again, the impact of the cascading relaxation is not as significant as in the case of shallow QDs. Furthermore, the maximum phase change occurs in the vicinity of zero delay time τ unlike in the case of shallow QDs, where the maximum phase change is observable at a delay time of several picoseconds. This may be attributed to the weak changes in the

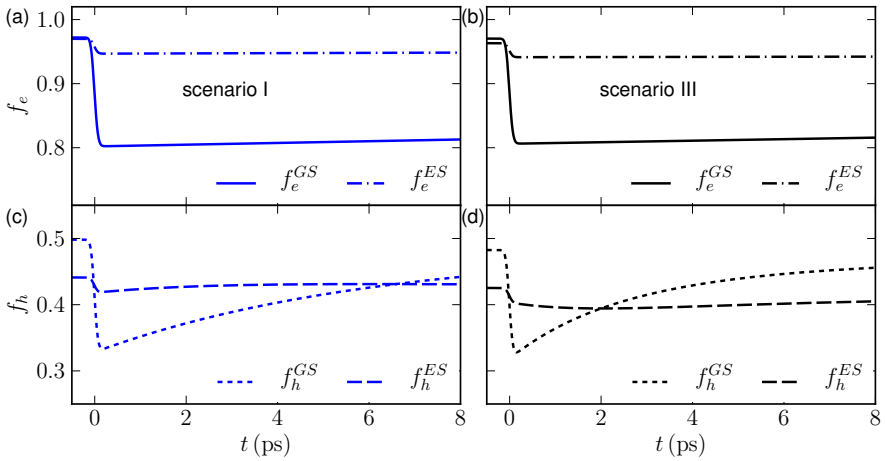

Figure 4.6: Same as Fig. 4.4 for deep QDs according to Table 3.1

QD ES electron and hole densities as shown in Fig. 4.6 for deep QDs.

The underlying carrier dynamics for the case of zero pump-probe delay τ is shown in Fig. 4.6. Here, Figs. 4.6(a) and (c) show the electron and hole dynamics of the QD ground and first excited staty for the case of direct carrier capture only (scenario I from Fig. 4.2), while Figs. 4.6(b) and (d) show the the electron and hole dynamics of the QD ground and first excited staty with all scattering channels included (scenario III from Fig. 4.2). Comparing Fig. 4.6(a) and (b) one observes that the QD electron ES remains nearly unaffected by the external input pulse in both cases. The same applies to holes as shown in Figs. 4.6(c) and (d). The overall impact of the cascading relaxation channel can therefore be regarded as small.

Impact of coherent quantum well interaction

Figure 4.7 shows the impact of the coherent QW interaction on the gain and phase recovery dynamics. Although the QW states are off-resonant to the central input light field frequency the coherent QW interactions makes a contribution to the total macroscopic polarization (as given by Eq. (2.69) resulting in slight deviations of the gain recovery dynamics from the case without coherent QW interactions, which can be observed in Fig. 4.7(a). The differences are most apparent in the ultrafast (coherent) recovery regime, whereas for large pump-probe delays the gain recovery dynamics for the cases with and without coherent QW interactions coincide nearly perfectly.

The phase dynamics shown in Fig. 4.7(b) for the case with coherent QW interactions

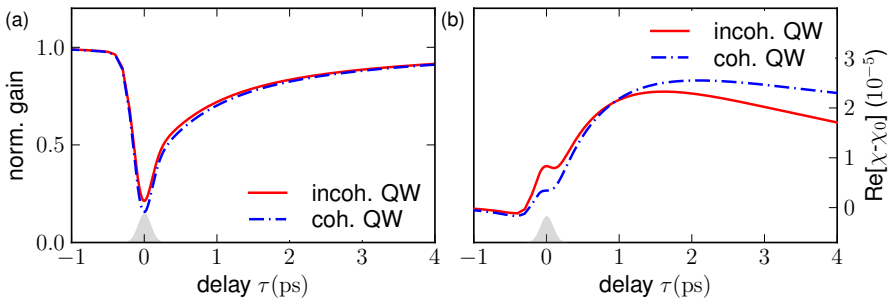

Figure 4.7: Gain and phase recovery dynamics for a single injected pump pulse with pulse area $\theta = \pi$ for an injection current of $j = 10\, j_0$ without (red solid curves) and with (blue dash-dotted) coherent interactions in the QW. All Auger scattering channels are included. (a): Gain recovery dynamics in dependence of the pump-probe delay time τ (b): Phase recovery dynamics in dependence of the pump-probe delay time τ. Other parameters as in Table 4.1.

shows quantitative differences compared to the case without coherent QW interactions both in the ultrafast regime and for large delay times. In the ultrafast recovery stage around $\tau = 0$ the real part of the susceptibility has a distinct kink caused by the rapid change of the charge carrier densities. The additional phase change originating from the coherent QW interaction counteracts the phase change induced by the QD states alone and flattens out the resulting kink in the phase dynamics around $\tau = 0$. For increasing delay τ the phase recovery dynamics is slower with coherent QW interaction compared to the case without coherent QW interaction.

4.1.2 Temperature effects

In this section carrier heating effects in QD SOAs are discussed and a comparison with measurements of the gain recovery dynamics is performed [MAJ11]. Injection of carriers into high energy states of the QW leads to an increase of the carrier plasma temperature and via carrier-phonon scattering processes also to an increase of the lattice temperature. Coupling to an external heat bath (the environment) counteracts carrier heating. The overall effect of plasma heating appears in the dependence of the device temperature on the electric pumping [GOM09] and in temperature dependent scattering rates. The temperature characteristic of the device along which the temperature varies in the dynamic simulation is modeled as linearly depending on the QW electron density in the range of interest. The functional dependence of the temperature is given by

$$T(w_e) = 145.645\,\mathrm{K} + 4.185 \cdot 10^{-9}\,\mathrm{K\,cm^2}\, w_e \quad \text{for } w_e \geq 4.57 \cdot 10^{10}\,\mathrm{cm^{-2}} \tag{4.9}$$

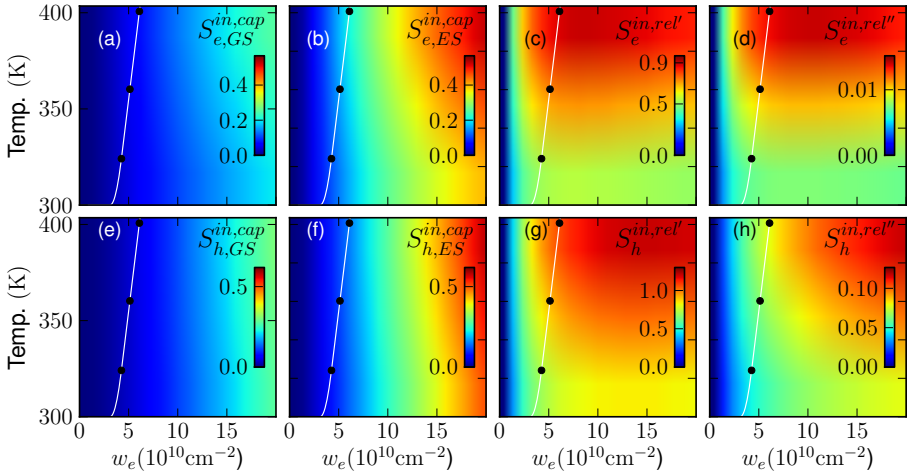

Figure 4.8: Density plots of the calculated Coulomb scattering rates in dependence of the QW electron density w_e and the plasma temperature T for fixed ratio $w_h/w_e = 1.5$. The assumed temperature characteristic of the device is shown by the white curves. Black dots mark the initial steady states used in the pump-probe simulations. [(a) and (b)]: Electron in-scattering rates for direct capture processes to the QD GS and ES, respectively. [(c) and (d)]: Electron relaxation rates for processes involving one intradot transition accompanied by a carrier transition within the QW or two QD-QW transitions, respectively. [(e) and (f)]: Hole in-scattering rates for direct capture processes to the QD GS and ES, respectively. [(g) and (h)]: Same as (c) and (d) for holes. The color code is in units of ps^{-1}. Parameters see Table 3.1.

For QW electron densities below a value of $4.57 \cdot 10^{10}\,\mathrm{cm}^{-2}$ a smooth transition to the lower temperature bound of 300 K (room temperature) is modeled. The temperature dependent scattering rates are shown in Fig. 4.8. The temperature characteristic is indicated by the white curves in Fig. 4.8 and the initial temperature values prior to the arrival of the input pulse for the different injection currents are marked by the black dots in Fig. 4.8. The assumed temperature characteristic is in good agreement with measurements performed in [GOM09], where the device temperature was extracted from a calibrated measurement of the displacement of the ripple modes in the SOA's cavity. Besides the considered Joule heating the device can also heat up due to Auger heating and free carrier absorption. In a scattering process between QW and QD as described in chapter 3.4 the assisting Auger electron or hole is lifted to an energetically higher level in the QW conduction or valence band causing a temperature increase in the equilibration process. Free carrier absorption accounts for intraband optical excitations within the conduction band induced by the external light field. Both of these effects are assumed to be small compared to Joule heating. The assumed energetic configuration is the shallow

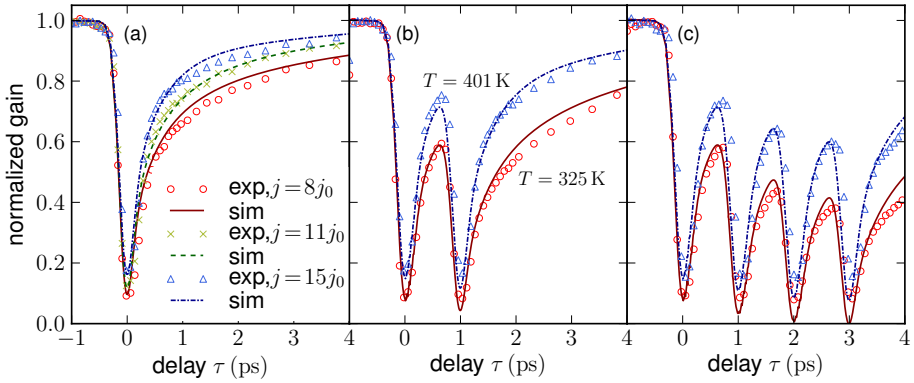

Figure 4.9: (a): Measured (exp) and simulated (sim) gain recovery dynamics for a single injected pump pulse and injection currents of $j = 8\, j_0$ (red 'o' symbols and solid curve), $j = 11\, j_0$ (green 'x' symbols and dashed line), $j = 15\, j_0$ (blue 'Δ' symbols and dash-dotted curve) (b): Gain recovery dynamics for two injected pump pulses with a spacing of $\Delta t = 1$ ps ($T = 325$ K and $T = 401$ K correspond to the initial temperatures). (c): Gain recovery dynamics for four injected pump pulses with a spacing of $\Delta t = 1$ ps.

QD configuration. The density- and temperature dependent scattering rates are shown in Fig. 4.8. Here, an increased scattering efficiency for higher plasma temperatures is visible for all in-scattering rates. Out-scattering is related to in-scattering via detailed balance [LUE09] and is not shown in the figure.

In experiments the gain recovery of a $InGaAs/GaAs$ quantum dot based semiconductor optical amplifier after the amplification of different short pulse trains (one, two and four pulses) has been measured. By incorporating carrier heating effects into the model an excellent agreement with ultrafast pump-probe measurements can be achieved [MAJ11]. Although attempts have been made to include carrier heating in QD semiconductor optical amplifier (SOA) models it remains a controversial issue. In Ref. [USK11] Auger heating in QD devices has been predicted to cause higher temperature increases than in QW or bulk devices along with a reduced scattering efficiency for elevated temperature and as a result a recovery performance loss. Despite the fact that the present work motivates the temperature increase by Joule heating as opposed to Auger heating, the microscopic theory of carrier-carrier scattering from chapter 3.4 predicts an enhanced scattering efficiency for elevated temperatures and as a direct consequence also a faster gain recovery dynamics, which stands in contrast to [USK11]. The measured gain recovery dynamics together with the simulated curves are shown in Fig. 4.9 for a single pulse pump-probe setup (a), a dual pulse setup (b) and a setup with four pump pulses (c). The pump-pulse spacing is chosen as $\Delta t = 1$ ps in accordance with the experiments

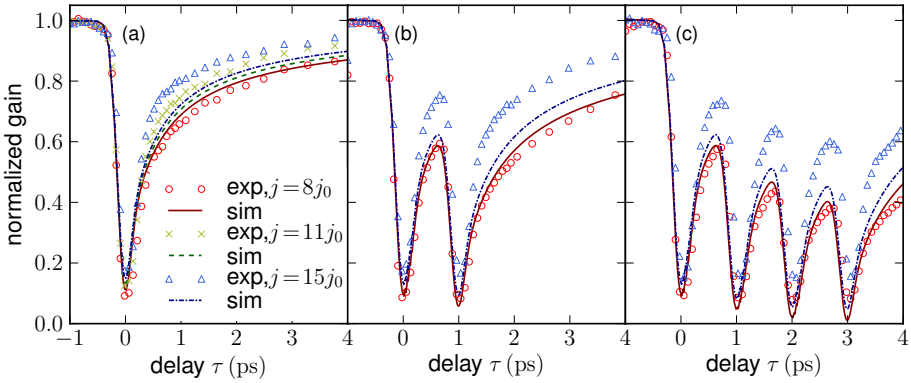

Figure 4.10: Same as Fig. 4.9 with a fixed temperature of $T = 300\,\mathrm{K}$ considered in the simulation.

and the arrival time of the first pump signal is at $\tau = 0$. The experimental data are shown for injection currents of 80 mA, 110 mA, and 150 mA, whereas the simulations are depicted for injection current densities $j = 8\,j_0$, $11\,j_0$, and $15\,j_0$ given in multiples of the transparency current density j_0, which corresponds approximately to a transparency current of 10 mA enabling a direct quantitative comparison. The simulated gain recovery dynamics in Fig. 4.9 is in excellent agreement with the measured data for all pump-probe setups (one, two and four pulses). Both in the ultrafast gain recovery stage ($\tau \approx T_2$), where the coherent dynamics of the polarization is essential and in the fast recovery stage, where τ is on the order of the carrier lifetime given by the Coulomb scattering between QW and QDs ($\tau \geq 1\,\mathrm{ps}$), the simulated curves match the measured data very well. The impact of the temperature dependence becomes apparent by comparing the experimental results to simulations without consideration of temperature effects in the model as is shown in Fig. 4.10. The increase in scattering efficiency due to the increase of the injection current alone cannot account for the experimentally observed increase of the gain recovery performance in the fast recovery regime. While the recovery dynamics for the lowest injection current still shows a very good agreement to the experimental data, the performance increase for higher injection currents of $j = 11\,j_0$ and $j = 15\,j_0$ remains too small and so the simulation results deviate very strong from the actual gain recovery behaviour of the QD SOA.

The carrier dynamics obtained from the simulation in the presence of the pump pulse only is shown in Fig. 4.11 for an injection current density of $j = 8\,j_0$. The input pulse is centered around $\tau = 0$. The QD ground and excited state populations are plotted for electrons and holes in Fig. 4.11(a) and (b), respectively. A clear signature of a strong

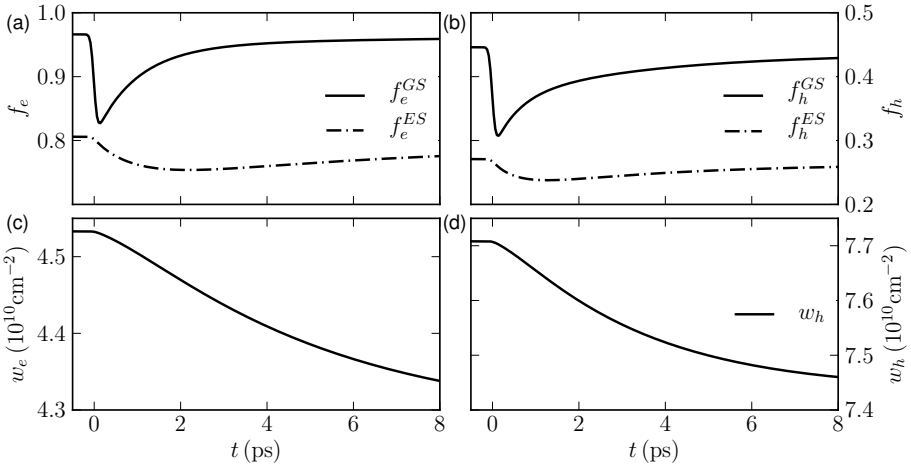

Figure 4.11: Time series of QW and QD charge carriers in the presence of the pump pulse only. (a): Calculated average electron populations in the QD ground state (black solid curve) and excited state (black dash-dotted curve) (b): Same as (a) for holes. (c): QW electron density. (d): QW hole density. The injection current density is $j = 8\,j_0$. Other parameters as in Table 4.1

cascading relaxation process is visible both for electrons and holes, where the QD ground state is quickly refilled by carriers from the excited state, which in turn shows a carrier depletion setting in with the arrival of the pulse, and is then slowly refilled from the QW.

The QW electron and hole dynamics shown in Fig. 4.11(c) and (d), respectively, is characterized by a continuous drain in the depicted time window of 8 ps.

4.1.3 Conclusion

In conclusion, the gain recovery dynamics of QD SOAs can be directly linked to the scattering efficiency of carrier-carrier scattering in the QD-QW system. It therefore sensitively depends upon the electronic structure of the QDs, but also on the the carrier plasma temperature. Deep QDs exhibit poor gain recovery performance in comparison to shallow QDs due to the lower scattering efficiency of carrier-carrier scattering. A comparison with experimental measurements of the gain recovery dynamics suggests that the QDs of the gain medium are shallow QDs. Furthermore the significant current density dependence of the gain recovery dynamics can only be reproduced by taking carrier heating effects into account. Band structure engineering and efficient temperature control are therefore highly interesting for the design of high speed optical devices.

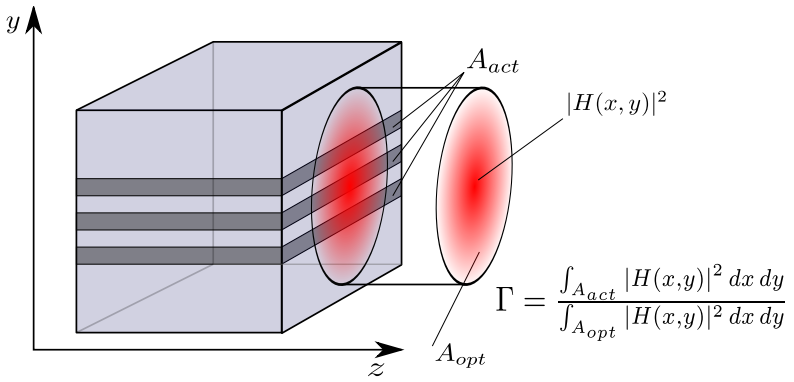

Figure 4.12: Illustration of the transverse optical confinement factor. $H(x, y)$ is the tranverse mode profile of the electric field.

4.2 Static gain properties

Quantum dot based optical amplifiers not only show ultrafast gain recovery dynamics due to the efficient QD-QW scattering mechanisms, they also have a broad gain spectrum associated with a large inhomogeneous broadening of the QDs. In the theoretical description the inhomogeneous broadening of the QDs is included by separating the QD ensemble into subgroups with unique transition frequencies as described in chapter 2. The width of the inhomogeneous broadening depends mainly on fluctuations in the material composition and size fluctuations of the QDs. In this section the static gain properties and the associated static linewidth enhancement factor are investigated.

The differential gain (per length) is defined as

$$g(\omega) = -\frac{1}{2}\Gamma\frac{\omega}{cn_{bg}}\,\mathrm{Im}[\chi(\omega)], \tag{4.10}$$

where Γ is the transverse optical confinement , c is the vacuum speed of light and $n_{bg} = \sqrt{\epsilon_b}$ is the background refractive index. The confinement factor is illustrated in Fig. 4.12 and defined in Eq. (B.22) (Γ is the confinement factor perpendicular to the propagation direction and not the in-plane confinement factor). It accounts for the fact, that only a fraction of the transverse mode (area A_{opt}) overlaps with the active cross section (area A_{act}). The optical parameters of the gain medium are chosen according to Table 4.1. The optical susceptibility $\chi(\omega)$ is obtained from the polarization response of the medium by calculating the steady state solution to Eqs. (4.1)-(4.4) for a single mode input electric field $E(t) = E_0\, e^{-i\omega\, t}$ with constant amplitude E_0. The resulting steady state macroscopic polarization density P from Eq. (4.5) can be used to calculate the susceptibility χ for

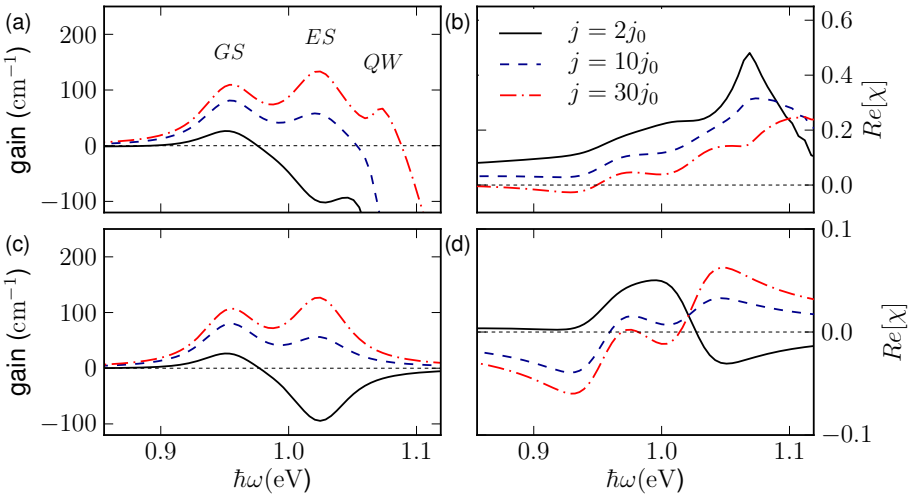

Figure 4.13: Shallow QD gain spectrum (a)and real part of the optical susceptibility Re[χ] (b) in dependence of the transition energy $\hbar\omega$ for injection currents of $j = 2\,j_0$ (black solid curve), $j = 10\,j_0$ (blue dashed curve) and $j = 30\,j_0$ (red dash-dotted curve) with coherent QW interactions included in the model. (c) and (d): same as (a) and (b) without coherent QW interactions (QW dipole moments $\mu^k = 0$). Parameters as in Table 4.1.

the given input frequency ω using the relation $P = \epsilon_0 \chi E$. In order to spectrally resolve the static gain the input frequencies ω have to be varied within the desired range.

4.2.1 Shallow quantum dot static gain spectra

The small signal linear gain and phase spectra for a gain medium comprised of shallow QDs are shown in Fig. 4.13(a) and (b) for current injection densities of $j = 2, 10, 30\,j_0$, respectively. As can be seen in Fig. 4.13(a) and (c) the QD ground state transition at $\hbar\omega = 0.96\,\text{eV}$ is above transparency for all values of the injection current densitie while the QD ES with transition energies around $\hbar\omega = 1.03\,\text{eV}$ is absorptive for $j = 2\,j_0$ and turns from absorption to gain at increased injection current densities. For high injection currents ($j = 30\,j_0$) the value of the ES peak gain even exceeds the GS peak gain in Fig. 4.13(a) and (b). Furthermore, for an injection current density of $j = 30\,j_0$ a third gain peak in the gain spectrum in Fig. 4.13(a) located at $\hbar\omega \approx 1.07\text{eV}$ appears, which can be attributed to the coherent QW interaction.

In Fig. 4.13(c) and (d) the gain and refractive index spectra are shown without coherent QW interaction (zero QW dipole moment $\mu^k = 0$). While the part of the gain spectrum covering transition energies up to values of the ES transition remains little

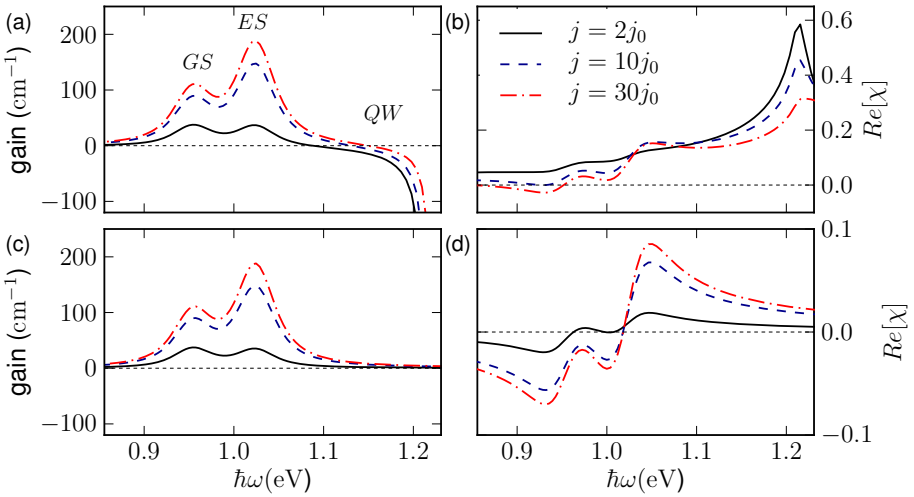

Figure 4.14: Same as Fig. 4.13 for deep QDs according to Table 3.1. Parameters as in Table 4.1.

affected by the coherent QW interaction the part of the gain spectrum with transition energies above the ES transition energy is significantly altered in the presence of coherent QW interaction. Without coherent QW interaction the gain curves approach zero gain for high transition frequencies, whereas with coherent QW interactions the gain medium is absorptive at high frequencies and may exhibit an additional gain peak at high injection current densities. The spectrum of the real part of the susceptibility is shown in Figs. 4.13(b) and (d) for the case of coherent ($\mu^k = 0.5$) and incoherent ($\mu^k = 0$) QW interaction, respectively. The real and imaginary part of the susceptibility are related via the *Kramers-Kronig* relations. Consequently, one also observes strong changes due to the coherent QW interaction in the spectrum of the real part of the susceptibility. Most importantly the changes in the spectrum of the real part of the optical susceptibility caused by the coherent QW interaction are significant at the QD ground state and first excited state transition energies.

4.2.2 Deep quantum dot gain spectra

Deep QD gain and phase spectra for different injection current densities of $j = 2, 10, 30\, j_0$ are shown in Fig. 4.14. As a main difference to the shallow QD gain spectra the excited state optical transition shows an enhanced gain compared to the shallow QD case. Here, the gain of the ES at a current injection density of $j = 30\, j_0$ is nearly double as high as the GS gain, whereas for shallow QDs the ES gain at $j = 30\, j_0$ merely exceeds the

GS gain. Furthermore, the gain of the QD ES optical transition exceeds the gain of the GS transition already for low injection currents of $j \approx 2\,j_0$, which was not the case for shallow dots (see Fig. 4.13). The increased ES gain can be attributed to the larger QD confinement energies of the deep QDs, which severely reduce the out-scattering rates of both the GS and the ES, and thus increase their steady state occupation probability.

4.2.3 Static α-factor

A parameter describing the coupling of gain and refractive index changes is the linewidth enhancement factor, or α-factor, first introduced in Ref. [HEN82]. The α-factor is defined as

$$\alpha(\omega) = \frac{\partial\,\mathrm{Re}[\chi(\omega)]/\partial N}{\partial\,\mathrm{Im}[\chi(\omega)]/\partial N}, \tag{4.11}$$

where χ is the optical susceptibility and N is the total electron density in the active region. In generic laser models the α-factor [HEN82, OSI87, AGR93a] is a commonly used parameter. It is known to affect the stability properties of QD lasers [OTT10] and is both experimentally and theoretically of high interest.

With the results from the previous section it is possible to calculate the frequency dependent α-factor of the gain medium in dependence of the injection current density as well as the excitation strength.

In the following the spectral properties and the associated α-factor will be investigated for the deep and shallow QD configurations from Table 3.1. The injection current density and the QD optical dephasing time as well as the amount of inhomogeneous broadening are varied.

Figure 4.15 shows the calculated small-signal α-factors obtained from the spectra shown in Fig. 4.13. Figure 4.15(a) shows the resulting α-factor at the QD GS transition in dependence of the injection current density. The black solid curve shows the α-factor for the full QD-QW system with coherent interaction of QD and QW states present. One can observe a strong injection current dependence of the α-factor showing a monotonic increase with increasing injection current density. In order to determine the impact of the QW states to the α-factor the blue dashed curve shows the value of α obtained without coherent QW interaction ($\mu^k = 0$). In that case the current density dependency of the α-factor is greatly reduced and unlike in the case with coherent QW interaction the α-factor increases up to an injection current density of $j \approx 5\,j_0$ and then decreases upon further increase of the injection current density. Also, the coherent contribution of the QW states to the α-factor becomes larger with increasing injection current density. While for small injection strengths the impact of the QW is rather insignificant, at high

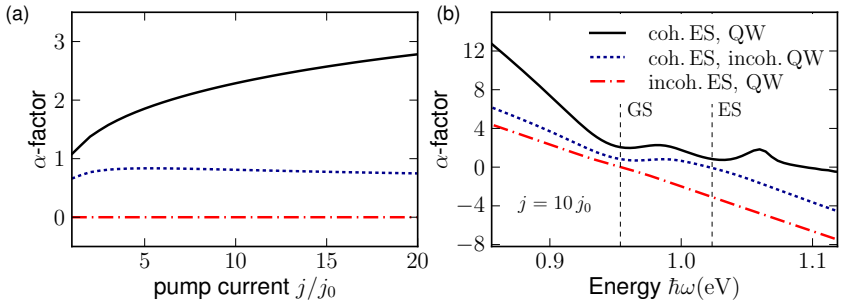

Figure 4.15: (a): α-factor at the QD GS frequency for shallow QDs from Table 3.1 in dependence of the injection current density calculated for a QD gain medium with coherent interaction in the GS only (red dash-dotted), GS and ES (blue dashed), and GS, ES and QW (black solid). (b): α-factor in dependence of the transition energy $\hbar\omega$ for an injection current of $j = 10\,j_0$. The vertical dashed lines mark the frequencies of the QD GS and ES optical transitions. Parameters as in Table 4.1.

injection strengths the QW states make up nearly half the contribution to the α-factor. Neglecting the coherent interaction of the QD ES state and the QW states by setting $\mu^{ES} = \mu^k = 0$ the resulting α-factor at the QD GS transition is zero, which is shown by the red dash-dotted line in Figure 4.15(a). This can be attributed to the symmetry of the gain spectrum in this case.

In Fig. 4.15(b) the frequency dependence of the α-factor is plotted for a fixed injection current density of $j = 10\,j_0$. The frequency dependence of the full QD-QW system is given by the black solid line in Fig. 4.15(b). It shows a nonlinear behavioutr and exhibits peaks at the frequencies corresponding to the local maxima/minima in the gain spectrum that can be attributed to the GS, ES, and QW transitions. In the vicinity of the optical QD GS and ES transitions marked by the vertical lines in Fig. 4.15(b) the α-factor has local minima. The blue dashed curve in Fig. 4.15(b) shows the α-factor that results by taking into account only the QD GS and ES coherent interaction and neglecting the QW dipole interactions ($\mu^k = 0$). In that case the α-factor is reduced over the whole frequency range compared to the case with coherent interaction of the QD states and the QW states. Neglecting the dipole interactions of the QD ES state as well as the QW states (setting $\mu^{ES} = \mu^k = 0$) results in a linear frequency dependence given by the red dash-dotted line in Fig. 4.15(b).

The injection current density and spectral dependence of the α-factor for deep QDs is shown in Fig 4.16. Regarding the current injection dependence one can observe a similar behaviour as in the case of shallow QDs, namely an increase of the α-factor with increasing injection strength. Overall, the α-factor remains smaller than in the shallow

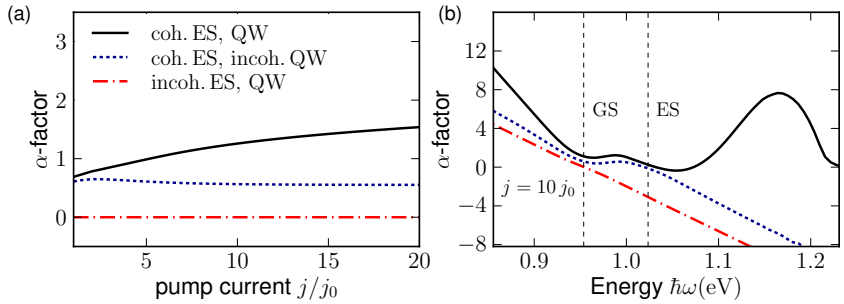

Figure 4.16: Same as Fig. 4.15 for deep QDs as given in Table 3.1. The vertical dashed lines mark the frequencies of the QD GS and ES optical transitions. Other parameters as in Table 4.1.

QD case and at low injection current densities the contribution of the QW states to the α-factor unlike for the case of deep QDs. The spectral dependence of the α-factor of deep QDs for a fixed injection current density of $j = 10\,j_0$ is shown in Fig. 4.16(b). Compared to the shallow QD α-factor one observes a pronounced peak in the frequency range covering the QW transitions, whereas in the spectral range of the QD GS and ES optical transitions the α-factor is similar to that of shallow QDs.

Here, the local minima in the spectral dependence of the α-factor do not coincide with the values of the QD GS and ES transitions. For the QD ES the deviations are especially pronounced and the local minima of the α-factor is shifted to higher frequencies than the optical transitions. This knowledge can be usefol to tailor optical devices with enhanced stability properties towards optical feedback or injection [OTT10].

Dephasing time and inhomogeneous broadening dependence

The optical dephasing time T_2 that is included in the model as a parameter (see Eq. (2.48)) generally depends on the QW carrier density and temperature just as the scattering rates. Microscopic calculations performed in [LOR06] based on a quantum kinetic approach suggest values of $5 - 8\,\text{meV}$ for the dephasing time. It is therefore useful to examine the dependence of the spectral properties and the α-factor on the QD dephasing time. The value of the inhomogeneous broadening $\hbar\delta\omega$ is another parameter in the model that might

Table 4.2: Homogeneous linewidth for different dephasing times T_2.

T_2	FWHM_{hom}
30 fs	21.9 meV
100 fs	6.6 meV

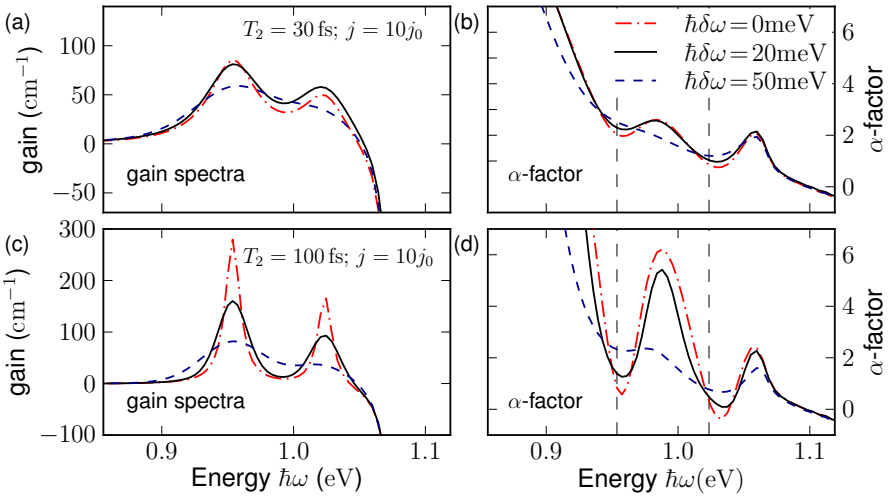

Figure 4.17: (a): Gain spectra in dependence of the transition energy $\hbar\omega$ for a fixed injection current of $j = 10\,j_0$ for a QD polarization dephasing time of $T_2 = 30\,\mathrm{fs}$ and different values of the inhomogeneous broadening $\hbar\delta\omega = 0, 20, 50\,\mathrm{meV}$. (b): α-factor in dependence of the optical excitation frequency ω for a fixed injection current of $j = 10\,j_0$ for a QD polarization dephasing time of $T_2 = 30\,\mathrm{fs}$ and different values of the inhomogeneous broadening $\hbar\delta\omega = 0, 20, 50\,\mathrm{meV}$. (c): Same as (a) with a QD polarization dephasing time of $T_2 = 100\,\mathrm{fs}$ (d): Same as (b) with a QD polarization dephasing time of $T_2 = 100\,\mathrm{fs}$. The vertical dashed lines mark the QD GS and ES optical transition frequencies. Shallow QDs according to Table 3.1. Other parameters as in Table 4.1.

vary from sample to sample or may even be tailored in specific growth modes. Therefore in this section the fundamental spectral properties for different values of the QD dephasing time T_2 and the amount of inhomogeneous broadening $\hbar\delta\omega$ are investigated for shallow and deep QDs.

Shallow quantum dot α-factor

In Figure 4.17 gain spectra and resulting α-factors for the QD-QW system are shown for two different QD optical dephasing times of $T_2 = 30\,\mathrm{fs}$ and $T_2 = 100\,\mathrm{fs}$ and in each case different values of the inhomogeneous broadening of $\hbar\delta\omega = 0, 20, 50\,\mathrm{meV}$. For the case of no inhomogeneous broadening given by the red dash-dotted line in Fig. 4.17 the linewidth of the spectra is determined solely by the homogeneous Lorentzian linewidth, which in turn is related to the dephasing time (see Eq. (2.44) and Table 4.1). For zero inhomogeneous broadening all QDs share the same transition frequency thus leading to a narrow gain spectrum. Comparing Figs. 4.17(a) and (c) one can observe that increasing the inhomogeneous broadening leads to a flattening and simultaneous broadening of the

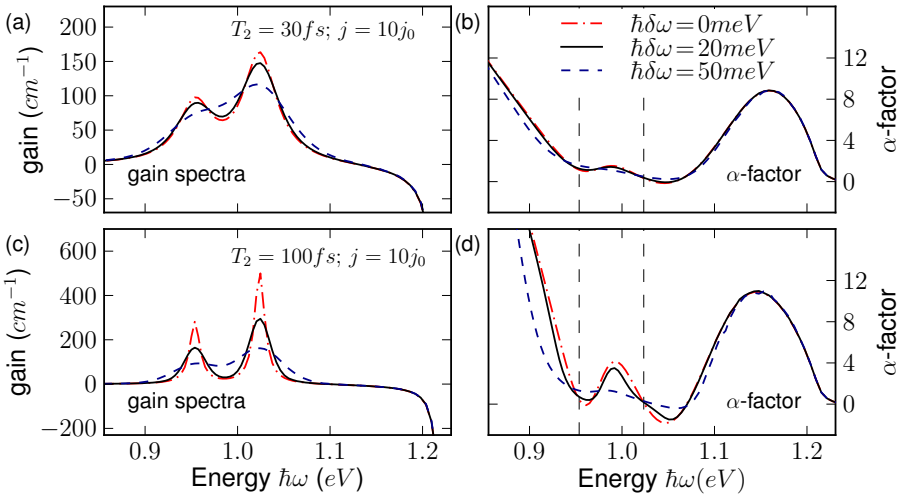

Figure 4.18: Same as Fig 4.17 for the deep dot energy level spacing as in Table 4.1. Other parameters as in Table 4.1.

spectra, while increasing the dephasing time T_2 has the opposite effect of narrowing the spectrum. Both effects are transferred to the frequency dependence of the α-factor in such a way that a larger QD dephasing time enhances the maxima and minima, while an increased broadening flattens the spectral dependence. For large dephasing times the variations in the spectral dependence of the α factor are considerable larger compared to the case of small dephasing times and the inhomogeneous broadening has a much greater impact on magnitude of the α-factor.

Furthermore, the α-factor exhibits local minima in its spectral dependence at transition energies close to, but not necessarily coinciding with, the QD GS and ES transitions. For a small value of the inhomogeneous broadening the local minima are most pronounced, thus a smaller inhomogeneous broadening seems to be beneficial for engineering devices with low α-factors.

Deep quantum dot α-factor

The influence of the QD dephasing time and the amount of inhomogeneous broadening of the QDs on the gain spectra and the α-factor for deep QDs (see Table 3.1) is shown in Fig. 4.18 for a fixed injection current density of $j = 10\, j_0$. One can observe the same parameter dependent behaviour as already seen in Fig. 4.17, namely that both an increase in the dephasing time as well as a reduction of the inhomogeneous broadening lead to narrower and enhanced gain peaks at the QD GS and ES optical transitions. At the

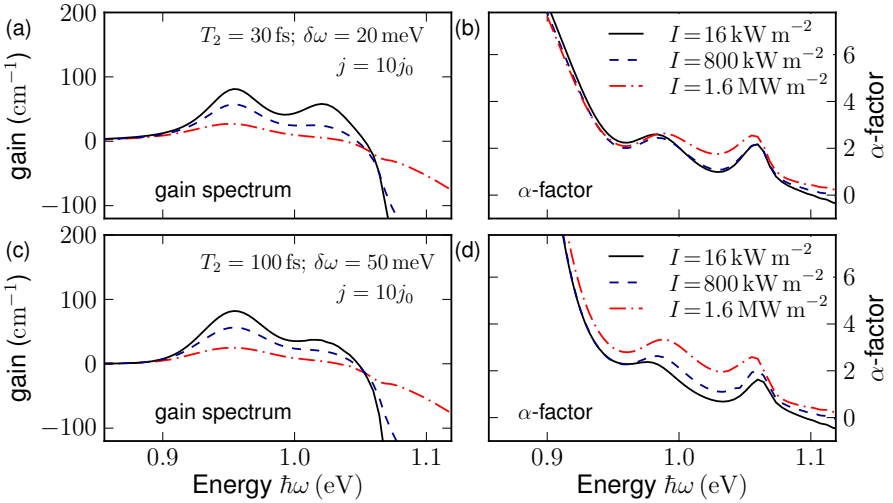

Figure 4.19: Shallow QD gain spectra and α-factors in dependence of the transition energy $\hbar\omega$ for different input irradiances of the electric field of I plotted as $I = 0.016\,\mathrm{MW\,m^{-2}}$ (dash-dotted) $I = 0.8\,\mathrm{MW\,m^{-2}}$ (solid) and $I = 1.6\,\mathrm{MW\,m^{-2}}$ (dashed) lines. (a): Excitation dependence of the gain spectrum and (b) the α-factor. The QD polarization dephasing has a value of $T_2 = 30\,\mathrm{fs}$ and an inhomogeneous broadening of $\hbar\delta\omega = 20\,\mathrm{meV}$. (c) and (d): Same as (a) and (b) with a QD polarization dephasing time of $T_2 = 100\,\mathrm{fs}$ and inhomogeneous broadening of $\hbar\delta\omega = 50\,\mathrm{meV}$. The injection current is set to $j = 10\,j_0$. Other parameters as in Table 4.1.

same time the frequency dependent modulation of the α-factor in the spectral window around the QD optical transition is enhanced. Additionally, one observes huge α-factors in the spectral range of the QW transitions, which stands in contrast to the shallow QD scenario (compare Fig. 4.17).

Excitation dependence

In the previous section the small signal spectral properties of the QD SOA were investigated. With increasing input irradiance of the electric field $E(t)$ the active medium starts to *bleach*, which refers to a reduction of the gain towards transparency. Figure 4.19 shows the gain spectra and the corresponding α-factors for different values of the input irradiance for a fixed injection current density of $j = 10\,j_0$ for deep and shallow QDs for different dephasing times and different values of the inhomogeneous broadening. Figs. 4.19(a) and (b) are calculated with a QD dephasing time $T_2 = 30\,\mathrm{fs}$ together with a broadening of $\hbar\delta\omega = 20\,\mathrm{meV}$, while Figs. 4.19(c) and (d) show spectra and α-factors for a dephasing time of $T_2 = 100\,\mathrm{fs}$ and $\hbar\delta\omega = 50\,\mathrm{meV}$. The gain bleaching for increasing optical

input irradiance is very well visible in Fig. 4.19(a) and (c). It leads to a reduction of the differential gain. With increasing input irradiance the resulting α-factor increases over a broad range of the frequency domain (only in the range of transition energies below the QD GS transition a decrease of the α-factor can be observed with increasing input irradiance as shown in Fig. 4.19(b)).

4.2.4 Conclusion

In conclusion, one observes that the shape of the gain spectrum strongly depends on the current injection density. The presence of the surrounding QW leads to strong absorptive behaviour at high frequencies and significantly alters the spectrum of the real part of the optical susceptibility in the frequency range of the QD optical transitions. The presence of QW dipole interactions leads to an increased α-factor of the QD-QW system. Furthermore, the α-factor exhibits a strong carrier density and frequency dependence. This suggests, that for a QD amplifier, where the amplified signals are not single mode and the carrier density may show time-dependent variations it is hard to determine a definite value for the α-factor. For single mode operation of a QD laser however one can very well define an α-factor for example at lasing threshold, where the carrier density is pinned to a fixed value.

Chapter 5

Pulse propagation dynamics

In optical networks it is desirable to have short pulses in time and in frequency domain. Nonlinearities of the gain medium may affect the input pulse leading to distortions from its original shape. The following analysis will focus on the aspects of pulse shaping and the analysis of chirp for ultrashort input pulses due to self-phase modulation.

5.1 Input-output characteristics

The input-output characteristics of an optical amplifier measures the output pulse energy (at the output facet) in dependence of the input pulse energy. It is an important device characeristic comparable to the $I-V$-characteristic of a semiconductor laser showing the gain saturation behaviour of the device.

In the limit of small input pulses the device is unsaturated. With increasing input pulse energy however, gain saturation effects become stronger leading to a gain suppression. The input-output characteristics of the investigated QD SOA is plotted in Fig. 5.1 in dependence of the input pulse area θ for unchirped Gaussian input pulses with a FWHM of 150 fs and 500 fs and a device length of $z = 500\,\mu$m. All curves are normalized to the small-signal single pass gain value at $\theta = 10^{-2}\pi$. As evident from Fig. 5.1 the amplification regimes can be separated into a small-signal regime, where the gain is unsaturated, followed by a transition regime and a gain saturation regime for high power input pulses, where the input signal is not significantly amplified any longer due to gain saturation. The optical parameters of the gain medium crucially affect the saturation behaviour. For the case of a large optical dephasing time of $T_2 = 100$ fs given by the red solid and blue dashed curves in Fig. 5.1 the transition from unsaturated to saturated behaviour is shifted towards smaller input pulse areas (e.g. smaller input pulse energies) compared to the case of a small dephasing time of $T_2 = 30$ fs. The reason for this behaviour is that a larger dephasing time enhances the induced polarization. Therefore saturation sets on for weaker input pulse signals (smaller input pulse areas).

In the next section the dynamic properties of the QD SOA will be discussed for

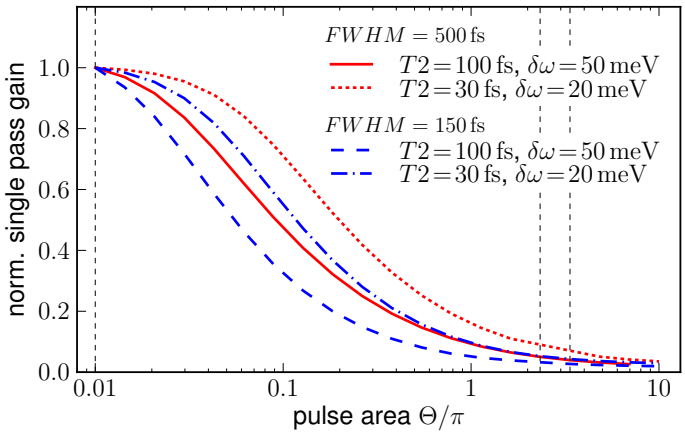

Figure 5.1: Normalized single pass gain of the QD SOA in dependence of the input pulse area θ. The red solid and short dashed curves are for an initial input pulse width of $FWHM = 500\,\text{fs}$ and optical parameter sets I and II from Table 5.1, respectively. The blue long dashed and dash-dotted curves are for an initial input pulse width of $FWHM = 150\,\text{fs}$ and optical parameter sets I and II from Table 5.1, respectively. Shallow QDs according to Table 3.1. Other parameters as in Table 4.1.

different input pulse areas of $\Theta = 10^{-3}\,\pi$ in the unsaturated domain and $\Theta = 2.33\,\pi$ and $\Theta = 3.36\,\pi$ in the saturated domain of the QD SOA indicated by the vertical dashed lines in Fig. 5.1.

5.2 Self-phase modulation

One important manifestation of the intensity dependence of the refractive index in nonlinear media occurs through self-phase modulation, a phenomenon that leads to spectral broadening of optical pulses. It describes the phase modulation of an optical pulse induced by the refractive index variations during its propagation. Another nonlinear gain effect is cross-phase modulation, which refers to the phase modulation of an optical field induced by a co-propagating field at different frequency. In this section the induced phase dynamics and the resulting chirp of optical signals due to self-phase modulation is

Table 5.1: Parameter sets used for the simulation of the propagation dynamics.

Set I	Set II
$T_2 = 100\,\text{fs}$ (6.6 meV)	$T_2 = 30\,\text{fs}$ (21.9 meV)
$\hbar\delta\omega = 50\,\text{meV}$	$\hbar\delta\omega = 20\,\text{meV}$

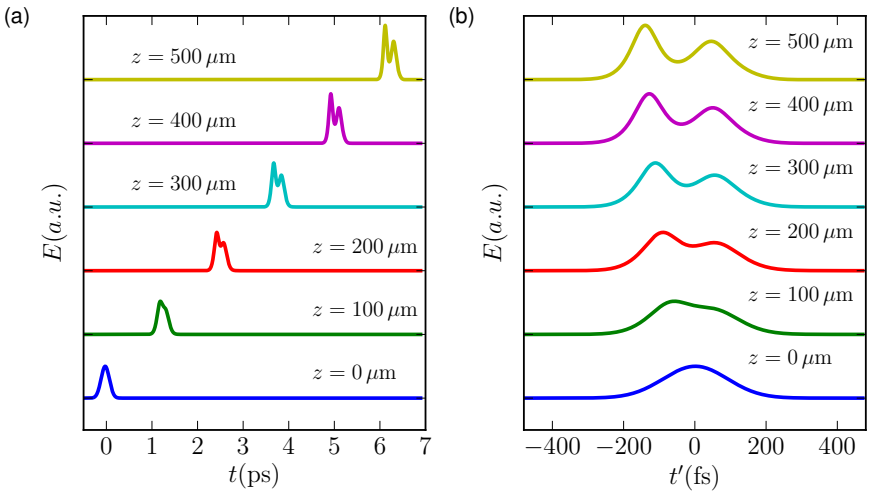

Figure 5.2: Time series of the electric field amplitude of a Gaussian input pulse with $FWHM = 150\,\text{fs}$. The optical parameter are chosen according to set I from Table 5.1 and a pulse area of $\Theta = 2.33\,\pi$. The injection current density is $j = 10\,j0$. (a) Time series $E(t)$ at different spatial positions z. (b) Time series $E(t')$ in the comoving frame. Offsets are for better visibility. Shallow QDs according to Table 3.1. Other parameters as in Table 4.1.

investigated. The chirp of an optical signal refers to the instantaneous frequency change of the pulse over time. The focus of the analysis is on coherent effects induced by the polarization dynamics and the impact of coherent interaction with the QW states. The initial slowly varying input signals are unchirped Gaussian input pulses of the form

$$E(z=0,t) = E_0 \exp\left[\frac{-t^2}{2\sigma^2}\right], \tag{5.1}$$

where E_0 is the amplitude of the input signal and σ is the standard deviation of the Gaussian signal (and the full width at half maximum is $FWHM = 2\sqrt{2\ln 2}\,\sigma$). It is convenient to express the slowly varying envelope of the electric field in terms of amplitude $|E|$ and phase ϕ as

$$E(z,t) = |E(z,t)|e^{i\phi(z,t)}. \tag{5.2}$$

The acquired chirp of the signal is then given by the second derivative of the phase $\ddot{\phi}(z,t)$. Table 5.1 lists the parameter sets already used in Sec 4.2 that will be considered for the analysis of the pulse propagation dynamics. In the following analysis of the spatiotemporal dynamics it is convenient to transform into a comoving frame by introducing new

space and time coordinates z' and t' as follows

$$t' = t - \frac{z}{v_g}, \quad z' = z. \tag{5.3}$$

Here, $v_g = c/n_{bg}$ is the group velocity, $n_{bg} = \sqrt{\epsilon_{bg}}$ is the background refractive index and ϵ_{bg} is the background permittivity. The application of the transformation to the spatiotemporal dynamics of the electric field is illustrated in Fig. 5.2. Here, panel (a) shows timeseries of the electric field at different spatial coordinates z in dependence of t, while panel (b) shows the electric field dynamics in dependence of t'. With the transformation into a comoving frame defined by Eq. (5.3) the time window needed to capture the relevant spatiotemporal dynamics of the signal is reduced compared to the untransformed coordinates. In the following all spatiotemporal plots are made in the comoving frame.

5.2.1 Small-signal regime

In the limit of small input pulse energies (amplitudes) the gain is in good approximation linear and saturation effects can be neglected. A pulse propagating in this regime will acquire only a linear phase shift and therefore no chirp. The resulting spatiotemporal propagation dynamics for an injection current density of $j = 10\, j_0$ and an input pulse with $\Theta = 0.01\pi$, and optical parameter set I is shown in Fig. 5.3(a). The shape of the pulse remains more or less unchanged. The phase dynamics at the output facet at $z = 500\mu$m and the acquired chirp of the pulse is shown in Fig. 5.3(b). The phase shows an initially linear dependence and the corresponding chirp is minimal around $t' = 0$. The case of a smaller dephasing time T_2 (parameter set II) is not shown, since the qualitative features are very similar in that case. Due to the very small input pulse area, the charge carrier densities change only very little upon propagation of the pulse through the device (see Fig. 5.3(c) and (d).)

5.2.2 High power regime

In the high power regime the gain medium shows strongly nonlinear behaviour. The spatiotemporal dynamics of a pulse in this domain with an input pulse area of $\theta = 2.33\,\pi$ is shown in Fig. 5.4 for optical parameters given by set I from Table 5.1. The pulse shape is strongly deformed from its initial Gaussian shape and in this special case the pulse exhibits a breakup and a second maximum appears while the pulse propagates through the amplifier medium. The breakup of the pulse is a manifestation of coherent Bloch

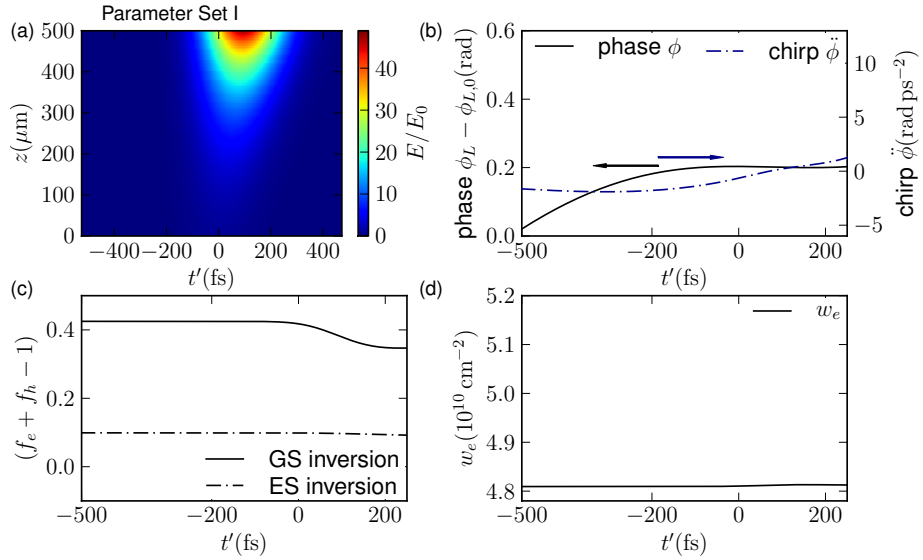

Figure 5.3: (a): Spatiotemporal dynamics of the slowly varying electric field amplitude E in dependence of time $t' = t - z/v_g$ and spatial coordinate z. The color code indicates the amplification in units of the initial slowly varying amplitude E_0 at the input facet ($z = 0$). (b): Temporal evolution of the phase change and chirp at the output facet ($z = 500\mu$m) given by the black solid and dash-dotted curves, respectively. The injection current density is $j = 10 j_0$, the input pulse area is $\Theta = 10^{-2}\,\pi$ and the optical parameters of the gain medium are $T_2 = 100\,$fs and $\hbar\delta\omega = 50\,$meV. Shallow QDs according to Table 3.1. Other parameters as in Table 4.1.

oscillations induced by the strong input pulse. Despite the damping of the polarization it leads to absorptive behaviour of the gain medium in the time window between the two pulse peaks. Without the separate degree of freedom given by the polarization dynamics, an input pulse could not induce a transition between absorption and gain, instead the gain would bleach in a monotonic way. Since the damping of the polarization is given by the inverse of the polarization lifetime one can expect this behaviour to strongly depend on the dephasing time T_2. In Fig. 5.5(a) the pulse propagation dynamics is shown for the case of $T_2 = 30\,$fs and $\hbar\delta\omega = 20\,$meV. While the strong gain nonlinearity leads to enhanced amplification of the leading pulse edge, the pulse breakup behaviour as in Fig. 5.4(a) can no longer be observed. The phase and chirp dynamics at the output facet is shown in Fig. 5.4(b) and 5.5(b) for the two cases discussed. The phase given by the black solid curves increases monotonically over the duration of the pulse and in the high intensity region of the pulse the phase shows nonlinear behaviour, an indication of gain nonlinearities. The resulting chirp shows a maximum in the high intensity region

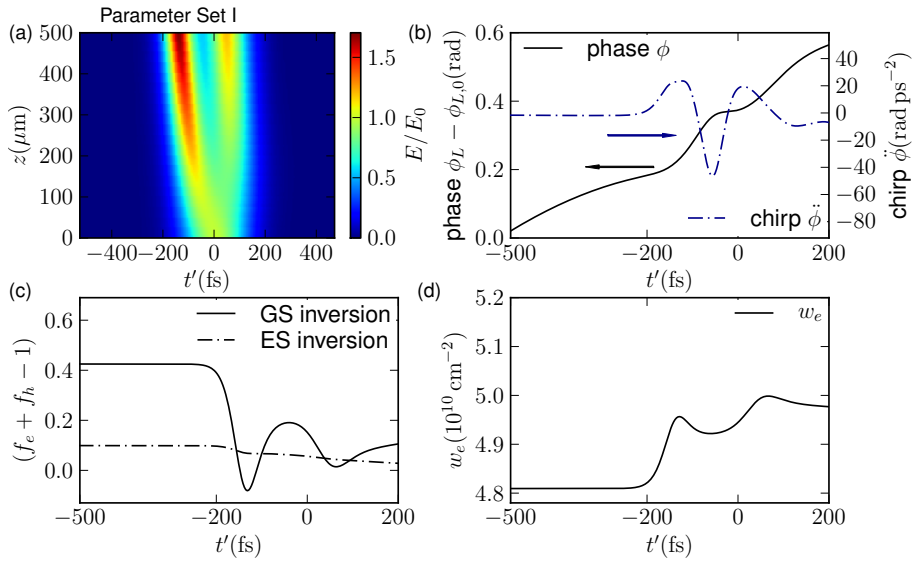

Figure 5.4: Same as Figure 5.3 but with input pulse area $\theta = 2.33\pi$. Parameters are $T_2 = 100\,\mathrm{fs}$ and $\hbar\delta\omega = 50\,\mathrm{meV}$ (Set I from Table 5.1). Other parameters as in Table 4.1.

of the pulse and the chirp dynamics follows the electric field intensity dynamics. In Fig. 5.4(c) the average QD GS and ES inversion at the output facet is plotted. The average GS inversion (black solid curve) shows an oscillatory behaviour with two minima corresponding to the intensity peaks of the pulse, while the QD ES state (dash-dotted curve) is on average less inverted than the GS prior to the arrival of the pulse. During and after the pulse duration the ES inversion then gradually decreases. The QW electron dynamics at the output facet is shown in Fig. 5.4(d). Here, an increase of the electron density due to the coherent light-matter interaction in the QW can be observed setting in with the arrival of the pulse.

Further increasing the input pulse area to $\Theta = 3.36\,\pi$, the spatiotemporal pulse propagation dynamics has the form shown in Fig. 5.6(a). The associated phase and chirp dynamics at the output facet is given in Fig. 5.6(b). As already observed in Fig. 5.4(a) the pulse envelope is broadened while propagating through the medium and again a pulse breakup can be observed, only here the first peak structure has a lower amplitude than the second peak. The phase and chirp dynamics shown in Fig. 5.6(b) is qualitatively similar to that observable in Fig. 5.4(b).

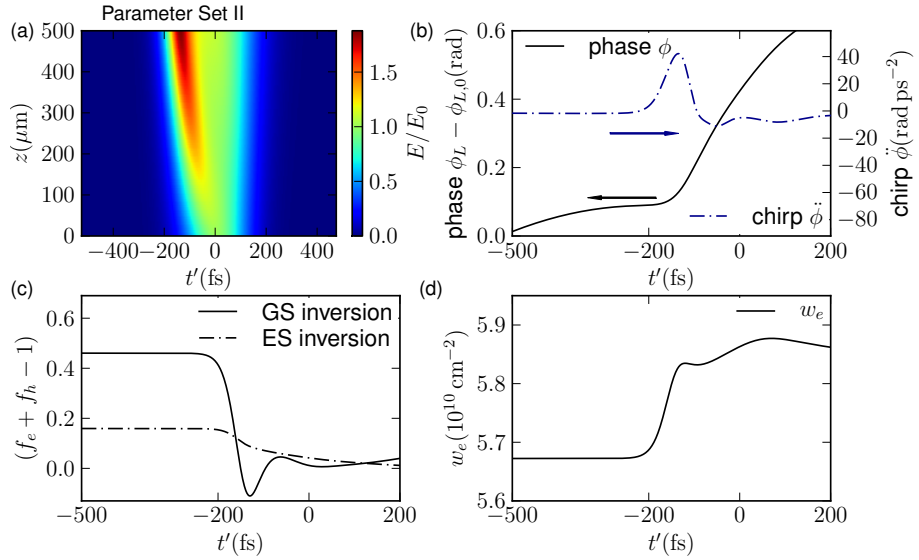

Figure 5.5: Same as Fig. 5.4 except $T_2 = 30\,\mathrm{fs}$ and $\hbar\delta\omega = 20\,\mathrm{meV}$ (Set II from Table 5.1). Other parameters as in Table 4.1.

5.3 Impact of coherent interaction in the QW

In Sec 4.2 it was found that the coherent interaction of light with the QW states has a significant impact on the spectral properties and on the α-factor of the device. The strong dependence of the α-factor on the coherent QW interaction suggests that the dipole interactions in the QW also affect the propagation dynamics of optical pulses. In order to analyze the impact of the coherent interaction of the QW on the propagation dynamics of ultrashort pulses in the QD SOA the full dynamics is compared to the limiting case without coherent QW interaction by setting the dipole moment of the QW states to zero, e.g., $\mu^k = 0$. The injection current density is in both cases set to $j = 10\,j_0$. The absolute value of the injected current is not the same in this case, since the transparency current density changes when the QW interactions are switched on or off. When including coherent QW interactions the transparency current density is shifted to higher values compared to the case of no coherent QW interactions. The QW states are not inverted when the QD GS cross from absorption to gain causing an additional absorptive contribution from the QW states to the overall gain that has to be overcome by the QD gain contributions, thus requiring a higher inversion of the QD states. This in turn requires a higher injection current density. The transparency current densities are listed in App. A.4. Figure 5.7 shows the dynamical behaviour at the

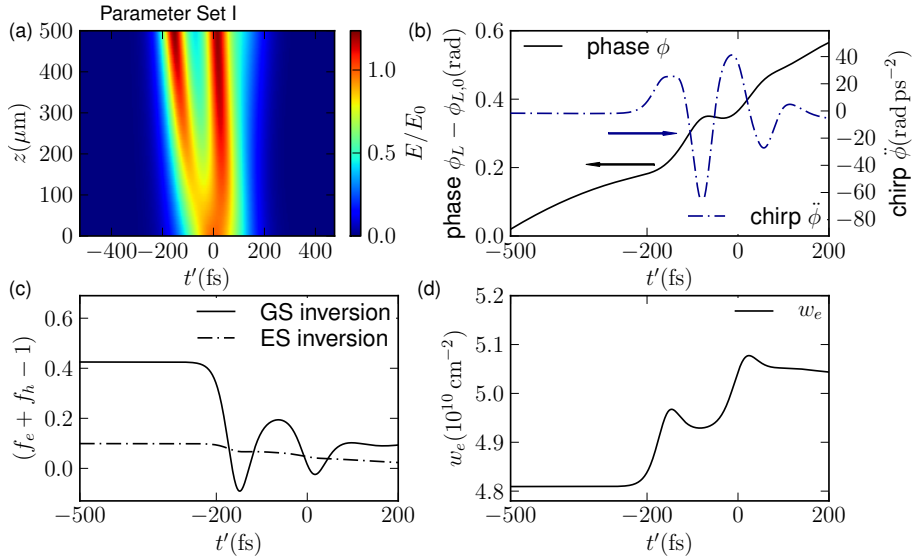

Figure 5.6: Same as Figure 5.3 for an input pulse area $\theta = 3.36\pi$. Parameters are $T_2 = 100\,\text{fs}$ and $\hbar\delta\omega = 50\,\text{meV}$ (Set I from Table 5.1). Other parameters as in Table 4.1.

amplifier output facet for the case of coherent QW interactions included in the dynamics ($\mu^k = 0.5$, black solid curves) and the case when coherent QW interactions are neglected (μ^k=0, blue dash-dotted curves). The input pulse width and area are $FWHM = 150\,\text{fs}$ and $\theta = 2.33\,\pi$, respectively, and the current injection is $j = 10\,j_0$. The amplitudes of the slowly varying electric field is shown in Fig. 5.7(a), while the chirp of the signal is plotted in Fig. 5.7(b) for the two cases. While the shape of the electric field envelopes are qualitatively and quantitatively very similar in both cases, the magnitude of the chirp the pulse acquires is underestimated when the coherent QW interactions are neglected. The QD GS inversion is shown in Fig. 5.7(c). The initial difference of the inversion for the two cases considered is a result of the different absolute values of the current injection density. The double-peak structure of the pulse envelope leads to two local minima of the GS carrier inversion. The QW electron density is shown in Fig. 5.7(d). The left and right scale are for the cases with and without coherent QW interaction, respectively. The higher injection current density in the case of coherent QW interactions leads to higher initial QW charge carrier densities than without coherent QW interaction. Although the QW states are off-resonant the coherent interaction generates carriers in the QW leading to a significant increase of the QW electron density with the onset of the pulse. With no coherente interaction in the QW the electron density gradually decreases due to incoherent scattering processes between the QD and QW states. Increasing the pulse

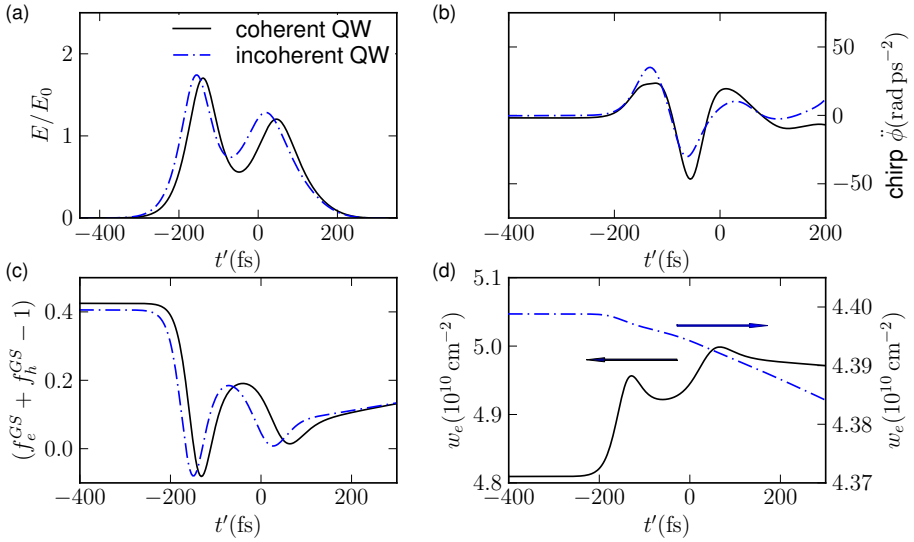

Figure 5.7: Comparison of the propagation dynamics with quantum well dipole moment $\mu^k = 0.5\,e_0 nm$ (black solid curve) and $\mu^k = 0$ (blue dash-dotted curve). The current injection strength in both cases is $j = 10\,j_0$ and the input pulse area and FWHM of the Gaussian input pulse are $\theta = 2.33\pi$ and $FWHM = 150\,\mathrm{fs}$. (a): Dynamics of the slowly varying electric field amplitude at the ouput facet $z = 500\,\mu\mathrm{m}$ in dependence of time t'. (b): Time evolution of the chirp at the output facet. (c): GS inversion at the output facet. (d): QW electron dynamics w_e at the output facet. The dephasing time is set to $T_2 = 100\,\mathrm{fs}$ and the inhomogeneous broadening to $\hbar\delta\omega = 50\,\mathrm{meV}$. Shallow QDs according to Table 3.1. Other parameters as in Table 4.1.

width to $FWHM = 500\,\mathrm{fs}$ while keeping the other parameters in Fig. 5.7 results in the dynamical scenario shown in Fig. 5.8. As before, the field envelopes show little deviations when switching the coherent QW interaction on or off. Comparing Figs. 5.8(b) to 5.7(b) one notices that the maximum chirp for 500 fs pulse is significantly reduced compared to the 150 fs pulse and the relative error made when neglecting the coherent QW interaction becomes smaller.

5.4 Band structure effects

To investigate the band structure effects, the pulse propagation dynamics investigated in Sec. 5.2 for shallow QDs with energy levels according to Table 3.1 is reconsidered in this section for deep QDs according to Table 3.1.

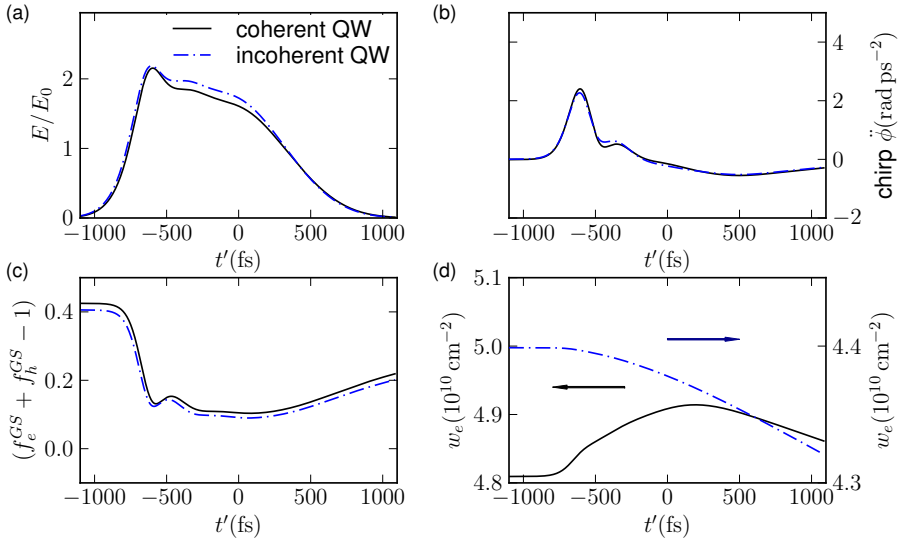

Figure 5.8: Same as Fig. 5.7 for an input pulse width of $FWHM = 500\,\mathrm{fs}$.

5.4.1 Small-signal regime

For a small-signal input signal with pulse area $\Theta = 10^{-2}\,\pi$ the corresponding spatiotemporal dynamics along with the phase and chirp dynamics of the electric field and the QD and QW carrier dynamics at the output facet is shown in Fig. 5.9. In comparison to the dynamics of the shallow dot configuration from Fig. 5.3 one observes a higher single pass gain (due to a larger differential gain, compare Figs. 4.13 and 4.14). The maximum pulse amplitude at the SOA output facet is approximately 80 times larger than the input signal. As a consequence one can observe gain saturation effects in the GS carrier inversion in Fig 5.9(c) due to the strong built-up electric field. The field intensity at the output facet is strong enough that coherent interactions with the off-resonant QW states takes place leading to an increase in the QW electron density shown in Fig. 5.9(d) (QW hole density is omitted). Furthermore, the emergence of gain nonlinearities gives rise to a non-constant chirp as can be seen in Fig. 5.9(b).

5.4.2 High power regime

In the saturated regime of the QD SOA the spatiotemporal pulse propagation dynamics for deep QDs is reevaluated as in Sec 5.2. The results for input pulse areas of $\theta = 2.33\,, 3.36\pi$ are shown in Figs. 5.10 and 5.11, respectively. For an input pulse area of $\Theta = 2.33\,\pi$ Figs. 5.10(a) and (b) the spatiotemporal dynamics of the slowly varying

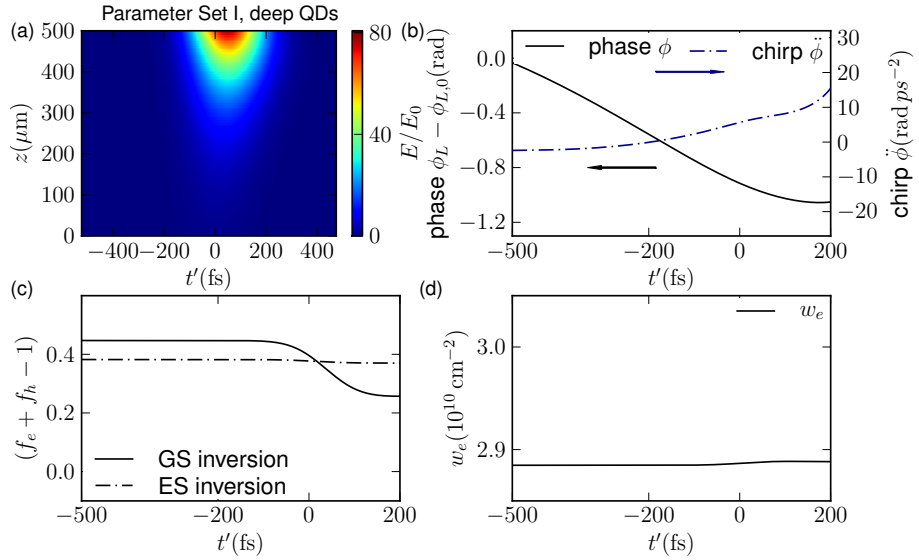

Figure 5.9: Same as Figure 5.3 for deep QDs from Table 3.1. Parameters are $\theta = 10^{-2}\pi$, $T_2 = 100\,\mathrm{fs}$, and $\hbar\delta\omega = 50\,\mathrm{meV}$ (Set I from Table 5.1). Other parameters as in Table 4.1.

electric field envelope and the output phase and chirp of the signal, respectively. The dynamics of the QD GS and ES carrier inversion and the QW electron density are plotted in Fig. 5.10(c) and (d), respectively. The electric field envelope in Fig. 5.10(a) shows even more pronounced pulse breakup than in 5.4(a). Compared to Fig. 5.4(b) the chirp for the deep QDs is larger than in the shallow dot case. The QD GS and ES inversion is shown in Fig. 5.10(c). Unlike in the case of shallow QDs the GS inversion only slightly exceeds the ES inversion here. The QD GS optical inversion shows strong coherent oscillations as in the shallow dot case while the ES experiences a carrier drain when the pulse interacts with the medium. The QW electron density (hole dynamics not shown) increases during the interaction period, which indicates coherent interaction (absorption). Due to the larger detuning of the QW states the magnitude of the coherent QW interaction is not as large as in the case of shallow QDs and therefore the increase in the QW carrier density is also smaller. For a larger input pulse area of $\Theta = 3.36\,\pi$ the dynamical behaviour shown in Fig 5.11 is qualitatively similar to Fig. 5.10. Most importantly, the acquired chirp at the SOA's output facet is very similar to that shown in Fig. 5.10.

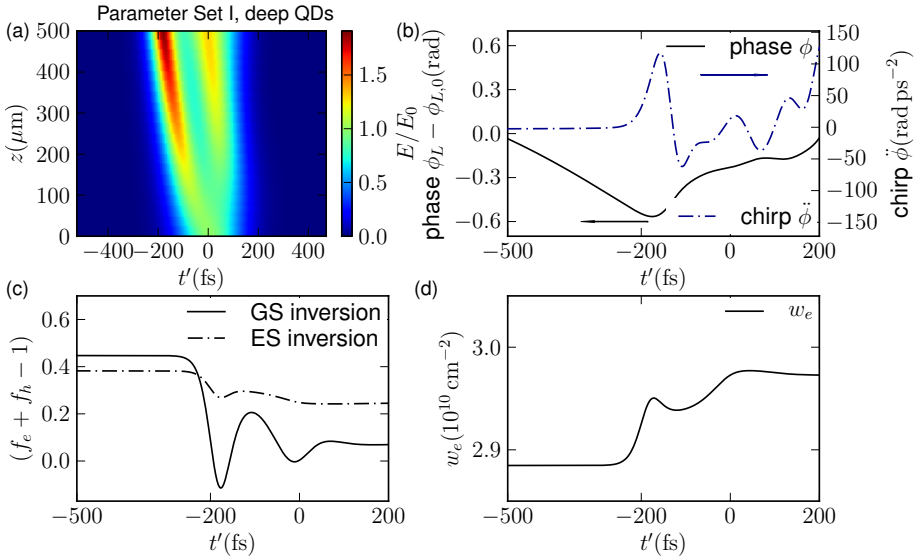

Figure 5.10: Same as Figure 5.3 for deep QDs from Table 3.1. Parameters are $\theta = 2.33\pi$, $T_2 = 100\,\mathrm{fs}$, and $\hbar\delta\omega = 50\,\mathrm{meV}$ (Set I from Table 5.1). Other parameters as in Table 4.1.

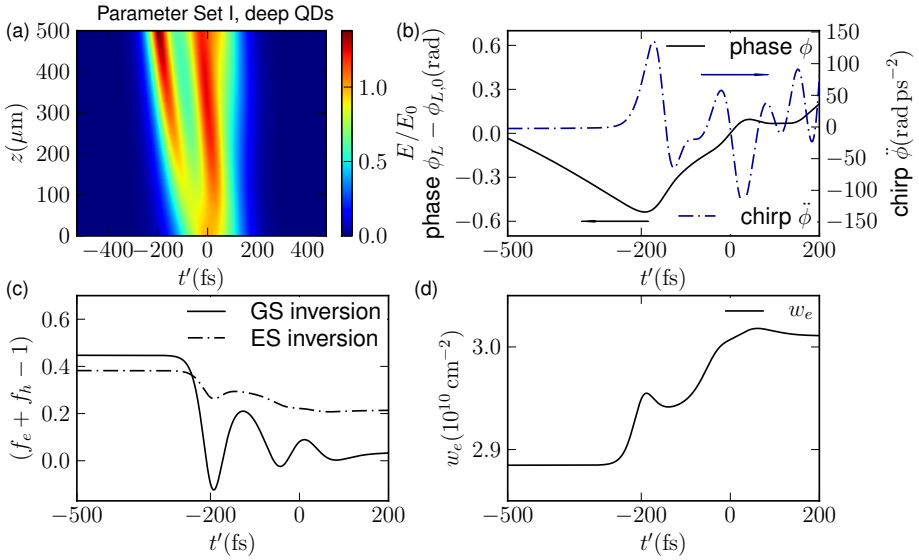

Figure 5.11: Same as Figure 5.10 for an input pulse area $\theta = 3.36\pi$. Parameters are $T_2 = 100\,\mathrm{fs}$ and $\hbar\delta\omega = 50\,\mathrm{meV}$ (Set I from Table 5.1). Other parameters as in Table 4.1.

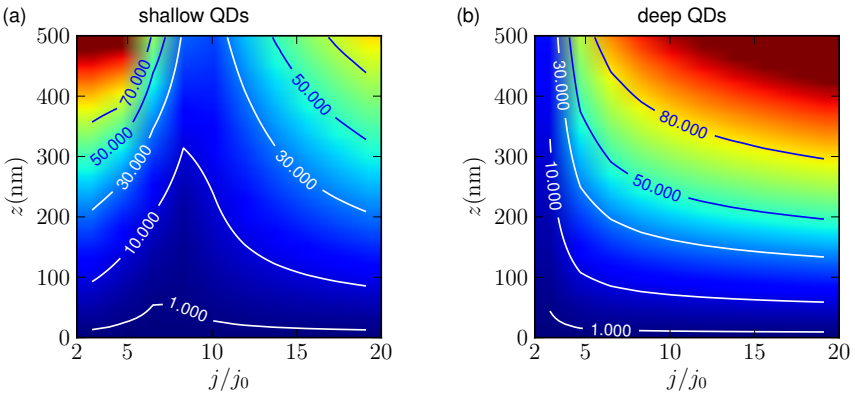

Figure 5.12: Maximum chirp of an input pulse with $FWHM = 150\,\text{fs}$ and input pulse area $\Theta = 2.33\,\pi$ in dependence of the injection current density and the propagation distance for (a) shallow QDs and (b) deep QDs according to Table 3.1. The values at the contour lines indicate the chirp in units of ps^{-2}. Parameters are: QD dephasing time $T_2 = 100\,\text{fs}$ and energy brodening $\hbar\delta\omega = 50\,\text{meV}$. Other parameters as in Table 4.1.

5.5 Injection current dependence

The injection current density dependence of the chirping behaviour is investigated in this section. The maximum attained chirp of the signal in dependence of the injection current density and spatial position z is shown in Fig. 5.12(a) and (b) for shallow and deep QDs according to Table 3.1, respectively. The input pulse is an unchirped Gaussian signal with $FWHM = 150\,\text{fs}$. The pulse area is set to $\Theta = 2.33\,\pi$ in the saturated regime of the QD SOA. For both shallow and deep QDs the maximum chirp of the pulse increases in propagation direction. In the case of shallow QDs shown in Fig 5.12(a) the chirping behaviour for increasing injection current density is characterized first by a decrease in chirp followed by a minimum and then an increase. As a consequence there exists an optimal injection current for which the pulse experiences the least chirp. For deep QDs the maximum chirp of the pulse shown in Fig. 5.12(b) increases monotonically with increasing injection current density.

5.5.1 Role of coherent QW interactions

The impact of coherent interactions of the pulse with the QW states is analyzed in Fig. 5.13 by comparing the full system with coherent interactions of QD and QW states to the reduced system, where only the QD dipole dynamics is considered and the QW acts solely as a carrier reservoir. The maximum chirp of the pulse at the output facet as

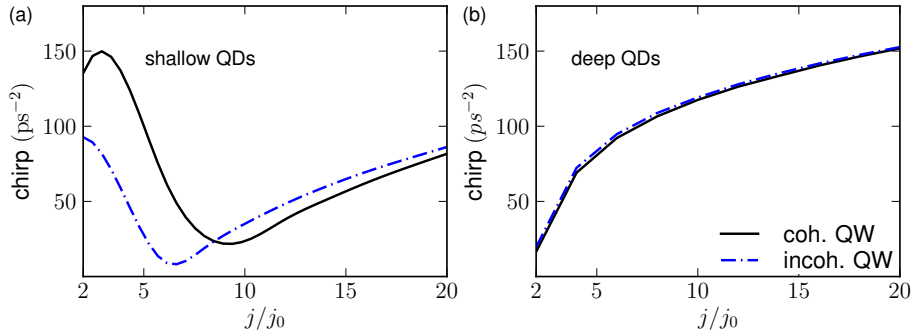

Figure 5.13: Comparison of the maximum chirp attained at the ouput facet with (solid black curves) and without (blue dash-dotted curves) coherent QW interactions for an input pulse with $FWHM = 150\,\mathrm{fs}$ and input pulse area $\Theta = 2.33\,\pi$ in dependence of the injection current density for shallow QDs (a) and deep QDs (b) according to Table 3.1. Same parameters as in Fig 5.12.

a function of the injection current density is shown in Fig. 5.13 (a) and (b) for shallow and deep QDs, respectively. The full simulation of the system is given by the black solid lines, whereas the reduced system where only the QDs are polarizable is shown by the blue dash-dotted curves. In the case of shallow QDs shown in Fig 5.13(a) the coherent QW interaction significantly alters the chirping behaviour. Especially for small input currents $j < 10\,j_0$ the coherent QW interaction significantly enhances the chirp of the pulse. In the deep QD configuration the coherent QW interaction has nearly no effect on the maximum chirp of the signal.

5.6 Comparison of full-field and reduced dynamics

In order to compare the different models time series of the the full field approach (FDTD) from Eqs. (2.8)-(2.9) and the reduced wave equation from Eq. (2.10) of the electric field amplitude, the macroscopic polarization amplitude, and the ground state occupation probability are plotted in Fig. 5.14 at the input facet (left panel) and output facet (right panel) of the amplifier. The inset in Fig. 5.14(c) shows a blowup of the full-field dynamics of the macroscopic polarization density indicating the fast oscillations of the carrier wave. The input signals of the full electric field and the slowly varying envelopes in Fig. 5.14(a) perfectly match, whereas the output signal of the full field dynamics lags behind the dynamics obtained from the reduced system. Other than that, the pulse shape is recovered by the reduced wave equation and only slight deviations in the amplitude occur. The observed time lag of the electric field of the full simulation compared to the

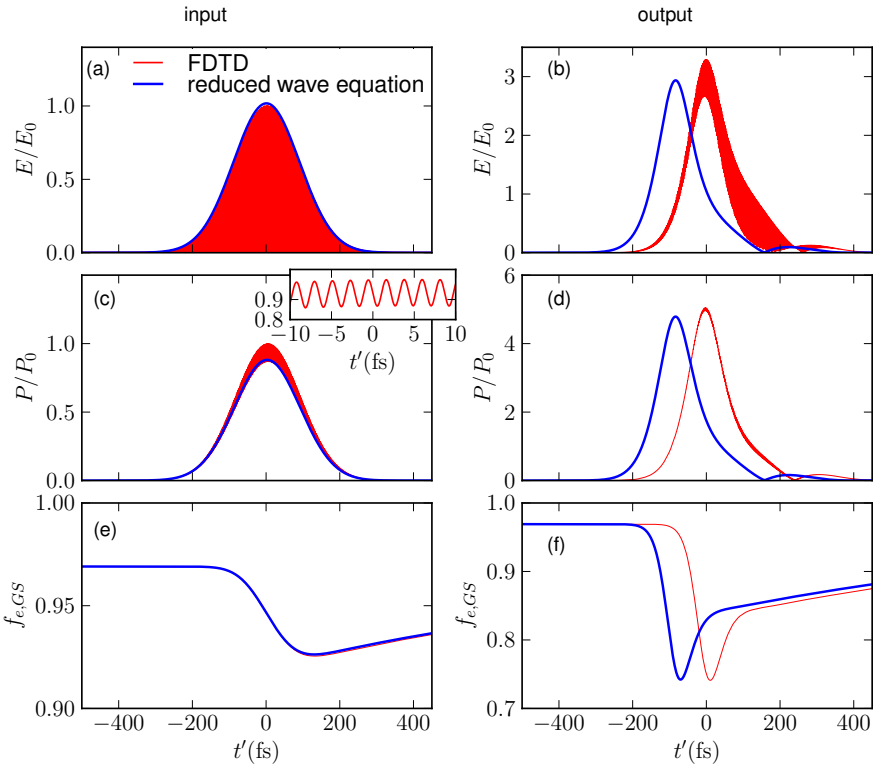

Figure 5.14: Comparison of the dynamics of the full field approach (FDTD) from Eqs. (2.8)-(2.9) and the reduced wave equation approach from Eq. (2.10) for a Gaussian input pulse with $FWHM = 150\,\mathrm{fs}$, $\theta = 0.5\,\pi$ and injection current density $j = 10\,j_0$. The left panel shows the input signals and the right panel the output signals in dependence of time t'. (a) and (b): Input and output electric field amplitudes, respectively. (c) and (d): Input and output absolute values of the macroscopic polarization density normalized to the FDTD amplitude at the input facet, respectively. The inset shows a blowup around $t' = 0$. (e) and (f): Input and output dynamics of the ground state occupation probability $f_{e,GS}$. $T_2 = 100\,\mathrm{fs}$ and $\hbar\delta\omega = 50\,\mathrm{meV}$. Shallow QDs according to Table 3.1. Other paramters as in Table 4.1

reduced system is also noticeable in the output dynamics of the macroscopic polarization and the QD GS electron probability as shown in Fig. 5.14(d) and (f). The occuring time lag may be caused by refractive index changes caused by the coherent QW interaction that are not captured in the reduced approach.

5.7 Conclusion

To conclude, one observes strong nonlinear self-phase modulation in QD SOAs for input signals with large intensity. The coherent interactions present in the system can lead to pulse breakup. Furthermore, the QW dipole interactions can also lead to an enhancement of the chirp.

Chapter 6

Wave mixing dynamics

Nonlinear phenomena can be used in two general ways, one being the analysis of the properties of the medium that generates them, the other is targeted on applications such as second harmonic generation, optical bistability, phase conjugation etc. The various kinds of nonlinear spectroscopy methods fall into the first category, and one of them, namely the pump-probe spectroscopy has been examined in Sec. 4.1. In this chapter the focus lies on one important application of nonlinear optics, that is four-wave mixing [AGR88a, CHO95, QAS04, BER04]. The fundamental principle of wave mixing relies on the nonlinear interaction between incident signals with different frequencies and propagation directions. The simplest nonlinear wave interaction is created in a three-wave mixing setup shown in Fig. 6.1(a). In such a setup, the medium is excited with a saturating pump field with central frequency ω_2 along one direction (wavevector $\boldsymbol{k}_2$) and a potentially weaker probe field with frequency ω_1 and direction $\boldsymbol{k}_1$. In the degenerate case the frequency components of the pump and probe signal are equal, e.g., $\omega_1 = \omega_2$ and only the incident angles differ from each other. In the non-degenerate setup the frequencies of the incident pump and probe signals are also different from each other. The beating between the pump and probe signals induces field fringes in the medium which result in refractive index variations caused by carrier density modulations. The pump field then scatters off the induced fringes creating the conjugate signal. The

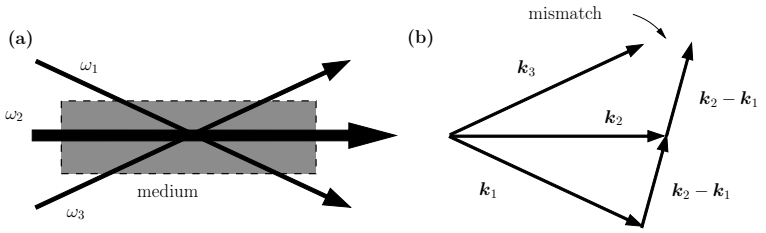

Figure 6.1: (a): Three-wave mixing setup showing incident pump wave ω_2 and probe wave ω_1 along with the conjugate signal ω_3.(b): Illustration of phase mismatch in three-wave mixing.

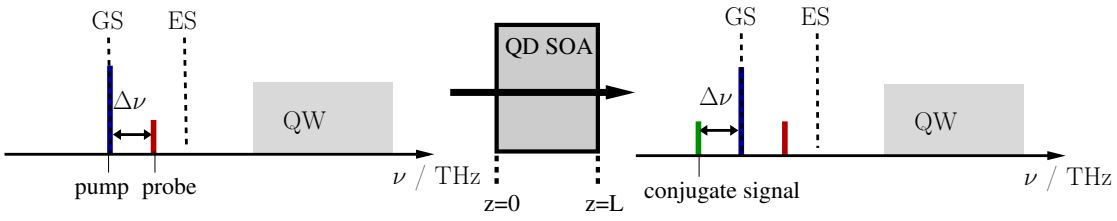

Figure 6.2: Schematic illustration of a three-wave mixing setup for wavelength conversion. The central GS and ES transition frequencies as well as the quasi-continuum of the QW transitions are indicated by the dashed lines and the grey shaded area, respectively. The pump and probe signals are indicated by the dark blue and red lines and the generated conjugate signal is given by the green line.

scattering geometry is sketched in Fig. 6.1(a). Unless the wave-vectors $\mathbf{k}_i$ are all parallel momentum conservation is not perfectly fulfilled and the conjugate signal intensity is reduced. Fig. 6.1(b) illustrates this so-called *phase mismatch* behaviour in three-wave mixing. In the following we restrict ourselves to collinear propagating pulses which are phase-matched. Figure 6.2 schematically illustrates the three-wave mixing setup for the QD SOA system. The central QD ground state and first excited state transition energies are indicated by the dashed lines and the quasi-continuum of QW transitions is indicated by the gray shaded area. The pump pulse is centered around the central QD GS transition frequency ω_{GS} and the detuning frequency of the pump and probe signal is indicated by $\Delta\omega = 2\pi\Delta\nu$. The conjugate signal located at $\omega = \omega_{GS} - \Delta\omega$ is given by the green line while the input probe pulse is indicated by the red line. If not stated otherwise, the amplitude ratio of input pump signal amplitude E_{pump} and probe signal amplitude E_{probe} is set to $E_{pump} = 10\,E_{probe}$ in the following. As a measure for the nonlinear wavelength conversion efficiency ΔFWM the ratio of the input probe pulse intensity at frequency $\omega_{GS} + \Delta\omega$ to the output intensity at the conjugate frequency $\omega_{GS} - \Delta\omega$ is used (ratio between red and green signals in Fig. 6.2)

$$\Delta FWM = \frac{|E(\omega_{GS} - \Delta\omega, z = L)|^2}{|E_{probe}(\omega_{GS} + \Delta\omega, z = 0)|^2}. \tag{6.1}$$

The amount to which the beating in the field intensity induces a modulation of the charge carrier densities of electrons and holes in the active medium strongly depends on the carrier and polarization lifetimes of the QD and QW states. The polarization lifetime of the QD states is on the order of tens to hundreds of femtoseconds [LOR06], whereas the carrier lifetime is on the order of hundreds of femtoseconds up to picoseconds. This means that effectively the bandwidth of frequency conversion is limited mainly due to the large

carrier lifetimes of the QD levels. Experimental [AKI02] and theoretical [QAS04, BER04] investigations of FWM in QD semiconductor optical amplifiers predict a larger bandwidth of wavelength conversion for QD based devices compared to conventional bulk or QW amplifiers. Three main mechanisms drive the nonlinear wavelength conversion: global carrier density pulsations (CDP), spectral hole burning (SHB) and carrier heating (CH). Global carrier density pulsations refer to variations of the total charge carrier density of the device, whereas spectral hole burning describes local pulsations of the charge carrier density (especially in the QDs). In the case of CDP the charge carrier dynamics of the QDs adiabatically follows the QW charge carrier dynamics. The spectral hole burning component creates a charge carrier oscillation in the QDs that is decoupled from the QW. Carrier heating effects in this context refers to free carrier absorption in the conduction band, where an electron is excited to an energetically higher state. For QD devices these processes are assumed to play a minor role only and are therefore neglected in the analysis of Four-wave mixing in QD SOAs.

Throughout this chapter the optical parameters are $T_2 = 100\,\text{fs}$ and $\hbar\,\delta\omega = 50\,\text{meV}$ (Parameter set I from Table 5.1) and the length of the amplifier is set to $L = 500\,\mu\text{m}$.

6.1 Input power dependence

The input power of the optical signal determines the degree of carrier-induced gain nonlinearity and therefore also determines the nonlinear wavelength conversion efficiency ΔFWM to a large extent. For small input powers the induced carrier density variations are negligible and the gain is in good approximation linear, which means that one can therefore expect the wavelength conversion efficiency in this regime to be small. On the other hand, if the input signal is large, the gain medium will bleach very fast thus leading to a low nonlinear wavelength conversion efficiency. For a Gaussian pulse with fixed width the pulse area scales the amplitude of the pulse and thus also the maximum power density of the signal. On the one hand, in the small signal regime (small input pulse area) the degree of nonlinearity is small and therefore the wavelength conversion efficiency is low. On the other hand, in the high power regime corresponding to large input pulse areas, gain bleaching will reduce the wavelength conversion efficiency. In between these two regime one can expect an optimum input pulse area for which the conversion efficiency has a maximum value.

Figure 6.3 shows the nonlinear wavelength conversion efficiency in dependence of the input pulse area for a frequency detuning of $\Delta\nu = 1\,\text{THz}$ between the pump and probe signal, an input pulse width of $FWHM = 2\,\text{ps}$, and injection currents of $j = 2, 10\,j_0$.

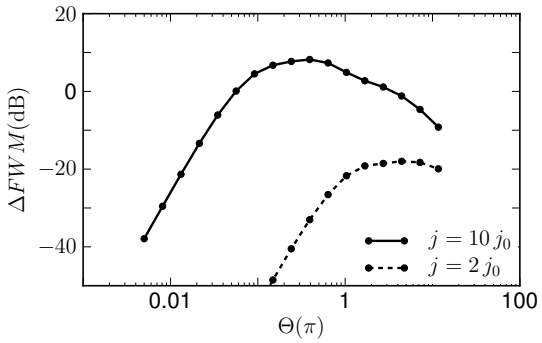

Figure 6.3: Pulse area dependence of the nonlinear wavelength conversion efficiency for two different injection current densities of $j = 2, 10\,j_0$. The frequency detuning between pump and probe signal is $\Delta\nu = 1\,\mathrm{THz}$. The input pulse width is $FWHM = 2\,\mathrm{ps}$. Shallow QDs according to Table 3.1.

In the range of input pulse areas from $\Theta = 5 \times 10^{-2}\,\pi$ to $\Theta = 50\,\pi$ the wavelength conversion efficiency at first increases and then decreases again with increasing input pulse area. The figure indicates that a higher injection current increases the wavelength conversion efficiency. This can be attributed to an increased scattering efficiency and a reduced carrier lifetime of the QD levels in combination with a higher modal gain. For an injection current density of $j = 2\,j_0$ the wavelength conversion efficiency is more than 10 dB smaller compared with the case of an injection current density of $j = 10\,j_0$. The maximum wavelength conversion efficiency is shifted to larger input pulse areas for the case of $j = 2\,j_0$ compared to the case of $j = 10\,j_0$.

6.2 Frequency dependence

For all-optical wavelength conversion it is desirable to have a large bandwidth to allow for example wavelength conversion at multiple wavelengths simultaneously. To this end the frequency dependence of the wavelength conversion efficiency ΔFWM is studied, e.g., the dependence of the generated conjugate field intensity in the output spectra on the frequency difference $\Delta\nu$ between the input pump and probe pulses (see setup in Fig. 6.2) is investigated in this section. A spectrum of the input and output electric field for an injection current density of $j = 10\,j_0$, an input pulse area of $\Theta = 0.5\,\pi$ and $FWHM = 2\,\mathrm{ps}$ is shown in Figure 6.4. In Fig. 6.4(a) the frequency detuning between the pump and probe pulses is $\Delta\nu = 1\,\mathrm{THz}$ and in Fig. 6.4(b) the pump-probe frequency detuning is $\Delta\nu = 3.36\,\mathrm{THz}$. The initial Gaussian shape of the input pump and probe signals given by the black solid curves in Figs. 6.4(a) and (b) are distorted

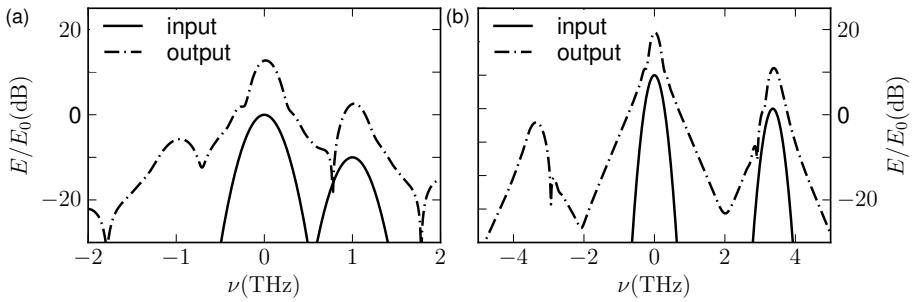

Figure 6.4: Input (black solid curve) and output spectrum (black dash-dotted curve) of three-wave mixing for (a): pump-probe detuning $\Delta\nu = 1\,\mathrm{THz}$ and (b): pump-probe detuning of $\Delta\nu = 3.36\,\mathrm{THz}$. Shallow QDs according to Table 3.1. Other parameters are $FWHM = 2\,\mathrm{ps}$, $\theta = 0.5\pi$, $j = 10\,j_0$.

from their initial shape at the output facet and one can clearly observe a distinct peak in the spectrum at the conjugate frequency. In Fig. 6.4(a) also higher order peaks at $\Delta\nu = \pm 2\,\mathrm{THz}$ appear in the spectrum. The generated conjugate signal in Fig. 6.4(a) has a spectral amplitude that even exceeds the amplitude of the initial input signal, whereas for the larger detuning in Fig. 6.4(b) the generated conjugate signal has an amplitude that is approximately 10 dB smaller in magnitude than the initial input probe amplitude.

The detuning frequency dependence of the wavelength conversion efficiency is shown in Fig. 6.5 for injection currents of $j = 2, 10\,j_0$. The pulse width is again $FWHM = 2\,\mathrm{ps}$. The black solid lines are for negative frequency detunings and the black dash-dotted line shows the frequency dependence of the wavelength conversion efficiency for positive detuning. The qualitative shape of the frequency dependence for both high ($j = 10\,j_0$) and low ($j = 2\,j_0$) injection currents shown in Figs 6.5(a) and (b), respectively, is very similar. For the case of strong current injection ($j = 10\,j_0$) from Fig. 6.5(a) the wavelength conversion efficiency is more than 20 dB larger compared to the case of low current injection ($j = 2\,j_0$) Fig. 6.5(b) over the whole range of detuning frequencies. The reason for this behaviour is that for lower injection current densities the QD SOA has a lower modal gain and also a reduced QW-QD scattering efficiency leading to enhanced QD charge carrier lifetimes. For $j = 10\,j_0$ the initial value of the wavelength conversion efficiency for a detuning of $\Delta_\nu = 1\,\mathrm{THz}$ is above 0 dB. The frequency converted signal at the output facet thus has a higher intensity than the input probe signal at this detuning frequency. The symmetry of the wavelength conversion efficiency for positive and negative detuning is very high for both injection currents. For an injection current density of $j =$

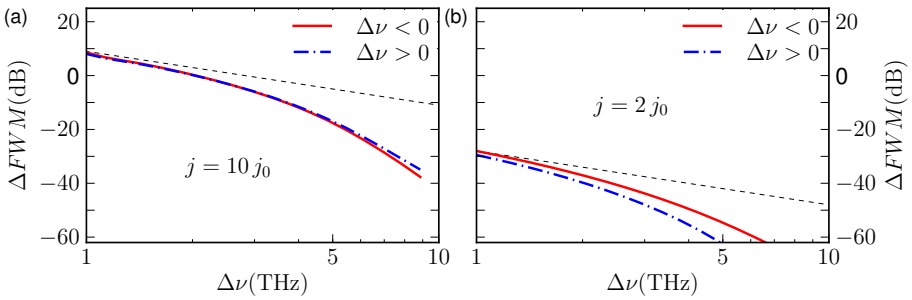

Figure 6.5: Frequency dependence of the nonlinear wavelength conversion efficiency for shallow QDs for different injection current densities of (a): $j = 10\,j_0$ and (b): $j = 2\,j_0$. Red solid and blue dash-dotted lines indicate positive and negative frequency detuning, respectively. The black dashed lines indicate the $-20\,$dB/dec line. The input pulse area is $\Theta = 0.5\,\pi$ and the input pulse width is $FWHM = 2000\,$fs.

$10\,j_0$ the positive and negative detuning behaviour is almost identical, whereas for $j = 2\,j_0$ the asymmetry in the wavelength conversion efficiency increases to several dB with an enhanced conversion efficiency for negative frequency detunings as visible in Fig. 6.5(b). The asymmetry can be attributed to the asymmetry of the gain spectrum. For $j = 2\,j_0$ the QD excited state is absorptive (see Fig. 4.13) and therefore the gain spectrum is more asymmetric around the QD GS transition in comparison to the spectrum for an injection current of $j = 10\,j_0$.

Regarding the frequency dependence a typical rate at which the efficiency of bulk and QW devices decreases with increasing detuning frequency is given by the $-20\,$dB/dec line. As shown in Fig. 6.5(a) the high conversion efficiency for $j = 10\,j_0$ at a detuning of $\Delta\nu = 1\,$THz drops at a rate faster than $-20\,$dB/dec with increasing detuning frequency indicating that one is beyond a frequency range where the performance in this regard is better than that of a QW or bulk device.

The detuning dependence for a Gaussian input signal with $FWHM = 10\,$ps at $j = 10\,j_0$ is shown in Fig. 6.6. The larger temporal pulse width allows the detuning in the lower frequency range to be extended down to 200 GHz while still maintaining a clear spectral separation of the pump, prope and conjugate signals. The negative and positive detuning curves show nearly 0 dB separation indicating nearly perfect symmetry of the wavelength conversion efficiency. The initial wavelength conversion efficiency is approximately 10 dB at 200 GHz detuning, which is a comparable value to the shorter 2 ps input signal conversion efficiency at 1 THz. A 20 dB/dec decrease is obtained at approximately 500 GHz in this case.

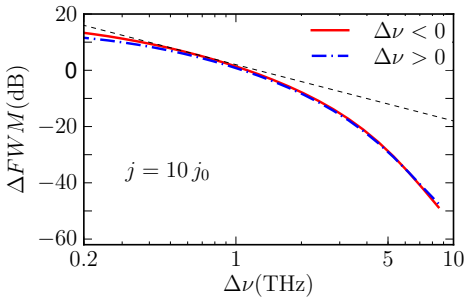

Figure 6.6: Same as Fig. 6.5(a) for an input pulse with $FWHM = 10\,\text{ps}$ and an extended frequency range from $0.2 - 10\,\text{THz}$.

6.2.1 Impact of the band structure

In this section the impact of the band structure on the wavelength conversion efficiency is examined. To this end the deep QD band structure from Table 3.1 and the associated scattering rates are used in the evaluation of the wavelength conversion efficiency.

The frequency dependence of FWM for the deep QD configuration is shown in Fig. 6.7 again for injection current densities of $j = 2\, j_0$ and $j = 10\, j_0$. As a main difference to the case of shallow QDs from Fig. 6.5 the asymmetry of the wavelength conversion efficiency for deep QDs is high for an injection current of $j = 10\, j_0$ and for deep QDs the positively detuned prope signals deliver higher wavelength conversion efficiencies compared to negatively detuned signals. This also stands in opposition to the asymmetric case for shallow QDs shown in Fig. 6.5(b). For a low value of the injection current ($j = 2\, j_0$) the wavelength conversion efficiency is highly symmetric. In the shallow dot case the behaviour is opposite (higher asymmetry for low current injection of $j = 2\, j_0$ and low asymmetry for high current injection of $j = 10\, j_0$). Again, this behaviour is closely connected to symmetry of the gain spectrum in the vicinity of the QD GS transition.

6.2.2 Injection current dependence and role of coherent QW interactions

The current injection strength changes the scattering efficiency between QD and QW states and therefore impacts the carrier dynamics of the QD-QW system.

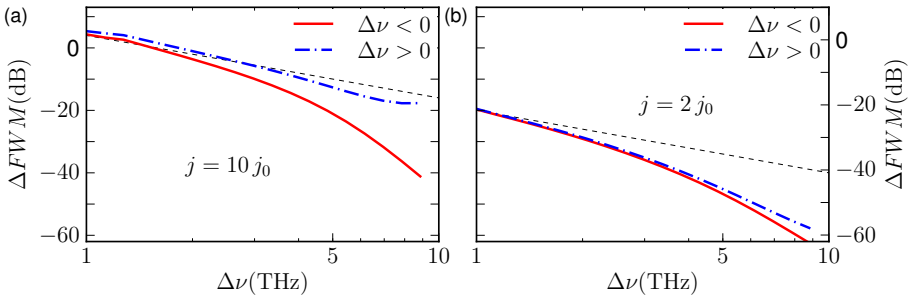

Figure 6.7: Same as Fig. 6.5 for deep QDs. The input pulse area is $\Theta = 0.5\,\pi$. The input pulse width is $FWHM = 2\,\text{ps}$.

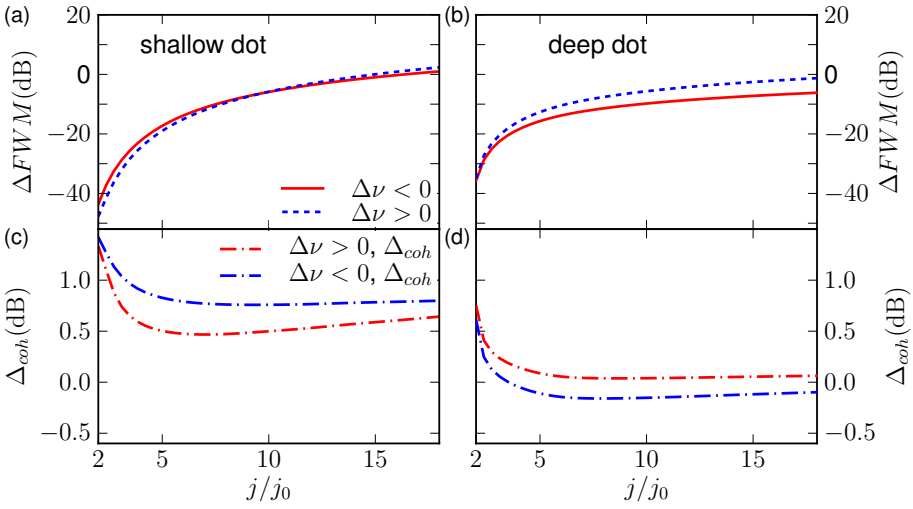

Figure 6.8: Injection current density dependence of ΔFWM for (a): shallow QDs and (b): deep dots. Red solid and blue dashed lines indicate positive and negative frequency detunings of $\Delta\nu = \pm 3\,\text{THz}$, respectively. (c) and (d): Difference Δ_{coh} of ΔFWM due to coherent QW interaction for shallow and deep QDs, respectively . The input pulse area is $\Theta = 0.5\,\pi$and the input pulse width is $FWHM = 2\,\text{ps}$.

For the investigation of the injection current density dependence of the wavelength converstion efficiency the pump-probe detuning frequency is set to $\Delta\nu = \pm 3\,\mathrm{THz}$. The wavelength conversion efficiency for shallow and deep QDs in dependence of the injection current density is shown in Figure 6.8(a) and (b), respectively, for a range of injection currents from $j = 2 - 18\,j_0$. The red solid curves mark the case of negative frequency detuning while the blue dashed curve indicates positive frequency detunings between input pump and probe signal. The shallow QD and deep QD behaviour is qualitatively similar. It is characterized by a quick initial increase with growing injection up to a value of approximately $5\,j_0$, from whereon the rate of increase in the wavelength conversion efficiency gradually becomes lower. For shallow QDs shown in Fig. 6.8(a) the negative and positive detuning curves show a crossover at approximately $12\,j_0$,from whereon the wavelength conversion efficiency for positive pump-probe detuning exceeds the value for negative pump-probe detuning (and vice versa before). In contrast, for deep QDs shown in Fig. 6.8(b) the injection current dependence for positive detunings always exceeds the curve for negative pump-probe detuning.

To quantify the effect of coherent QW interactions on the wavelength conversion efficiency it is useful to introduce a measure $\Delta_{coh} = \Delta FWHM_{coh} - \Delta FWHM_{incoh}$, where $\Delta FWHM_{coh}$ and $\Delta FWHM_{incoh}$ refer to the wavelength conversion efficiencies with and without coherent QW interactions included. The impact of coherent QW interactions to the injection current dependence is shown in Fig. 6.8(c) and (d) for shallow and deep QDs, respectively. The deviations of the wavelength conversion efficiency due to coherent interaction of the QW states is of the order of $\approx$ 1dB. For the case of shallow QDs shown in Fig. 6.8(c) the coherent QW interaction always leads to an enhancement of the wavelength conversion efficiency. For the case of deep QDs depicted in Fig. 6.8(d) the scenario is different. Here, for currents larger than $5\,j_0$ the coherent QW interaction leads to a slight enhancement of the wavelength conversion efficiency for negative pump-probe detunings and a reduction for positive detunings. Overall, the impact of coherent QW interaction on the wavelength conversion efficiency is small. One can therefore conclude that the spectral hole burning component of the QW states contributing to the wavelength conversion efficiency is negligible.

Chapter 7

Summary and outlook

In this thesis the dynamics of quantum dot based semiconductor optical amplifiers has been studied. A semiclassical model has been set up that is able to predict the dynamics of QD SOAs and give further insight into the the interplay between structure and device performance. The predictive power of the presented approach makes the results interesting for experimentalists as well as for the community engaged in QD modelling.

On the level of Maxwell-Bloch equations the dynamics of the amplifier is governed by material equations for the microscopic interband polarizations and electron and hole populations of the quantum dot and quantum well states coupled to propagation equations for the electric field deduced from Maxwell's equations. The full field dynamics in one spatial dimension and a reduced set of equations based on the rotating wave and slowly varying envelope approximations have been introduced. By exploiting the limitations and the range of validity of the reduced set of equations it is now possible to choose the appropriate modeling approach for a specific physical problem. As an essential part of the material model microscopically calculated carrier-carrier (Auger) scattering rates between the QW states and the bound QD states have been calculated for QDs with a ground state and a first excited state energy level, resulting in a total of sixteen possible Auger processes between the quantum well and quantum dot states. The resulting Auger scattering rates in dependence of the quantum well charge carrier density and temperature have been presented in chapter 3.

In chapter 4 the spectral properties and the static linewidth enhancement factor, or static α-factor, have been analyzed in dependence of frequency and injection current density. The separate contributions of the quantum dot ground and excited state and QW dipole interactions to the linewidth enhancement factor have been examined and it has been shown that the quantum well dipole interaction leads to significant enhancement of the linewidth enhancement factor compared to the case without coherent QW interactions.

The frequency dependence of the linewidth enhancement factor exhibits local minima, which generally do not coincide with the spectral gain maximum. This knowledge can be

beneficial for cavity design. A low value of the linewidth enhancement factor can enance the stability properties of semiconductor lasers under external optical injection or optical feedback.

The dynamic gain properties in response to ultrashort subpicosecond pulses have been investigated in terms of single-color pump-probe simulations resonant to the QD GS transition. With the microscopic Auger scattering rates at hand it was possible to quantify the strength of the different scattering channels. For shallow QDss it was found that the ultrafast recovery dynamics associated with quantum dot based semiconductor optical amplifiers is driven by the cascading relaxation scattering channel. An excellent agreement between experimental and simulated gain recovery dynamics could be obtained for shallow QD structures over a range of injection current densities in the high excitation regime. Here, carrier heating was found to play an essential role in order to accurately describe the current injection dependent gain recovery.

The pulse propagation dynamics for ultrashort input signals was investigated in chapter 5. Nonlinear self-phase modulation measured in terms of the acquired chirp of the signal was investigated for deep and shallow QD structures. In contrast to the enhanced static linewidth enhancement factor of shallow QDs the dynamical chirp of the ultrashort signals was lower for the shallow QDs. The static linewidth enhancement factor can therefore not be used in the nonlinear gain regime to predict the coupling of amplitude and phase. For the shallow QD structure the injection current dependence of the chirp has a minimum above transparency indicating optimal operating conditions.

In chapter 6 nonlinear wavelength conversion with nondegenerate four-wave mixing was examined. For large frequency detunings above $1\,THz$ the QD structures still show a high wavelength conversion efficiency, which is attributed to efficient carrier-carrier scattering between the QW and QD states, thus outperforming conventional QW or bulk devices. The high bandwidth of nonlinear wavelength conversion in QD SOAs is mainly driven by spectral hole burning in the QDs and the impact of QW dipole interactions is insignificant both for deep and shallow quantum dot devices.

For future investigations regarding quantum dot semiconductor optical amplifiers several topics would be of high interest. The model could be extended in several ways. Based on the microscopic model Coulomb renormalizations of the QD and QW single particle states can be taken into account into the dynamic device simulation. Their impact on the spectral properties and the dynamic behaviour of the gain recovery dynamics and the chirping behaviour of single pulses would be of great interest. Furthermore, the dephasing time of the optical polarization of the QDs has proven to be a sensitive parameter of the system. Therefore, taking into account a density dependent dephasing time would

also be of high interest. The inclusion of spontaneous emission noise in the electric field dynamics and the noise figure in combination with pulse propagation is an interesting research topic.

Regarding the dynamical aspects the investigation of gain recovery dynamics in a two-color pump-probe setup is highly interesting from an experimental and also theoretical point of view, since it can deliver valuable insight into further details on the internal carrier dynamics and dipole interactions.

Appendix A

Parameters

A.1 Quantum dot energy level spacings

Parameter	Symbol	Value		Unit
		Shallow QD	Deep QD	
Energy separation of QD GS to QW conduction band edge	$\Delta E_{e,m=0}$	74	210	[meV]
Energy separation of QD ES to QW conduction band edge	$\Delta E_{e,m=\pm1}$	24	146	[meV]
Energy separation of QD GS to QW valence band edge	$\Delta E_{h,m=0}$	40	50	[meV]
Energy separation of QD GS to QW valence band edge	$\Delta E_{h,m=\pm1}$	20	44	[meV]
QD electron energy level spacing	Δ_e	50	64	[meV]
QD hole energy level spacing	Δ_h	20	6	[meV]

Table A.1: Quantum dot energy level spacings of deep and shallow QDs.

A.2 Material parameters

Parameter	**Symbol**	**Value**	**Unit**
Device temperature	T	300	[K]
Number of QW layers	a^L	10	
Background permittivity	ϵ_{bg}	14.2	
GS optical transition energy	$\hbar\omega_{GS}$	0.96	[eV]
Geometric confinement factor	Γ	0.2	
QD dipole moment	μ	0.6	[e_0 nm]
QW dipole moment	μ^k	0.5	[e_0 nm]
QW charge carrier lifetime	T_1^{QW}	60	[fs]
QW polarization dephasing time	T_2^{QW}	120	[fs]
bimolecular recombination rate in the QW	B^s	700	[$ns^{-1}nm^{-2}$]
Einstein coefficient of QD GS	W_{GS}	0.45	[ns^{-1}]
Einstein coefficient of QD ES	W_{ES}	0.55	[ns^{-1}]
In-plane area	A	2×10^9	[nm^{-2}]
Device length	L	500	[μm]
Height of QW layer	h^{QW}	4	[nm]
2D QD density	N^{QD}	10^{11}	[cm^{-2}]
Efective electron mass	m_e	0.043	[m_0]
Efective hole mass	m_h	0.45	[m_0]

Table A.2: Parameters used throughout this work unless stated otherwise.

A.3 Optical parameter sets

QD type		Value		Unit
		Set I	**Set II**	
QD dephasing time	T_2	100	30	[fs]
QD inhomogeneous broadening	$\hbar\delta\omega$	50	20	[meV]

Table A.3: Optical parameter sets used in Chapter 5.

A.4 Transparency current densities

QD type	T_2(fs)	$\hbar\delta\omega$(meV)	μ^k(e$_0$ nm)	j_0 (e$_0$ nm^{-2}fs^{-1})
shallow	100	50	0	2.47×10^{-9}
	100	50	0.5	2.85×10^{-9}
	30	20	0	3.21×10^{-9}
	30	20	0.5	3.72×10^{-9}
deep	100	50	0	1.32×10^{-9}
	100	50	0.5	1.37×10^{-9}
	30	20	0	1.39×10^{-9}
	30	20	0.5	1.45×10^{-9}

Table A.4: Transparency current densities j_0 for different paramters used throughout this work.

Appendix B

Derivation of the reduced wave equation

B.1 Derivation of the reduced wave equation

The derivation of the propagation equation from Maxwell's Equations that is used throughout this work is adapted from [BIN95, KNO92]. Starting point are Maxwell's Equations governing the space-time evolution of the electric field. We consider the case of a non-magnetic material, e.g. ($\mathbf{B} = \mu_0 \mathbf{H}$)

$$\nabla \cdot \mathbf{D} = \rho_f, \tag{B.1}$$

$$\nabla \cdot \mathbf{B} = 0, \tag{B.2}$$

$$\nabla \times \mathbf{E} = -\frac{\partial \mathbf{B}}{\partial t}, \tag{B.3}$$

$$\nabla \times \mathbf{H} = \mathbf{J}_f + \frac{\partial \mathbf{D}}{\partial t}, \tag{B.4}$$

where ρ_f and J_f are the free charge density and current density, respectively. The electric displacement field is given by $\mathbf{D} = \epsilon_0 \mathbf{E} + \mathbf{P}$, where the polarization $\mathbf{P}$ is the macroscopic spatial average of the microscopic dipole density. Taking $\nabla\times$ of Eq. (B.3) and using Eq. (B.4) one obtains the fundamental wave equation

$$\nabla^2 \mathbf{E} - \nabla(\nabla \cdot \mathbf{E}) = \frac{1}{c^2}\frac{\partial^2 \mathbf{E}}{\partial t^2} + \mu_0 \frac{\partial^2 \mathbf{P}}{\partial t^2} + \mu_0 \frac{\partial \mathbf{J}_f}{\partial t} \tag{B.5}$$

The transversal part of this equation is the propagation equation

$$\nabla^2 \mathbf{E}_T - \frac{1}{c^2}\frac{\partial^2 \mathbf{E}_T}{\partial t^2} = \mu_0 \frac{\partial^2 \mathbf{P}_T}{\partial t^2} + \mu_0 \frac{\partial \mathbf{J}_{f,T}}{\partial t}. \tag{B.6}$$

Furthermore, assuming that the free current density is negligible ($\mathbf{J}_f = 0$). The electric field is of the general form

$$\mathbf{E}_T(\mathbf{r},t) = \mathbf{E}(\mathbf{r},t)e^{i(\mathbf{k}_0\mathbf{r}-\omega_0 t)} + c.c. \tag{B.7}$$

and analogously the macroscopic polarization density

$$\mathbf{P}_T(\mathbf{r},t) = \mathbf{P}(\mathbf{r},t)e^{i(\mathbf{k}_0\mathbf{r}-\omega_0 t)} + c.c.. \tag{B.8}$$

$\mathbf{E}$ and $\mathbf{P}$ are the envelopes of E_T and P_T, respectively. In the *Slowly Varying Envelope Approximation* (**SVEA**), the envelopes are assumed to vary little on timescales ω_0^{-1}. Inserting this ansatz one obtains

$$(\nabla + i\mathbf{k}_0)^2\,\mathbf{E} - \frac{1}{c^2}\left(\frac{\partial}{\partial t} - i\omega_0\right)^2 \mathbf{E} = \mu_0\left(\frac{\partial}{\partial t} - i\omega_0\right)^2 \mathbf{P} \tag{B.9}$$

To eliminate the background contribution of the semiconductor polarization the total polarization is split into separate contributions as follows

$$\mathbf{P} = \mathbf{P}_r + \mathbf{P}_{bg},$$

where $\mathbf{P}_r$ denotes the contributions to the polarization that are in resonance to the input electric field, whereas $\mathbf{P}_{bg}$ contains all off-resonant contributions. Assuming that $\mathbf{P}_{bg}$ responds linearly to $\mathbf{E}$ and that the response function is a rapidly converging Taylor expansion around the resonant frequency ω_0. One can then write

$$\mathbf{P}_{bg}(\mathbf{r},\omega) = \epsilon_0\chi_{bg}(\omega)\mathbf{E}(\mathbf{r},\omega) \tag{B.10}$$

With

$$\chi_{bg}(\omega) = \chi_{bg}(\omega_0) + (\omega-\omega_0)\chi'_{bg}(\omega_0) + \frac{1}{2}(\omega-\omega_0)^2\chi''_{bg} \tag{B.11}$$

one obtains by Fourier transforming $\mathbf{P}_{bg}(\mathbf{r},\omega) = \int dt\,\mathbf{P}_{bg}(\mathbf{r},t)e^{i\omega t}$

$$\begin{aligned}\mathbf{P}_{bg}(\mathbf{r},t) =& \epsilon_0\int\frac{d\omega}{2\pi}\mathbf{P}_{bg}(\mathbf{r},\omega)e^{-i\omega t}\\ \approx& \left(\chi_{b,0} + \chi'_{b,0}(i\frac{\partial}{\partial t} - \omega_0) + \frac{1}{2}\chi''_{b,0}(i\frac{\partial}{\partial t} - \omega_0)^2\right)\mathbf{E}(\mathbf{r},t),\end{aligned} \tag{B.12}$$

since

$$\int \frac{d\omega}{2\pi}(\omega-\omega_0)\mathbf{E}(\mathbf{r},\omega)e^{-i\omega t} = (i\frac{\partial}{\partial t}-\omega_0)\int \frac{d\omega}{2\pi}\mathbf{E}(\mathbf{r},\omega)e^{-i\omega t} = (i\frac{\partial}{\partial t}-\omega_0)\mathbf{E}(\mathbf{r},t) \quad \text{(B.13)}$$

With the following definition:

$$\chi(\omega) := \chi_{bg}(\omega) - \omega_0\chi'_{bg}(\omega) + \frac{1}{2}\omega_0^2\chi''_{bg}(\omega)$$

Setting

$$\begin{aligned}
&\chi(\omega_0) = \chi_{bg}(\omega_0) - \omega_0\chi'_{bg}(\omega_0) + \frac{1}{2}\omega_0^2\chi''_{bg}(\omega_0) =: \chi_0\\
&\chi'(\omega_0) \approx \chi'_{bg}(\omega_0) - \omega_0\chi''_{bg}(\omega_0) =: \chi'_0\\
&\chi''(\omega_0) \approx \chi''_{bg}(\omega_0) =: \chi''_0
\end{aligned}$$

Eq. (B.12) can be rewritten as

$$\mathbf{P}_{bg}(\mathbf{r},t) \approx \left(\chi_0 + i\chi'_o\frac{\partial}{\partial t} - \frac{1}{2}\chi''_o\frac{\partial^2}{\partial t^2}\right)\mathbf{E}(\mathbf{r},t) \quad \text{(B.14)}$$

Inserting this into Eq. (B.9) gives

$$\begin{aligned}
(\nabla + i\mathbf{k}_0)^2\,\mathbf{E} - \frac{1}{c^2}\left(\frac{\partial}{\partial t} - i\omega_0\right)^2\mathbf{E} =\\
\mu_0\left(\frac{\partial}{\partial t} - i\omega_0\right)^2\left[\mathbf{P}_r + \epsilon_0\left(\chi_0 + i\chi'_0\frac{\partial}{\partial t} - \frac{1}{2}\chi''_0\frac{\partial^2}{\partial t^2}\right)\mathbf{E}\right] \quad \text{(B.15)}
\end{aligned}$$

For the evaluation of the righthand side in Eq. (B.15) higher than 2nd order time derivatives of the electric field are neglected assuming again that the fields are slowly varying in time. Then the following equation is obtained

$$\begin{aligned}
&(\nabla + i\mathbf{k}_0)^2\,\mathbf{E} - \frac{1}{c^2}\left(\frac{\partial}{\partial t} - i\omega_0\right)^2\mathbf{E} =\\
&\mu_0\left(\frac{\partial}{\partial t} - i\omega_0\right)^2\mathbf{P}_r + \frac{1}{c^2}\chi_0\left(\frac{\partial}{\partial t} - i\omega_0\right)^2\mathbf{E}\\
&+ \frac{1}{c^2}\chi'_0\left(2\omega_0\frac{\partial^2}{\partial t^2}\mathbf{E} - i\omega_0^2\frac{\partial}{\partial t}\mathbf{E}\right) + \frac{1}{2}\frac{1}{c^2}\chi''_0\omega_0^2\frac{\partial^2}{\partial t^2}\mathbf{E}. \quad \text{(B.16)}
\end{aligned}$$

The lengthy prefactors involving ω_0 and $\chi_0, \chi_0', \chi_0''$ can be simplified by introducing a background dispersion relation of the form

$$\mathbf{k}^2(\omega) = \frac{\omega^2}{c^2}\left(1 + \chi(\omega)\right). \tag{B.17}$$

To eliminate the terms containing no spatial or time derivative in Eq. (B.16) one assumes that $k_0 = k(\omega_0)$. Assuming that $\chi_{bg}(\omega)$ $(\chi(\omega))$ is real the first and second derivative of Eq. (B.17) at $\omega = -\omega_0$ are evaluated. Equation (B.15) can then be cast into the form

$$\left(\left[\nabla^2 + 2i\mathbf{k}_0\nabla\right] + 2i\mathbf{k}_0\mathbf{k}_0'\frac{\partial}{\partial t} - (\mathbf{k}_0''\mathbf{k}_0 + \mathbf{k}_0^2)\frac{\partial^2}{\partial t^2}\right)\mathbf{E}(\mathbf{r},t) = \mu_0\left(\frac{\partial}{\partial t} - i\omega_0\right)^2\mathbf{P}_r(\mathbf{r},t). \tag{B.18}$$

In this equation, $\mathbf{P}_r$ contains the response of all transitions around $\hbar\omega_0$.

To further simplify Eq. (B.18) reasonable approximations for waveguide scenarios are now discussed, e.g. Fabry-Perot lasers or optical amplifiers. Denoting the spatial and temporal dimensions of the envelopes with δx, δy, δz, and δt, the derivatives can be approximated by $\partial/\partial x \rightarrow 1/\delta x$, etc. For an order of magnitude estimate one can replace $\mathbf{k}_0\mathbf{k}_0' \rightarrow \omega_0/c^2$ and $\mathbf{k}_0''\mathbf{k}_0 + \mathbf{k}_0'^2 \rightarrow 1/c^2$. Now, if $\omega_0 \gg 1/\delta t$ the second order time derivative on the l.h.s of Eq. (B.18) can be neglected. Furthermore, on the r.h.s only the term with ω_0^2 is kept. The energy level spacing in case of $InGaAs$ QDs is of the order $\hbar\omega \approx 1\,\mathrm{eV}$, so $\omega_0 \approx 1.5\,\mathrm{fs}^{-1}$. For pulse lengths of more than 100 fs the above approximation should be valid.

Concerning spatial effects, the transverse mode structure determines the magnitude of the transverse derivatives. Considering the lowest (TEM_{00}) mode to be dominant and the electric field to extend well into the cladding material, the transverse derivative inside the guiding material is usually negligible.

The wave vector points in propagation direction z, $\mathbf{k}_0 = (0, 0, k_z)$ and typically also $\partial^2\mathbf{E}/\partial z^2$ is small compared to $k_z/\delta z$ and can be neglected resulting in the following wave equation

$$\left(\frac{\partial}{\partial z} + k_0'\frac{\partial}{\partial t}\right)\mathbf{E}(\mathbf{r},t) = \frac{1}{2}i\mu_0\frac{\omega_0^2}{k_0}\mathbf{P}_r(\mathbf{r},t). \tag{B.19}$$

As a last step the group velocity $\nu_g = 1/k_o'$ is introduced with the approximation $k_0 \approx n_{bg}\omega_0/c$, where n_{bg} is the background refractive index $n_{bg} = \sqrt{1+\chi_0}$.

$$\left(\frac{\partial}{\partial z} + \frac{1}{\nu_g}\frac{\partial}{\partial t}\right)\mathbf{E}(\mathbf{r},t) = \frac{1}{2}i\mu_0\frac{\omega_0 c}{n_{bg}}\mathbf{P}_r(\mathbf{r},t). \tag{B.20}$$

In an index guided device the active area is confined to a small region in transverse direction, whereas the transverse electric field extends into the surrounding area depending on the guiding efficiency. Assuming the slowly varying electric field to be of the form

$$\mathbf{E}(\mathbf{r},t) = \mathbf{E}(z,t)\,H(x,y), \tag{B.21}$$

where $H(x,y)$ is the transverse mode distribution in the $x-y$ plane (transverse to the propagation direction) a spatial averaging of Eq. (B.20) over the transverse coordinates [SUG04] can be performed. The formal structure of the wave equation then remains the same, the only difference being a confinement factor Γ in front of the polarization term of the r.h.s of Eq. (B.20) given by

$$\Gamma = \frac{\int_{act} |H(x,y)|^2 dx\,dy}{\int_{cav} |H(x,y)|^2 dx\,dy}. \tag{B.22}$$

An illustration of the opical confinement factor is given in Fig. 4.12. With this Eq. (B.20) takes the final form used throughout this work

$$\left(\frac{\partial}{\partial z} + \frac{1}{\nu_g}\frac{\partial}{\partial t}\right)\mathbf{E}(z,t) = \frac{1}{2}\Gamma i\mu_0\frac{\omega_0 c}{n_{bg}}\mathbf{P}_r(z,t). \tag{B.23}$$

Appendix C

Numerical implementation of the electric field dynamics

This section describes the numerical implementation of the Maxwell-Bloch dynamical equations into computer code.

C.1 Full field dynamics

The full field dynamics requires a numerical integration scheme for the electric and magnetic field dynamics as given by Maxwell's equations. In Maxwells equations, the electric field equation contains the dynamic material polarizations as a source term. They are given by the QD and QW Bloch equations derived in chapter 2. These are systems of coupled time-domain differential equations for the charge carriers and dynamic microscopic polarizations. The numerical method of choice is a finite difference time domain method, which is described in more detail below.

C.1.1 The finite difference time domain method

Examining Maxwell's equations it can be seen that the change in the electric field component in time depends upon the curl of the magnetic field component across space. This results in the basic finite difference time domain (FDTD) time-stepping relation that, at any point in space, the updated value of the E-field in time is dependent on the stored value of the electric field and the numerical curl of the local distribution of the magnetic field in space [YEE66]. The magnetic field is time-stepped in a similar manner. At any point in space, the updated value of the H-field in time is dependent on the stored value of the magnetic field and the numerical curl of the local distribution of the electric field in space. Iterating the electric field and magnetic field updates results in a leapfrog stepping in time domain. The spatial discretization for the continuum equations of the electric and magnetic field components is given by a staggered grid. In the staggered grid method [YEE66] the vector components of the E-field and H-field are spatially staggered

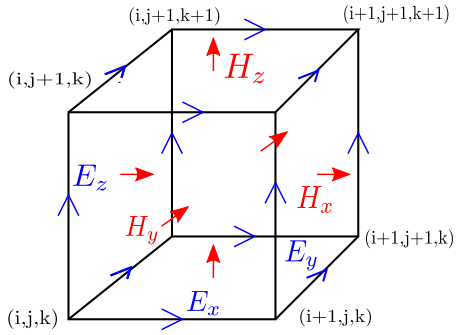

Figure C.1: Illustration of the general Yee cell spatially staggered grid for the electric field and magnetic field vector components in three dimensions.

about rectangular unit cells of a Cartesian computational grid so that each E-field vector component is located midway between a pair of H-field vector components, and vice versa. This scheme, known as a Yee lattice[YEE66], has proven to be very robust, and remains at the core of many current FDTD implementations. In time-domain a leapfrog scheme is used similary, wherein the E-field and H-field updates are staggered so that E-field updates are conducted midway during each time-step between successive H-field updates, and vice versa[YEE66]. This time-stepping scheme avoids the need to solve simultaneous equations, and yields wave propagation without numerical dissipation. This means that the electric field components and the magnetic field components are spatially separated by $\Delta z/2$ and temporally by $\Delta t/2$, where Δz and Δt are the spatial and temporal steps. As a consequence of the macroscopic polarization appearing in the electric field equation of Maxwell's Equations the material equations are associated with the location of the electric field. Figure C.1 illustrates the staggered grid in three dimensions. The structure of the grid in one dimension as it is used throughout the present work remains the same: the electric and magnetic field grid spatial grid points have a respective offset of $\Delta z/2$. The electric field components are solved at the space steps $k\Delta z$ for the time steps $n\Delta t$, whereas the spatial and temporal grid points of magnetic field components are $(h+\frac{1}{2})\Delta z$ and $(n+\frac{1}{2})\Delta t$, respectively. Notationally, the discrete values of the electric field for example are labeled by

$$E_x(h\,\Delta z, n\,\Delta t) = E_x(h,n);\; h \in H := \{1, 2 \ldots Z\},\; n \in \{0, 1 \ldots T\},$$

where $Z \in \mathbb{N}$ is the number of spatial grid points and $T \in \mathbb{N}$ the number of time steps. The set of spatial grid points $H := \{1, 2 \ldots Z\}$ is in the following referred to as the

computational domain. The implemented discretized version of the coupled Maxwell Bloch equations is of the following form

Maxwell equations:

$$H_y(h+\frac{1}{2},n+\frac{1}{2}) = H_y(h+\frac{1}{2},n-\frac{1}{2}) - \frac{\Delta t}{\mu_0 \Delta z}\left[E_x(h+1,n)-E_x(h,n)\right], \tag{C.1}$$

$$E_x(h,n+1) = E_x(h,n) - \frac{\Delta t}{\epsilon_0 \epsilon_r}\left[\frac{H_y(h+\frac{1}{2},n+\frac{1}{2})-H_y(h-\frac{1}{2},n-\frac{1}{2})}{\Delta z} - \Gamma \Delta P\right]. \tag{C.2}$$

Quantum dot Bloch equations:

$$\begin{aligned} p_m^j(h,n+1) =& p_m^j(h,n) + \Delta t \left[-i\tilde{\omega}_m^j - \frac{i}{4}[\tilde{\Omega}_m^j(h,n+1)+\tilde{\Omega}_m^j(h,n)]\times \right. \\ & \times\left(\frac{1}{2}[f_{e,m}^j(h,n+1)+f_{e,m}^j(h,n)]+\frac{1}{2}[f_{h,m}^j(h,n+1)+f_{h,m}^j(h,n)]-1\right) \\ & \left. -\frac{1}{T_2}\frac{1}{2}[p_m^j(h,n+1)+p_m^j(h,n)]\right] =: p_m^j(h,n) + \Delta t \Delta p_m^j, \end{aligned} \tag{C.3}$$

$$\begin{aligned} f_{b,m}^j(h,n+1) =& f_{b,m}^j(h,n) + \Delta t \left(-\mathrm{Im}\left[\frac{1}{2}[\tilde{\Omega}_m^j(h,n+1)+\tilde{\Omega}_m^j(h,n)]\frac{1}{2}[p_m^{j*}(h,n+1)+p_m^{j*}(h,n)]\right]\right. \\ & - W_m \frac{1}{2}[f_{e,m}^j(h,n+1)+f_{e,m}^j(h,n)][f_{h,m}^j(h,n+1)+f_{h,m}^j(h,n)] \\ & \left. + \frac{1}{2}\left[\left.\frac{\partial f_{b,m}^j}{\partial t}\right|_{col}(h,n+1) + \left.\frac{\partial f_{b,m}^j}{\partial t}\right|_{col}(h,n)\right]\right) \end{aligned} \tag{C.4}$$

Quantum well Bloch equations:

$$\begin{aligned} p_k(h,n+1) =& p_k(h,n) + \Delta t \left[-i\tilde{\omega}_k - \frac{i}{4}[\tilde{\Omega}_k(h,n+1)+\tilde{\Omega}_k(h,n)]\times \right. \\ & \times\left(\frac{1}{2}[f_k^e(h,n+1)+f_k^e(h,n)]+\frac{1}{2}[f_k^h(h,n+1)+f_k^h(h,n)]-1\right) \\ & \left. -\frac{1}{T_2^{QW}}\frac{1}{2}[p_k(h,n+1)+p_k(h,n)]\right] =: p_k(h,n) + \Delta t \Delta p_k, \end{aligned} \tag{C.5}$$

$$\begin{aligned} f_k^b(h,n+1) =& f_k^b(h,n) + \Delta t \left(-\mathrm{Im}\left[\frac{1}{2}[\tilde{\Omega}_k(h,n+1)+\tilde{\Omega}_k(h,n)]\frac{1}{2}[p_k^*(h,n+1)+p_k^*(h,n)]\right]\right) \\ & + \Delta t\, \Delta_k^b \end{aligned} \tag{C.6}$$

The term ΔP in Eq. (C.2) is given by the following term in analogy to Eq. (4.5)

$$\Delta P = \frac{2N^{QD}}{h^{QW}} \sum_{j,m} f(\omega_j)\mu_m \Delta p_m^j + \frac{2}{h^{QW}A}\sum_k \mu^k \Delta p_k. \tag{C.7}$$

In the numerical evaluation of the summation over k-states is replaced by an integral

$$\sum_{\mathbf{k}} \rightarrow \frac{A}{(2\,\pi)^2} \int d^2k.$$

The product $\Delta t\, \Delta_k^b$ is given similar to Eq. (2.65)

$$\begin{aligned}\Delta_t \Delta_k^b =& f_b^{k,eq}\left(\mu_b(\frac{1}{2}[w_b(h,n+1)+w_b(h,n)] + \Delta t \frac{1}{2}[W_b^{inc}(h,n+1)+W_b^{inc}(h,n)], T\right) \\ &- f_b^{k,eq}\left(\mu_b(\frac{1}{2}[w_b(h,n+1)+w_b(h,n)], T\right), \end{aligned} \tag{C.8}$$

where

$$\begin{aligned} W_b^{inc}(h,n) =& \frac{j(t)}{e_0} - \tilde{R}_{sp}(\frac{1}{2}[w_e(h,n+1)+w_e(h,n)], \frac{1}{2}[w_h(h,n+1)+w_h(h,n)]) \\ &- 2\sum_{m,j} N^j \frac{1}{2}\left[\left.\frac{\partial f_{b,m}^j}{\partial t}\right|_{col}(h,n+1) + \left.\frac{\partial f_{b,m}^j}{\partial t}\right|_{col}(h,n)\right]. \end{aligned} \tag{C.9}$$

The argument of the collision contribution term denotes that all variables appearing in these terms are evaluated at the respective space and time grid points. The above set of equations are of implicit type. They are solved in an iterative predictor-corrector scheme. Since the magnetic-field equation is updated at a time different from all other dynamic variables it is advanced in the standard fashion. The remaining set of equations is cast into the following form

$$\underline{\underline{S}}^{new} = \underline{\underline{S}}^{old} + \Delta t\, \underline{\underline{F}}(\underline{\underline{S}}^{old}, \underline{\underline{S}}^{new}). \tag{C.10}$$

The state matrix $\underline{\underline{S}}$ contains as column vectors the dynamical variables (except the magnetic field H) at the spatial grid points of the interior of the computational domain, e.g.,$H \setminus \{0, Z\}$. $\underline{\underline{F}}$ represents, minus the standalone value $\underline{\underline{S}}^{old}$, the right hand side of Eqs. (C.2)-(C.5). In each iteration process the value of $\underline{\underline{S}}^{new}$ used in $\underline{\underline{F}}$ is first set to the previous time step value $\underline{\underline{S}}^{old}$ giving updated values $\underline{\underline{S}}^{new}$ by the use of Eq. (C.10). The value of $\underline{\underline{S}}^{new}$ is then iteratively used in the functional $\underline{\underline{F}}$ until two successive values of $\underline{\underline{S}}^{new}$ reach a desired relative accuracy r_{tol}. For the simulations performed throughout this work a value of $r_{tol} = 10^{-6}$ was used.

C.1.2 Stability and boundary conditions

To propagate a distance of one cell in 1D requires a time of $\Delta t = \Delta x/v_g$, where v_g v_g is the group velocity of the considered electric field in the medium. The stability of the implemented finite difference time domain method is then given by the following Courant (or Courant-Friedrichs-Lewy) condition

$$\frac{v_g \Delta_t}{\Delta_x} \leq 1. \tag{C.11}$$

For the simulations $2v_g\Delta_t = \Delta_x$ has been used. In a QD SOA the facet relectivity is close to zero, therefore absorbing boundary conditions are chosen to keep the outgoing E and H fields from being reflected back into the problem space. Normally, in calculating the E field, one needs to know the surrounding H values. At the edge of the problem space one does not have access to the value to one side. However, without field sources outside the problem space the fields at the edge must be propagating outward. If a wave is going toward a boundary in free space, it is traveling at v_g, the group velocity speed. So in one time step of the FDTD algorithm, it travels

$$v_g \Delta t = \frac{\Delta x}{2}, \tag{C.12}$$

which is half a space cell. Reasonable boundary condition are therefore given by setting

$$E_x(0, n) = E_x(1, n-2); \quad E_x(Z, n) = E_x(Z-1, n+2). \tag{C.13}$$

These boundary conditions are easy to implement in computer code by simply storing the respective values of E_x at space points $z = 1, Z-1$ for two time steps and then overriding the values at $z = 0, Z$ with the stored values.

C.2 Reduced wave equation

The reduced wave equation is a single first order partial differential equation. A similar grid based finite difference time domain method is used to solve the problem. The QD and QW Bloch equations are given by Eq. (C.3) and Eq. (C.5), respectively, by replacing $\tilde{\omega}_j^m \rightarrow \tilde{\omega}_j^m - \omega$ and $\tilde{\omega}_k \rightarrow \tilde{\omega}_k - \omega$. The discretized version of the reduced wave equation,

Eq. (2.10), on the same spatial grid as defined above reads:

$$E(h,n+1)=E(h,n)+\nu_g\Delta_t\Bigg(\frac{1}{\Delta x}\Big[E(h+1,n)-E(h,n)\Big] + \frac{1}{4}\Gamma i\mu_0\frac{\omega_0 c}{n_{bg}}\Delta P\Bigg). \tag{C.14}$$

The polarization source term ΔP is given by

$$\Delta P = \frac{2N^{QD}}{h^{QW}}\sum_{j,m} f(\omega_j)\mu_m\,\frac{1}{2}[p_m^j(h,n+1)+p_m^j(h,n)] + \frac{2}{h^{QW}A}\sum_k \mu^k\frac{1}{2}[p_k(h,n+1)+p_k(h,n)]. \tag{C.15}$$

The boundary problem is formulated in terms of the initial values of the dynamic variables on the spatial grid together with the time evolution of the input electric field at the input facet ($z = 0$). The solution in the interior is then advanced in an iterative manner as discussed for the full field solution (see Eq. (C.10)).

Appendix D

Wavefunction overlap integrals

For lense shaped QDs embedded in a quasi-2D quantum well the 3D wavefunction can be separated into a z-component and an in-plane contribution given by Eqs. (3.2) and (3.3) in Sec 2. In this section the wavefunvtion overlap integrals appearing in the Coulomb matrix elements (3.2) are evaluated. Given localized QD states ϕ_α with $\alpha = (m, \mathbf{R})$ indicates the angular momentum of the QD state and its spatial in-plane position and QW states in the absence of QDs, which are assumed to be plane waves of the form $\phi^0_{\mathbf{k}} = (1/(\sqrt{A})e^{i\mathbf{k}\cdot\boldsymbol{\rho}}$ with two-dimensional carrier momentum $\mathbf{k}$. In the presence of QDs the orthogonality requirement of the basis set of wavefunctions is achieved by projecting the plane wave functions onto the subspace orthogonal to the QD wave functions. The QW wavefunctions are then given by orthogonalized plane waves (OPW) $|\phi_{\mathbf{k}}\rangle = (|\phi^0_{\mathbf{k}} - \sum_\alpha |\phi_\alpha\rangle\langle\phi_\alpha|\phi^0_{\mathbf{k}}\rangle)$. As shown in chapter 3 in the large area limit the set of wavefunctions comprised of the QW OPW wavefunctions together with the QD harmonic oscillator wavefunctions form an orthonormal basis for the QD-QW system.

D.1 Quantum well - quantum well overlap integrals

For the case of two QW states appearing in an overlap integral of Eq. (3.2) the overlap integral can be evaluated with Eq. (3.10).

$$\begin{aligned}\langle\phi_{\mathbf{k}}|e^{i\mathbf{q}\cdot\boldsymbol{\rho}}|\phi_{\mathbf{k}'}\rangle = \frac{1}{N_{\mathbf{k}}N_{\mathbf{k}'}}\Big[&\langle\phi^0_{\mathbf{k}}|e^{i\mathbf{q}\cdot\boldsymbol{\rho}}|\phi^0_{\mathbf{k}'}\rangle \\ &+\sum_{\alpha,\alpha'}\langle\phi^0_{\mathbf{k}}|\phi_\alpha\rangle\langle\phi_\alpha|e^{i\mathbf{q}\cdot\boldsymbol{\rho}}|\phi_{\alpha'}\rangle\langle\phi_{\alpha'}|\phi^0_{\mathbf{k}'}\rangle \\ &-\sum_\alpha\langle\phi^0_{\mathbf{k}}|e^{i\mathbf{q}\cdot\boldsymbol{\rho}}|\phi_\alpha\rangle\langle\phi_\alpha|\phi^0_{\mathbf{k}'}\rangle \\ &-\sum_\alpha\langle\phi^0_{\mathbf{k}}|\phi_\alpha\rangle\langle\phi_\alpha|e^{i\mathbf{q}\cdot\boldsymbol{\rho}}|\phi^0_{\mathbf{k}'}\rangle\Big]\end{aligned} \tag{D.1}$$

In the large area limit this expression can be simplified with the use of Eq. (3.11). Due to the random distribution of QDs the translation invariance of the expression is restored, and one obtains

$$\langle\phi_{\mathbf{k}}|e^{i\mathbf{q}\cdot\boldsymbol{\rho}}|\phi_{\mathbf{k}'}\rangle = \delta_{\mathbf{k},\mathbf{q}-\mathbf{k}'}\frac{1}{N_{\mathbf{k}}N_{\mathbf{k}'}}\Bigg[1 + N^{QD}\sum_{m,m'}\langle\phi^0_{\mathbf{k}}|\phi_m\rangle\langle\phi_m|e^{i\mathbf{q}\cdot\boldsymbol{\rho}}|\phi_{m'}\rangle\langle\phi_{m'}|\phi^0_{\mathbf{k}'}\rangle - N^{QD}\sum_m|\langle\phi^0_{\mathbf{k}}|\phi_m\rangle|^2 - N^{QD}\sum_m|\langle\phi_m|\phi^0_{\mathbf{k}'}\rangle|^2\Bigg] \tag{D.2}$$

D.2 Quantum dot - quantum well overlap integrals

When ν and ν' in Eq. (3.2) involve one QW and one QD state the resulting overlap integrals are of type

$$\langle\phi_\alpha|e^{i\mathbf{q}\cdot\rho}|\phi_{\mathbf{k}}\rangle = \frac{1}{N_k}\left(\langle\phi_\alpha|\phi^0_{\mathbf{k}+\mathbf{q}}\rangle - \sum_{\alpha'}\langle\phi_\alpha|e^{i\mathbf{q}\cdot\rho}|\phi_{\alpha'}\rangle\langle\phi_{\alpha'}|\phi^0_{\mathbf{k}}\rangle\right) \tag{D.3}$$

For a QD located at the in-plane position $\mathbf{R}$ one can express

$$\langle\phi_\alpha|e^{i\mathbf{q}\cdot\rho}|\phi^0_{\mathbf{k}}\rangle = \int d^2\rho\phi_m(\boldsymbol{\rho}-\mathbf{R})e^{i\mathbf{q}\cdot\rho}\phi^0_{\mathbf{k}}(\boldsymbol{\rho}) = \langle\phi_m|\phi^0_{\mathbf{k}}\rangle e^{i(\mathbf{k}+\mathbf{q})\cdot R}. \tag{D.4}$$

Assuming non-overlapping QD wave functions for dots at different spatial positions, e.g., if the screening length κ of the Coulomb interaction is much shorter than the in-plane spatial separation of the QDs, Eq. (D.5) can then be written as

$$\langle\phi_m|e^{i\mathbf{q}\cdot\rho}|\phi_{\mathbf{k}}\rangle = \frac{1}{N_k}\left(\langle\phi_m|\phi^0_{\mathbf{k}+\mathbf{q}}\rangle - \sum_{m'}\langle\phi_m|e^{i\mathbf{q}\cdot\rho}|\phi_{m'}\rangle\langle\phi_{m'}|\phi^0_{\mathbf{k}}\rangle\right)e^{i(\mathbf{k}+\mathbf{q})\cdot R}. \tag{D.5}$$

Appendix E

Coulomb renormalizations

The Coulomb energy renormalizations in a QW-QD many-body system are given in the following. A numerical implementation on the basis of orthogonalized plane waves will be subject to further investigations. The different contributions to the total single-particle energy renormalization for QD and QW states are listed in the following sections.

Screened Hartree energy shifts

Beginning with the screened Hartree contribution to the energy renormalization of a QD state one finds

$$\Delta\varepsilon^{SH}_{b,\alpha} = \sum_{b',\alpha'} W^{b,b'}_{\alpha\alpha'\alpha'\alpha} f^{b\prime}_{\alpha'} + \sum_{b',\mathbf{k}'} W^{b,b'}_{\alpha\mathbf{k}'\mathbf{k}'\alpha} f^{b\prime}_{\mathbf{k}'} = \Delta\varepsilon^{SH}_{b,\alpha}|_{QD} + \Delta\varepsilon^{SH}_{b,\alpha}|_{QW}. \tag{E.1}$$

The energy renormalization is made up of separate terms originating from interaction with other QD states ($\Delta\varepsilon^{SH}_{b,\alpha}|_{QD}$) and QW states ($\Delta\varepsilon^{SH}_{b,\alpha}|_{QW}$). For the QD contribution one obtains

$$\Delta\varepsilon^{SH}_{b,\alpha}|_{QD} = \sum_{j} \sum_{b',m'} \frac{1}{A} \sum_{\mathbf{q}} W^{b,b'}_{q} \langle\phi_\alpha|e^{-i\mathbf{q}\cdot\rho}|\phi_\alpha\rangle\langle\phi_{(m',\rho_j)}|e^{i\mathbf{q}\cdot\rho}|\phi_{(m',\rho_j)}\rangle f^{b'}_{\alpha'}. \tag{E.2}$$

In the following the shorthand notation $|m\rangle := |\phi_{m,0}\rangle$ for the single particle QD wavefunction at the in-plane spatial position $\rho = 0$ is introduced. Note, that the above expression has an in-plane spatial dependence through $\alpha = (m, \rho_i)$. Evaluating the configurational average one obtains an expression for the average shift of a QD level

$$\Delta\varepsilon^{SH}_{b,m}|_{QD} = \frac{1}{N} \sum_{i,j} \sum_{b',m'} \frac{1}{A} \sum_{\mathbf{q}} W^{b,b'}_{q} \langle m|e^{-i\mathbf{q}\cdot\rho}|m\rangle\langle m'|e^{i\mathbf{q}\cdot\rho}|m'\rangle e^{i\mathbf{q}(\rho_j-\rho_i)} f^{b'}_{m'}. \tag{E.3}$$

As a final result the QD contribution to the QD Hartree energy shifts is given by

$$\begin{aligned}\Delta\varepsilon^{SH}_{b,m}|_{QD} =& N^{QD}\sum_{b',m'} W^{b,b'}_{q=0} f^{b'}_{m'} \\ &+ \sum_{b',m'}\frac{1}{A}\sum_{\mathbf{q}} W^{b,b'}_{q}\langle m|e^{-i\mathbf{q}\cdot\rho}|m\rangle\langle m'|e^{i\mathbf{q}\cdot\rho}|m'\rangle f^{b'}_{m'} \end{aligned} \tag{E.4}$$

In a similar fashion one can evaluate the QW contribution to the QD energy shifts which results in

$$\begin{aligned}\Delta\varepsilon^{SH}_{b,m}|_{QW} &= \frac{1}{N}\sum_{i}\sum_{b',\mathbf{k}}\frac{1}{A}\sum_{\mathbf{q}} W^{b,b'}_{q}\langle m|e^{-i\mathbf{q}\cdot\rho}|m\rangle\langle\phi_{\mathbf{k}}|e^{i\mathbf{q}\cdot\rho}|\phi_{\mathbf{k}}\rangle e^{-i\mathbf{q}\cdot\rho_i} f^{b'}_{\mathbf{k}} \\ &= \frac{1}{N}\sum_{i}\sum_{b',\mathbf{k}}\frac{1}{A}\sum_{\mathbf{q}} W^{b,b'}_{q}\langle m|e^{-i\mathbf{q}\cdot\rho}|m\rangle\delta_{\mathbf{k},\mathbf{k}+\mathbf{q}} e^{-i\mathbf{q}\cdot\rho_i} f^{b'}_{\mathbf{k}} \\ &= \frac{1}{A}\sum_{b',\mathbf{k}} W^{b,b'}_{q=0} f^{b'}_{\mathbf{k}} = \sum_{b'} W^{b,b'}_{q=0} w_{b'}, \end{aligned} \tag{E.5}$$

involving the QW carrier density $w_{b'}$. Following the same steps as above one finds for the QW screened Hartree energy shifts

$$\begin{aligned}\Delta\varepsilon^{SH}_{\mathbf{k}} &= \sum_{b',\alpha'} W^{b,b'}_{\mathbf{k}\alpha'\alpha'\mathbf{k}} f^{b'}_{\alpha'} + \sum_{b',\mathbf{k}'} W^{b,b'}_{\mathbf{k}\mathbf{k}'\mathbf{k}'\mathbf{k}} f^{b'}_{\mathbf{k}'} \\ &= W^{b,b'}_{q=0}\left\{ N^{QD}\sum_{b',m'} f^{b'}_{m'} + \frac{1}{A}\sum_{\mathbf{k}} f^{b'}_{\mathbf{k}'}\right\} = 0, \end{aligned} \tag{E.6}$$

which vanishes due to global charge neutrality.

Screened exchange energy shifts

The screened exchange contribution to the QD energy renormalization reads

$$\begin{aligned}\Delta\varepsilon^{SF}_{b,m} =& -\sum_{m'}\frac{1}{A}\sum_{\mathbf{q}} W^{b,b}_{q}\left|\langle m|e^{-i\mathbf{q}\cdot\rho}|m'\rangle\right|^2 f^{b}_{m'} \\ &- \sum_{\mathbf{k}'}\frac{1}{A}\sum_{\mathbf{q}} W^{b,b}_{q}\left|\langle m|e^{-i\mathbf{q}\cdot\rho}|\phi_{\mathbf{k}'}\rangle\right|^2 f^{b}_{\mathbf{k}'}. \end{aligned} \tag{E.7}$$

The corresponding energy shifts of the QW stemming from the screened exchange contribution are given by

$$\begin{aligned}\Delta\varepsilon_{\mathbf{k}}^{SF} =& -N^{QD}\sum_{m'}\sum_{\mathbf{q}} W_q^{b,b}\left|\langle\phi_{\mathbf{k}}|e^{-i\mathbf{q}\cdot\rho}|m'\rangle\right|^2 f_{m'}^b \\ & -\sum_{\mathbf{k}'}\frac{1}{A}\sum_{\mathbf{q}} W_q^{b,b}\left|\langle\phi_{\mathbf{k}}|e^{-i\mathbf{q}\cdot\rho}|\phi_{\mathbf{k}'}\rangle\right|^2 f_{\mathbf{k}'}^b. \end{aligned} \tag{E.8}$$

Coulomb hole

The Coulomb hole contribution given by the difference of the screened and unscreened Coulomb potential is evaluated as

$$\Delta\varepsilon_{\nu}^{CH} = \lim_{|r|\to 0}\frac{1}{2}\left[W(|r|) - V(|r|)\right] = \frac{1}{2}\sum_{\nu'}\left[W_{\nu\nu'\nu\nu'} - V_{\nu\nu'\nu\nu'}\right] \tag{E.9}$$

Coulomb enhanced Rabi frequency

Not only the QD and QW single particle energies experience renormalization, also the effective Rabi frequency shifts due to Coulomb interaction. Restricting ourselves to the case of diagonal polarizations (e.g. $p = p_{\nu\nu}$) the Coulomb enhanced Rabi frequency of an arbitrary state (QD or QW) is

$$\tilde{\Omega}_{\nu} = \Omega_{\nu} + \Delta\Omega_{\nu} = \Omega_{\nu} + \frac{1}{\hbar}\sum_{\mu} W_{\mu\mu\nu\nu}^{e,h}\, p_{\mu\mu}. \tag{E.10}$$

Again, the Rabi frequency shifts of the QDs and the QW are evaluated separately,

$$\begin{aligned}\Delta\Omega_m =& \frac{1}{\hbar}\sum_{m'}\frac{1}{A}\sum_{\mathbf{q}} W_q^{e,h}\left|\langle m'|e^{-i\mathbf{q}\cdot\rho}|m\rangle\right|^2 p_{m'm'} \\ & +\frac{1}{\hbar}\sum_{\mathbf{k}'}\frac{1}{A}\sum_{\mathbf{q}} W_q^{e,h}\left|\langle\phi_{\mathbf{k}'}|e^{-i\mathbf{q}\cdot\rho}|m\rangle\right|^2 p_{\mathbf{k}'\mathbf{k}'}. \end{aligned} \tag{E.11}$$

Similarly, the Rabi enhancement of the QW states is given by the following expression

$$\begin{aligned}\Delta\Omega_{\mathbf{k}} =& \frac{1}{\hbar}N^{QD}\sum_{m'}\frac{1}{A}\sum_{\mathbf{q}} W_q^{e,h}\left|\langle m'|e^{-i\mathbf{q}\cdot\rho}|\phi_{\mathbf{k}}\rangle\right|^2 p_{m'm'} \\ & +\frac{1}{\hbar}\sum_{\mathbf{k}'}\frac{1}{A}\sum_{\mathbf{q}} W_q^{e,h}\left|\langle\phi_{\mathbf{k}'}|e^{-i\mathbf{q}\cdot\rho}|\phi_{\mathbf{k}}\rangle\right|^2 p_{\mathbf{k}'\mathbf{k}'}. \end{aligned} \tag{E.12}$$

Acknowledgement

I am greatful for the support that I have received from Prof. Schöll. First of all for giving me the opportunity to work in his group, and in second place for providing a pleasant and inspiring working atmosphere.
My thanks go to the quantum dot subgroup, especially Dr. Kathy Lüdge, for many helpful discussions.
My office colleague Christian Otto I thank especially for discussions regarding scientific matters.
I thank the rest of the group for providing a very pleasant and humorous atmosphere.
Last but not least I thank my family for all the support they provided.

Bibliography

[AGR88a] G. P. Agrawal. Population pulsations and nondegenerate four-wave mixing in semiconductor lasers and amplifiers. JOSA B **5**, 147–159 (1988).

[AGR93a] G. P. Agrawal and C. M. Bowden. Concept of linewidth enhancement factor in semiconductor lasers: its usefulness and limitations. IEEE Photonics Technol. Lett. **5**, 640–642 (1993).

[AKI02] T. Akiyama, H. Kuwatsuka, N. Hatori, Y. Nakata, H. Ebe and M. Sugawara. Symmetric highly efficient (0 dB) wavelength conversion based on four-wave mixing in quantum dot optical amplifiers. IEEE Photon. Technol. Lett. **14**, 1139–1141 (2002).

[BAR63] J. Bardeen. volume 5, Seite 420. (Macmillan, New York, 1963).

[BER04] T. W. Berg, J. Mørk and J. M. Hvam. Gain dynamics and saturation in semiconductor quantum dot amplifiers. New J. Phys. **6**, 178 (2004).

[BIM99] D. Bimberg, M. Grundmann and N. N. Ledentsov. *Quantum Dot Heterostructures*. (John Wiley & Sons Ltd., New York, 1999).

[BIM08a] D. Bimberg. *Semiconductor Nanostructures*. (Springer, Berlin, 2008).

[BIN95] R. Binder and S. W. Koch. Nonequilibrium semiconductor dynamics. Prog. Quantum Electronics **19**, 307 (1995).

[BOR00a] P. Borri, W. Langbein, J. M. Hvam, F. Heinrichsdorff, M. H. Mao and D. Bimberg. Spectral hole-burning and carrier-heating dynamics in InGaAs quantum-dot amplifiers. IEEE J. Sel. Top. Quantum Electron. **6**, 544–551 (2000).

[BOR00] P. Borri, W. Langbein, J. M. Hvam, F. Heinrichsdorff, M. H. Mao and D. Bimberg. Ultrafast Gain Dynamics in InAs–InGaAs Quantum-Dot Amplifiers. IEEE Photon. Technol. Lett. **12** (2000).

[BOR02] P. Borri, W. Langbein, S. Schneider, U. Woggon, R. L. Sellin, D. Ouyang and D. Bimberg. Exciton relaxation and dephasing in quantum-dot amplifiers from room to cryogenic temperature. IEEE J. Sel. Top. Quantum Electron. **8**, 984–991 (2002).

[BOR07b] P. Borri and W. Langbein. Four-wave mixing dynamics of excitons in InGaAs self-assembled quantum dots. J. Phys.: Condens. Matter **19**, 295201 (2007).

[CHO94] W. W. Chow, S. W. Koch and M. Sargent. *Semiconductor laser physics.* (Springer, Berlin, 1994).

[CHO95] W. W. Chow, R. A. Indik, A. Knorr, S. W. Koch and J. V. Moloney. Time-resolved nondegenerate four-wave mixing in a semiconductor amplifier. Phys. Rev. A **52**, 2479 (1995).

[CHO99] W. W. Chow and S. W. Koch. *Semiconductor-Laser Fundamentals.* (Springer, 1999).

[CHO05] W. W. Chow and S. W. Koch. Theory of semiconductor quantum-dot laser dynamics. IEEE J. Quantum Electron. **41**, 495–505 (2005).

[CON10] G. Contestabile, A. Maruta, S. Sekiguchi, K. Morito, M. Sugawara and K Kitayama. Cross-Gain Modulation in Quantum-Dot SOA at 1550nm. IEEE J. Quantum Electron. **46**, 1696–1703 (2010).

[GOM08] J. Gomis-Bresco, S. Dommers, V. V. Temnov, U. Woggon, M. Lämmlin, D. Bimberg, E. Malić, M. Richter, E. Schöll and A. Knorr. Impact of Coulomb scattering on the ultrafast gain recovery in InGaAs quantum dots. Phys. Rev. Lett. **101**, 256803 (2008).

[GOM09] J. Gomis-Bresco, S. Dommers, V. V. Temnov, U. Woggon, J. Martinez-Pastor, M. Lämmlin and D. Bimberg. InGaAs Quantum Dots Coupled to a Reservoir of Nonequilibrium Free Carriers. IEEE J. Quantum Electron. **45**, 1121–1128 (2009).

[GIO06] Filippo S. Giorgi, Gloria Lazzeri, Gianfranco Natale, Alfonso Iudice, Stefano Ruggieri, Antonio Paparelli, Luigi Murri and Francesco Fornai. MDMA and seizures: a dangerous liaison? Ann. N. Y. Acad. Sci. **1074**, 357–364 (2006).

[GIO08] M. Gioannini, G. A. P. The and I. Montrosset. Multi-population rate equation simulation of quantum dot semiconductor lasers with feedback. In *Numerical Simulation of Optoelectronic Devices, 2008. NUSOD '08. International Conference on*, Seite 101, 2008.

[GOR54] J. P. Gordon, H. J. Zeiger and C. H. Townes. Molecular Microwave Oscillator and New Hyperfine Structure in the Microwave Spectrum of NH_3. Physical Review **95**, 282–284 (1954).

[GRU95] M. Grundmann, N. N. Ledentsov, R. Heitz, L. Eckey, J. Christen, J. Böhrer, D. Bimberg, S. S. Ruvimov, P. Werner, U. Richter, J. Heydenreich, V. M. Ustinov, A. Yu. Egorov, A. E. Zhukov, P. S. Kop'ev and Zh. I. Alferov. InAs/GaAs quantum dots: Radiative recombination from zero-dimensional states. phys. status solidi (b) **188**, 249 (1995).

[HAK83a] H. Haken. *Laser Theory.* (Springer, 1983).

[HAL62] R. N. Hall, G. E. Fenner, J. D. Kingsley, T. J. Soltys and R. O. Carlson. Coherent light emission from GaAs junctions. Physical Review Letters **9**, 366–368 (1962).

[HAU94] H. Haug and S. Koch. *Quantum theory of the optical and electronic properties of semiconductors.* (World Scientific, Singapore, 1994).

[HAU04] H. Haug and S. W. Koch. *Quantum Theory of the Optical and Electronic Properties of Semiconductors.* (World Scientific, Singapore, 2 edition, 2004).

[HEN82] C. H. Henry. Theory of the linewidth of semiconductor lasers. IEEE J. Quantum Electron. **18**, 259–264 (1982).

[HOL62] Jr. N. Holonyak and S. F. Bevacqua. Coherent (visible) light emission from Ga(AsP) junctions. Applied Physics Letters **1**, 82–83 (1962).

[INO92] T. Inoshita and H. Sakaki. Electron relaxation in a quantum dot: Significance of multiphonon processes. Phys. Rev. B **46**, 7260–7263 (1992).

[INO97] T. Inoshita and H. Sakaki. Density of states and phonon-induced relaxation of electrons in semiconductor quantum dots. Phys. Rev. B **56**, R4355–R4358 (1997).

[JAC03] K. Jacobi. Atomic structure of InAs quantum dots on GaAs. Progr. Surf. Sci. **71**, 185–215 (2003).

[KEL11a] B. Kelleher, C. Bonatto, G. Huyet and S. P. Hegarty. Excitability in optically injected semiconductor lasers: Contrasting quantum-well- and quantum-dot-based devices. Phys. Rev. E **83**, 026207 (2011).

[KIM10a] J. E. Kim, E. Malić, M. Richter, A. Wilms and A. Knorr. Maxwell-Bloch Equation Approach for Describing the Microscopic Dynamics of Quantum-Dot Surface-Emitting Structures. IEEE J. Quantum Electron. **46**, 1115–1126 (2010).

[KNO92] A. Knorr, R. Binder, M. Lindberg and S. W. Koch. Theoretical study of resonant ultrashort-pulse propagation in semiconductors. Phys. Rev. A **46**, 7179–7186 (1992).

[KNO93] A. Knorr, R. Binder, E. M. Wright and S. W. Koch. Amplification, absorption, and lossless propagation of femtosecond pulses in semiconductor amplifiers. Opt. Lett. **18**, 1538 (1993).

[LIN10] B. Lingnau, K. Lüdge, E. Schöll and W. W. Chow. Many-body and nonequilibrium effects on relaxation oscillations in a quantum-dot microcavity laser. Appl. Phys. Lett. **97**, 111102 (2010).

[LIN11b] B. Lingnau. *Many-body effects in quantum dot lasers with optical injection.* Master's thesis, TU Berlin, 2011.

[LIN12] B. Lingnau, K. Lüdge, W. W. Chow and E. Schöll. Optimizing modulation properties of quantum-dot semiconductor lasers by electron lifetime engineering. Appl. Phys. Lett. (2012). submitted.

[LIU94] A. Liu. Local-field effect on the linear optical intersubband absorption in multiple quantum wells. Phys. Rev. B **50**, 8569 (1994).

[LOR06b] M. Lorke, W. W. Chow, T. R. Nielsen, J. Seebeck, P. Gartner and F. Jahnke. Anomaly in the excitation dependence of the optical gain of semiconductor quantum dots. Phys. Rev. B **74**, 035334 (2006).

[LOR06] M. Lorke, T. R. Nielsen, J. Seebeck, P. Gartner and F. Jahnke. Influence of carrier-carrier and carrier-phonon correlations on optical absorption and gain in quantum-dot systems. Phys. Rev. B **73**, 085324 (2006).

[LOR07] M. Lorke, F. Jahnke and W. W. Chow. Excitation dependences of gain and carrier-induced refractive index. Appl. Phys. Lett. **90**, 051112 (2007).

[LUE08] K. Lüdge, M. J. P. Bormann, E. Malić, P. Hövel, M. Kuntz, D. Bimberg, A. Knorr and E. Schöll. Turn-on dynamics and modulation response in semiconductor quantum dot lasers. Phys. Rev. B **78**, 035316 (2008).

[LUE09] K. Lüdge and E. Schöll. Quantum-dot lasers – desynchronized nonlinear dynamics of electrons and holes. IEEE J. Quantum Electron. **45**, 1396–1403 (2009).

[LUE10a] K. Lüdge, R. Aust, G. Fiol, M. Stubenrauch, D. Arsenijević, D. Bimberg and E. Schöll. Large Signal Response of Semiconductor Quantum-Dot Lasers. IEEE J. Quantum Electron. **46**, 1755 –1762 (2010).

[LUE10] K. Lüdge and E. Schöll. Nonlinear dynamics of doped semiconductor quantum dot lasers. Eur. Phys. J. D **58**, 167–174 (2010).

[LUE11] K. Lüdge, E. Schöll, E. A. Viktorov and T. Erneux. Analytic approach to modulation properties of quantum dot lasers. J. Appl. Phys. **109**, 103112 (2011).

[LUE11b] K. Lüdge. *Nonlinear Laser Dynamics - From Quantum Dots to Cryptography.* (Wiley-VCH, Weinheim, 2012).

[LAN87] O. Madelung, Hrsg. *Landolt-Börnstein: Numerical Data and Functional Relationships in Science and Technology*, volume III/22a. (Springer, 1987).

[MAJ10] N. Majer, K. Lüdge and E. Schöll. Cascading enables ultrafast gain recovery dynamics of quantum dot semiconductor optical amplifiers. Phys. Rev. B **82**, 235301 (2010).

[MAJ11] N. Majer, S. Dommers-Völkel, J. Gomis-Bresco, U. Woggon, K. Lüdge and E. Schöll. Impact of carrier-carrier scattering and carrier heating on pulse train dynamics of quantum dot semiconductor optical amplifiers. Appl. Phys. Lett. **99**, 131102 (2011).

[MAJ11a] N. Majer, K. Lüdge and E. Schöll. Maxwell-Bloch approach to Four-Wave Mixing in quantum dot semiconductor optical amplifiers. In Joachim Piprek, Hrsg., *11th Internat. Conf. on Numerical Simulation of Optoelectronic Devices (NUSOD), Rome 2011*, IEEE Proc., Seiten 153–154. IEEE, 2011.

[MEU11] C. Meuer, C. Schmidt-Langhorst, R. Bonk, H. Schmeckebier, D. Arsenijević, G. Fiol, A. Galperin, J. Leuthold, C. Schubert and D. Bimberg. 80 Gb/s wavelength conversion using a quantum-dot semiconductor optical amplifier and optical filtering. Opt. Express **19**, 5134–5142 (2011).

[MEY91] P. Meystre and M. Sargent. *Elements of Quantum Optics*. (Springer Verlag, 2nd edition, 1991).

[MIC03] P. Michler. *Single quantum dots: fundamentals, applications, and new concepts*, volume 90. (Springer, 2003).

[NAT62] M. I. Nathan, W. P. Dumke, G. Burns, Jr. F.H. Dill and G. Lasher. Stimulated emission of radiation from GaAs p-n junctions. Applied Physics Letters **1**, 62–64 (1962).

[NIE04] T. R. Nielsen, P. Gartner and F. Jahnke. Many-body theory of carrier capture and relaxation in semiconductor quantum-dot lasers. Phys. Rev. B **69**, 235314 (2004).

[ODR07a] I. O'Driscoll, T. Piwonski, J. Houlihan, G. Huyet, R. J. Manning and B. Corbett. Phase dynamics of InAs/ GaAs quantum dot semiconductor optical amplifiers. Appl. Phys. Lett. **91**, 263506 (2007).

[OSI87] M. Osinski and J. Buus. Linewidth Broadening Factor in Semiconductor Lasers – An Overview. IEEE J. Quantum Electron. **23**, 9–29 (1987).

[OTT10] C. Otto, K. Lüdge and E. Schöll. Modeling quantum dot lasers with optical feedback: sensitivity of bifurcation scenarios. phys. stat. sol. (b) **247**, 829 (2010).

[OTT11] C. Otto, K. Lüdge, E. A. Viktorov and T. Erneux. Quantum dot laser tolerance to optical feedback. In K. Lüdge, Hrsg., *Nonlinear Laser Dynamics - From Quantum Dots to Cryptography*, chapter 6, Seiten 141–162. (WILEY-VCH, Weinheim, 2011).

[OTT12] C. Otto, B. Globisch, K. Lüdge, E. Schöll and T. Erneux. Complex Dynamics of Semiconductor Quantum Dot Lasers Subject to Delayed Optical Feedback. Int. J. Bif. Chaos (2012). accepted.

[PAU12] J. Pausch, C. Otto, E. Tylaite, N. Majer, E. Schöll and K. Lüdge. Optically injected quantum dot lasers - impact of nonlinear carrier lifetimes on frequency locking dynamics. New J. Phys. (2012). accepted.

[PIW07] T. Piwonski, I. O'Driscoll, J. Houlihan, G. Huyet, R. J. Manning and A. V. Uskov. Carrier capture dynamics of InAs/GaAs quantum dots. Appl. Phys. Lett. **90**, 122108 (2007).

[POH05] U. W. Pohl, K. Pötschke, A. Schliwa, F. Guffarth, D. Bimberg, N. D. Zakharov, P. Werner, M. B. Lifshits, V. A. Shchukin and D. E. Jesson. Evolution of a multimodal distribution of self-organized InAs/GaAs quantum dots. Phys. Rev. B **72**, 245332 (2005).

[PRE97] F. Prengel, E. Schöll and T. Kuhn. Quantum Kinetics of Intra- and Intersubband Coulomb Dynamics in Quantum Wires. phys. status solidi (b) **204**, 322 (1997). Proc. HCIS-10.

[PRE99] F. Prengel and E. Schöll. Delayed intersubband relaxation in quantum wires due to quantum kinetic Coulomb scattering. Phys. Rev. B **59**, 5806–5816 (1999).

[QAS04] O. Qasaimeh. Theory of four-wave mixing wavelength conversion in quantum dot semiconductor optical amplifiers. IEEE Photonics Technol. Lett. **16**, 993–995 (2004).

[SCH84a] E. Schöll, D. Bimberg, H. Schumacher and P. T. Landsberg. Kinetics of Picosecond pulse generation in semiconductor lasers with bimolecular recombination at high current injection. IEEE J. Quantum Electron. **20**, 394 (1984).

[SCH87] E. Schöll. *Nonequilibrium Phase Transitions in Semiconductors.* (Springer, Berlin, 1987).

[SCH88j] E. Schöll. Dynamic Theory of Picosecond Optical Pulse Shaping by Gain-Switched Semiconductor Laser Amplifiers. IEEE J. Quantum Electron. **24**, 435–442 (1988).

[SCH98] E. Schöll, Hrsg. *Theory of Transport Properties of Semiconductor Nanostructures*, volume 4 von *Electronic Materials Series.* (Chapman and Hall, London, 1998).

[SCH01d] H. C. Schneider, W. W. Chow and S. W. Koch. Many-body effects in the gain spectra of highly excited quantum dot lasers. Phys. Rev. B **64**, 115315 (2001).

[SCH02j] H. C. Schneider, W. W. Chow and S. W. Koch. Anomalous carrier-induced dispersion in quantum-dot active media. Phys. Rev. B **66**, 041310–041310–4 (2002).

[SCH04e] H. C. Schneider, W. W. Chow and S. W. Koch. Excitation-induced dephasing in semiconductor quantum dots. Phys. Rev. B **70**, 235308 (2004).

[SCH05d] S. Schneider, P. Borri, W. Langbein, U. Woggon, R. L. Sellin, D. Ouyang and D. Bimberg. Excited-state gain dynamics in InGaAs quantum-dot amplifiers. IEEE Photon. Technol. Lett. **17**, 2014–2016 (2005).

[SEG05] R. Seguin, A. Schliwa, S. Rodt, K. Pötschke, U. W. Pohl and D. Bimberg. Size-Dependent Fine-Structure Splitting in Self-Organized InAs/GaAs Quantum Dots. Phys. Rev. Lett. **95**, 257402 (2005).

[SEI96] W. Seifert, N. Carlsson, M. Miller, M. E. Pistol, L. Samuelson and L. R. Wallenberg. In-situ growth of quantum dot structures by the Stranski-Krastanow growth mode. Prog. Crystal Growth and Charact. **33**, 423–472 (1996).

[SUG04] M. Sugawara, H. Ebe, N. Hatori, M. Ishida, Y. Arakawa, T. Akiyama, K. Otsubo and Y. Nakata. Theory of optical signal amplification and processing by quantum-dot semiconductor optical amplifiers. Phys. Rev. B **69**, 235332 (2004).

[SUG05] M. Sugawara, N. Hatori, M. Ishida, H. Ebe, Y. Arakawa, T. Akiyama, K. Otsubo, T. Yamamoto and Y. Nakata. Recent progress in self-assembled quantum-dot optical devices for optical telecommunication: temperature-insensitive 10 Gb s directly modulated lasers and 40 Gb s signal-regenerative amplifiers. J. Phys. D **38**, 2126–2134 (2005).

[USK05] A. V. Uskov, E. P. O'Reilly, M. Lämmlin, N. N. Ledentsov and D. Bimberg. On gain saturation in quantum dot semiconductor optical amplifiers. Opt. Commun. **248**, 211 (2005).

[USK11] A. V. Uskov, C. Meuer, H. Schmeckebier and D. Bimberg. Auger Capture Induced Carrier Heating in Quantum Dot Lasers and Amplifiers. Appl. Phys. Express **4**, 022202 (2011).

[WAC02] A. Wacker. Semiconductor Superlattices: A model system for nonlinear transport. Phys. Rep. **357**, 1 (2002).

[WAL04a] I. Waldmüller, J. Förstner and A. Knorr. Self-consistent projection operator theory of intersubband absorbance in semiconductor quantum wells. In K. Morawetz, Hrsg., *Nonequilibrium physics at short time scales: formation of correlations*, Seite 251. (Springer-Verlag, 2004).

[WAL06] I. Waldmüller, W. W. Chow, E. W. Young and M. C. Wanke. Nonequilibrium many-body theory of intersubband lasers. IEEE J. Quantum Electron. **42**, 292–301 (2006).

[WEG10] M. Wegert, N. Majer, K. Lüdge, S. Dommers-Völkel, J. Gomis-Bresco, A. Knorr, U. Woggon and E. Schöll. Nonlinear Gain Dynamics of Quantum Dot Optical Amplifiers. Semicond. Sci. Technol. **26**, 014008 (2011).

[WET04a] R. Wetzler, A. Wacker and E. Schöll. Coulomb scattering with remote continuum states in quantum dot devices. J. Appl. Phys. **95**, 7966 (2004).

[WET04] R. Wetzler, A. Wacker and E. Schöll. Non-local Auger effect in quantum dot devices. Semicond. Sci. Technol. **19**, S43 (2004).

[WOJ96] A. Wojs, P. Hawrylak, S. Fafard and L. Jacak. Electronic structure and magneto-optics of self-assembled quantum dots. Phys. Rev. B **54**, 5604 (1996).

[XU05a] M. C. Xu, Y. Temko, T. Suzuki and K. Jacobi. Shape transition of InAs quantum dots on GaAs (001). Journal of applied physics **98**, 083525 (2005).

[YEE66] K. Yee. Numerical solution of initial boundary value problems involving Maxwell's equations in isotropic media. IEEE Trans. Antennas Propagat. **14**, 302–307 (1966).